GO-VIKING

Research and Innovation Action (RIA)

This project has received funding from the Euratom research and innovation programme 2021-2025 under Grant Agreement No 101059603

Start date : 2022-06-01 Duration : 48 Months

Code benchmark and lesson learned

Authors : Lilla KOLOSZAR (IVKDF)

GO-VIKING - Contract Number: 101059603

Project officer: Angelgiorgio IORIZZO

Document title	Code benchmark and lesson learned
Author(s)	Lilla KOLOSZAR
Number of pages	77
Document type	Deliverable
Work Package	WP6
Document number	D6.3
Issued by	IVKDF
Date of completion	2026-06-24 16:45:03
Dissemination level	Public

Summary

Description of the benchmark with associated results

Approval

Date	By
2026-06-24 17:25:27	Philippe PLANQUART (IVKDF)
2026-06-24 17:27:28	Papukchiev ANGEL (GRS)

GO-VIKING deliverable D6.3: Results of code benchmark and lessons learned

Month 44

Version 1.0
June / 2026

Authors: Mohammed Muaaz M. D. Hussain (NRG PALLAS), Lilla Koloszar (VKI), Sean Bistany (PSU), Thomas Norddine (EDF), Ewan Harris (EDF-Energy), Yaroslav Dubyk (IPP)

EU DuC = 0E001

Funded by
the European Union

Disclaimer

Funded by
the European Union

Document information

Grant Agreement / Proposal ID	101060826
Project Title	Gathering expertise On Vibration ImpaKt In Nuclear power Generation
Project Acronym	GO-VIKING
Scientific Coordinators	Angel Papukchiev, GRS & Kevin Zwijsen, NRG PALLAS
Project starting date (duration)	1st June 2022 – 31st May 2026 (48 Months)
Related Work Package	WP6
Related Task(s)	Task 6.2 Training
Lead Organisation	NRG PALLAS
Contributing Partner(s)	NRG PALLAS, VKI, EDF, EDF-Energy, PSU, IPP
Due Date	31.03.2026
Submission Date	23.06.2026
Dissemination level	PU
NRG PALLAS Reference	2.6206.20/26.348542/CS/MH/ES

History

Date	Version	Submitted by	Reviewed by	Comments
23.06.2026	1.0	NRG PALLAS	Kevin Zwijsen, Angel Papukchiev	First submitted version

Funded by the European Union

Table of contents

List of figures

Funded by the European Union

List of tables

Abbreviations and acronyms

Acronym	Description
CAD	Computer-Aided Design
CFD	Computational Fluid Dynamics
CFL	Courant–Friedrichs–Lewy number
CSM	Computational Solid Mechanics / Computational Structural Mechanics
D2.1	Deliverable 2.1
D2.2	Deliverable 2.2
D6.3	Deliverable 6.3
DNS	Direct Numerical Simulation
DOF	Degrees of Freedom
EDF	Électricité de France
EDF-Energy	EDF Energy (UK Partner)
FEA	Finite Element Analysis
FEM	Finite Element Method
FFT	Fast Fourier Transform
FSI	Fluid-Structure Interaction
FIV	Fluid-Induced Vibrations
GO-VIKING	Gathering expertise On Vibration Impakt In Nuclear power Generation
GRS	Gesellschaft für Anlagen- und Reaktorsicherheit
ID	Inner Diameter
IPP	Max Planck Institute for Plasma Physics
LES	Large Eddy Simulation
NRG PALLAS	Nuclear Research and Consultancy Group PALLAS
OD	Outer Diameter

PIMPLE	PISO and SIMPLE (Combined OpenFOAM Solver)
PISO	Pressure-Implicit Split-Operator
PSD	Power Spectral Density
RANS	Reynolds-Averaged Navier–Stokes
Re	Reynolds Number
RMS	Root Mean Square
SIMPLE	Semi-Implicit Method for Pressure-Linked Equations
SSG RSM	Speziale, Sarkar, and Gatski Reynolds Stress Model
SST	Shear Stress Transport
T2.1	Task 2.1 (Cantilever Rod Benchmark)
T6.2	Task 6.2 (Training)
TIV	Turbulence-Induced Vibration
TKE	Turbulent Kinetic Energy
URANS	Unsteady Reynolds-Averaged Navier–Stokes
VIV	Vortex-Induced Vibration
VKI	Von Karman Institute
WP2	Work Package 2
WP6	Work Package 6
WR-LES	Wall-Resolved Large Eddy Simulation

Summary

The GO-VIKING deliverable D6.3 is concerned with providing the results of the numerical simulations for the Benchmark 1 of Work Package 2 (WP2) (Cantilever Rod). This involves making predictions of the Flow Induced Vibrations (FIV) of a free-clamped rod exposed to axial water flow. The experimental facility is that of University of Manchester, which has been described in detail along with obtained experimental data in the GO-VIKING deliverable D2.1. The area of interest for the numerical simulations is the test section which comprises of a vibrating rod confined inside a tube.

Six contributing partners: PSU, EDF, VKI, NRG PALLAS, EDF-Energy and IPP, performed numerical simulations on the Cantilever Rod experiment with hemispherical end subjected to an axial flow at Re=21.2k. This document focuses on the benchmark results, but also gives an overview of the modelling efforts at VKI. The details about the modelling approaches of the other benchmark participants can be found in (Hussain, et al., 2025). The selected benchmark case is used to compare the setup, computational costs and results of the involved participants.

Key results from the benchmark indicate that the choice of turbulence model for the fluid has an immense impact on the accuracy and involved computational cost of the simulations. Results also indicate that simplifications can also be made with little-to-no impact on the solution accuracy while reducing computational costs, either by virtue of simplifying the physics (beam model vs full CSM for the rod) or by making simplifications to the geometry and reducing the mesh requirement (single inlet-single outlet configuration, no explicit modelling of lead shots inside the rod).

Keywords

FIV, FSI, CFD, Cantilever Rod, Benchmark, Numerical Simulations

1. Purpose

In the context of nuclear engineering, turbulence induced vibration of fuel rods can lead to mechanical wear, which can be responsible for safety issues and significant maintenance costs in Nuclear Power Plants (NPPs). The "Gathering expertise On Vibration ImpaKt In Nuclear power Generation" (GO-VIKING) European project aims at developing Fluid Structure Interaction (FSI) methods on simpler geometries. Both experimental and reference numerical data are used to develop engineering tools and assess industrial numerical models. In the context of WP6 Task 6.2 , a benchmark has been set up on a cantilever beam configuration, in a confined tube and hydraulic diameter representative of a fuel rod. The main objective is to compare the results of different partners, generated with different numerical approaches, and to derive conclusions on their performance for the selected benchmark case (hemispherical rod end, Re=21.2k). Special attention is paid on the direct comparison between high fidelity and medium resolution approaches, as well on the agreement with the available experimental data. The moderate Reynolds number experimental case was chosen in order to afford the computationally expensive high fidelity simulations.

2. Introduction

In this report, the description of the single-phase Cantilever Rod experiment, the benchmark setup, and the obtained numerical results are provided.

The report is structured as follows: Chapter 3 provides the Cantilever Rod problem description with all available experimental tests. Chapter 4 presents the selected benchmark case along with a comparison of obtained numerical results against the experiment. Chapter 5 presents the numerical efforts performed by the institution VKI. Readers interested in the numerical efforts performed by the institutions PSU, EDF, NRG PALLAS, EDF-Energy, and IPP are referred to chapters 5-9 respectively of (Hussain, et al., 2025). The overall summary and conclusions of this report are provided in Chapter 6.

3. Problem/experiment description

The experiment of interest is the FIV of a cantilevered rod subjected to axial flow. This was performed at the University of Manchester, UK. This chapter provides key details of the experiment and available data. Readers interested in further details of the same are referred to (Cioncolini, et al., 2022).

3.1 Flow Loop and Test Section

The test rig consists of an open loop system where a pump drives water through the test section. Both flow directions are possible and are labelled as 1) Free-Clamped setup where the water flows up the vertical test section moving from the free end of the rod to the clamped end of the rod and 2) Clamped-Free setup where the water flows down the vertical test section moving from the clamped end of the rod to the free end of the rod. These are schematically shown in Figure 1.

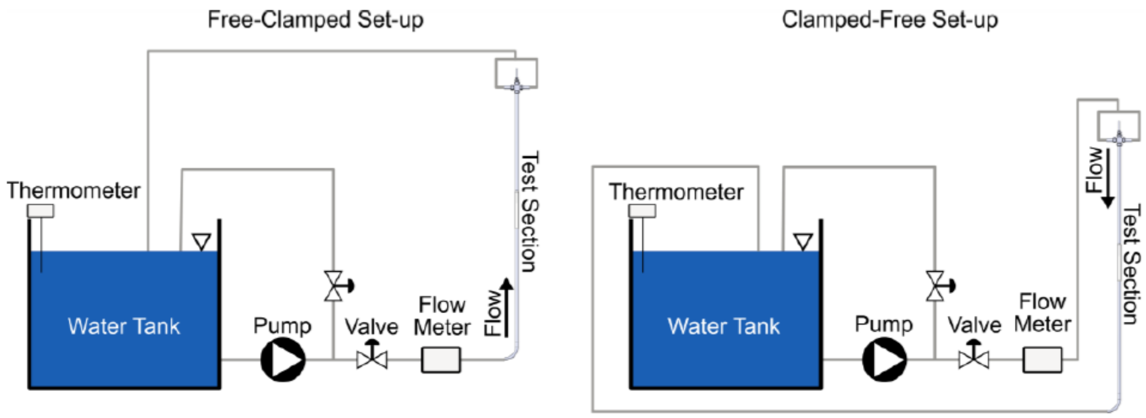

Figure 1. Schematic of the two flow configurations in the test rig (Cioncolini, et al., 2022)

The test section has a vertical vibrating rod that is clamped at the top within a union cross and free at the bottom tip, where vibration takes place, inside a confining vertical tube. A detailed schematic of the same is provided in Figure 2. Both of the aforementioned setup configurations can be implemented on the test section by simply swapping the inlet and outlet connections between the flow loop and the test section. The confining pipe has 20.86±0.05 mm inner diameter (D1) and 25.06±0.01 mm outer diameter. The pipe is made of AISI 316 stainless steel and is rigidly connected to a fixed frame, attached to the rig.

Funded by
the European Union

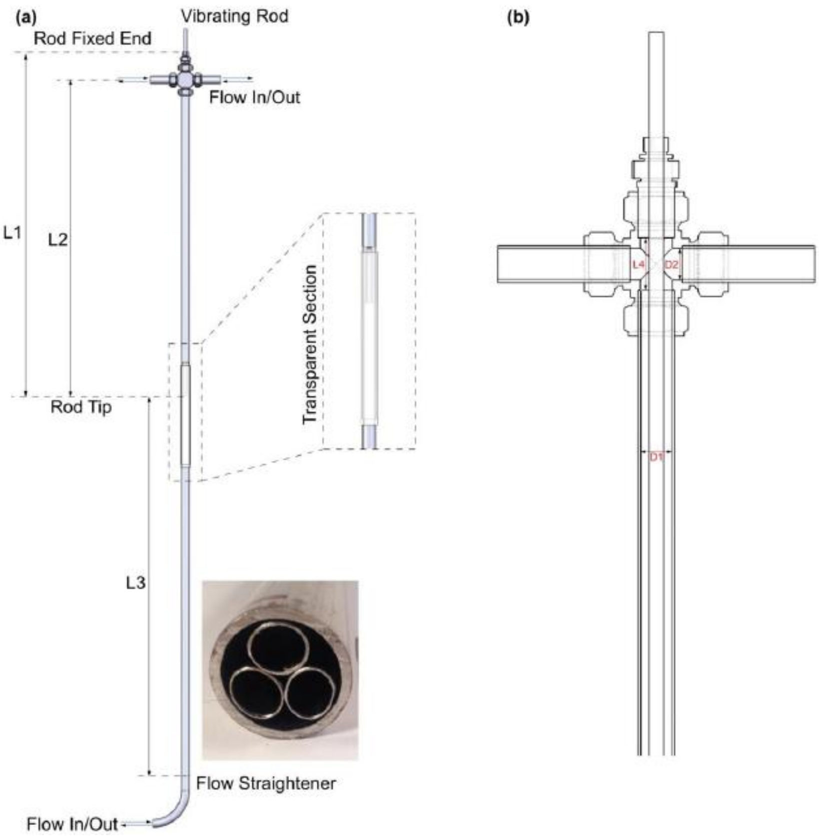

Figure 2. Experimental test section: (a) full test piece with a closeup showing the internal structure of the flow straightener; (b) union cross internal configuration (Cioncolini, et al., 2022)

A matching diameter Perspex transparent section is inserted near the rod tip for optical detection of the rod motion and flow visualization measurement. Because the flow is confined within a cylindrical tube, a surrounding rectangular box with flat faces was needed to reduce optical distortion via index matching. This surrounding structure has a square cross-section and is made of Perspex. The box structure was filled with water during experiments, which proved sufficient to remove the majority of the induced lensing effect of visualizing the flow through the cylindrical pipe. Another viewing window was also present approximately 10D1 upstream the rod tip to capture the flow in order to assist the numerical simulations with providing inflow turbulence.

A flow straightener is located at the bottom of the confining tube which acts to remove swirl and secondary flows with limited pressure drop for the Free-Clamped configuration. At the top, the test piece is connected to two symmetrically routed outlet pipes (same size as the test section confining tube) via a union cross which also holds the vibrating rod in place.

As shown in Figure 2, the free length of the rod from the clamping point to the free end (L1) is 1045 ± 1 mm for the hemispherical end and 1043 ± 1 mm for the blunt end. The distance between the centre of the symmetric pipes and the free end of the rod (L2) is 944±1 mm for the hemispherical end and 942 ± 1 mm for the blunt end. Inside the union cross, the internal cross pipe section has diameter (D2) of 21.8 mm and length (L4) of 35.7 mm. The distance between the top of the flow straightener and the vibrating rod free end (L3) is 1100 mm for the hemispherical end and 1102 mm for the blunt end, corresponding to a flow recovery length of ~53 confining pipe diameters which is proven to be sufficient for the flow to approach fully-developed conditions upstream of the vibrating rod free-end.

3.2 Rod Configurations

The vibrating rod is made of an 8.83±0.05 mm/10.01±0.06 mm inner/outer diameter AISI 316 stainless steel circular tube (surface roughness = 2-3 µm). The hydraulic diameter of the annular gap between the confining tube and the vibrating rod is 10.85 mm (20.86 mm – 10.01 mm). Different rod tip configurations are available including hemi-spherical, blunt and 3 cone tip (h/d = 0.5, 1.0 and 2.0) configurations. The different cone end-pieces were 3D printed using hard resin. For each experimental run, these cone-shaped end-pieces were firmly affixed onto the flat surface of the blunt end-piece using a secure adhesive. Figure 3 shows these configurations and dimensions of the rod end-pieces.

To minimize any potential local mass effects of the end-piece on the rod dynamics, the end-pieces were made of lightweight aluminum (density = 2.74 g.cm^{-3}) and have a mass of approximately 2.8 g (surface roughness = 0.4-0.5 µm) for the curved end and approximately 2.1 g for the blunt end so that it does not appreciably alter the linear mass density of the vibrating rod. The vibrating rod was filled with lead shots (density: 11.34 g.cm−3; diameters: 0.3-1.6 mm; source: manufacturer data) to mimic the loading of fuel pellets in nuclear fuel bundles. The measured mass density of the rod, accounting for rod material and lead shot filling, was 588 g.m^{-1}.

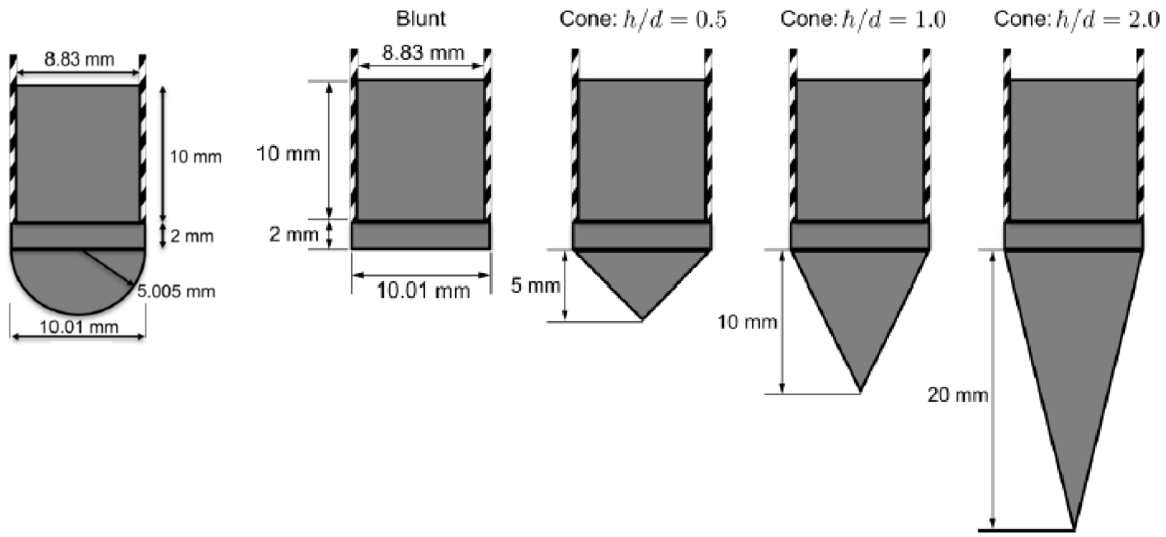

Figure 3. Schematic and dimension of end-pieces for cantilever rod (Hatching represents the rod pipe) (Cioncolini, et al., 2022)

3.3 Available Measurement Data

Broadly, there are two sets of measurement done: 1) Tracking the flow-induced motion of the free-end of the vibrating rod and 2) Flow field measurement upstream, around and downstream of the rod tip.The rod tip motion was captured using a fast-imaging camera (Panasonic Lumix DMC-FZ200; image resolution: 1280 x 720 pixels; recording frequency: 100 fps; recording duration: 60 s) positioned facing the test piece. The tip motion of the vibrating rod has been recorded from two sides, as a mirror placed at 45 degrees has been used so that both the front and side motions are captured as shown in Figure 4.

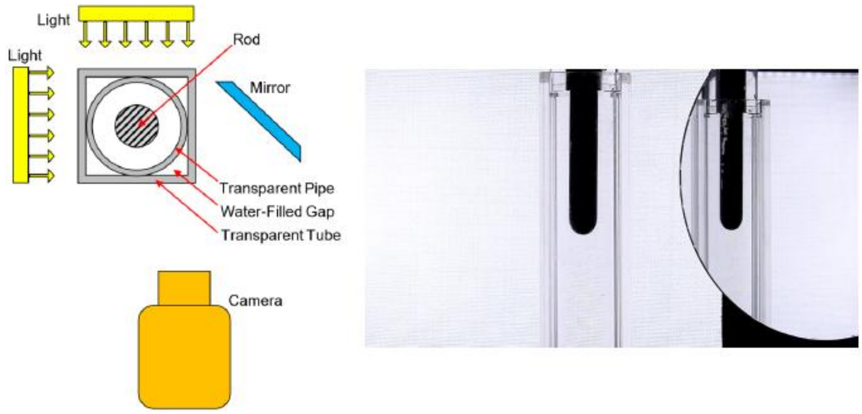

Figure 4. Motion tracking set-up arrangement (Cioncolini, et al., 2022)

The experimental setup was validated with preliminary free vibration experiments in still water which gave the free vibration frequency of the rod in still water (3.72 Hz) and the damping ratio of the rod in still water (0.015 ± 0.001). Similar tests in air gave corresponding values of 4.10 Hz and 0.0009.

The experiments are performed in a large range of Reynolds numbers from 10^4 up to 10^5 for all configurations. Key vibration results are extracted from the rod tip displacement (both in-plane directions) time history. These are the RMS rod vibration amplitude and the vibrational frequency. Select results are shown in Figure 5 for all but the curved end rod configuration.

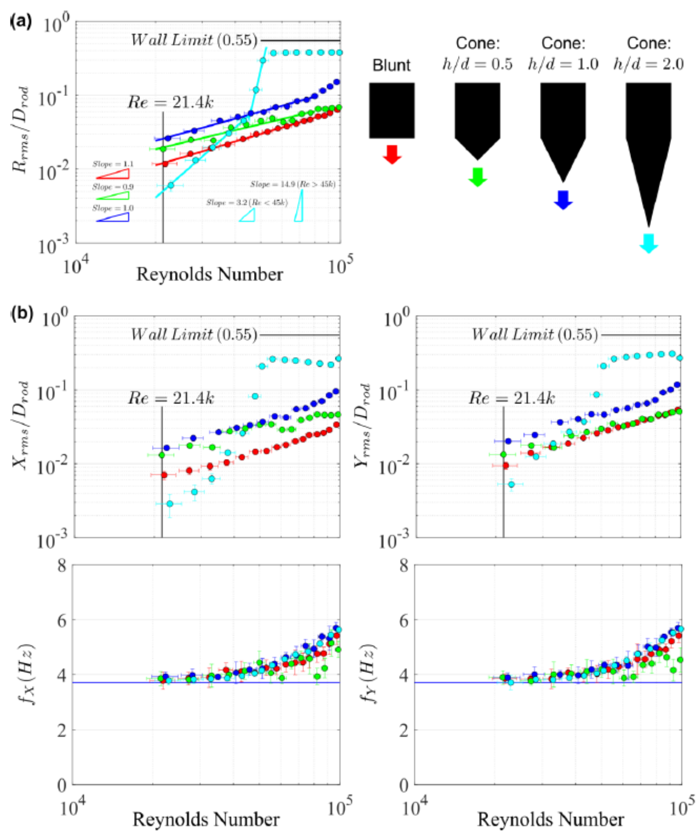

Figure 5. RMS displacement and frequency for rod with different tip shapes against Reynolds number for the clamped-free configuration. (a) Resultant radial displacement. (b) Displacements from the front, X, and side, Y directions. The displacement is scaled using the rod outer diameter (D_{rod} = 10.01 mm). (Cioncolini, et al., 2022)

At selected flow rates, PIV measurements were carried out to visualize the complex flow field around the vibrating rod tip. A Dantec Dynamics PIV system was used in these measurements, consisting of a double cavity Nd:YLF laser, that provides maximum output energy of 15 mJ at a wavelength of 527nm. Care was taken to avoid the shadow of the rod obscuring part of the flow visualization region. The PIV setup is shown in Figure 6. To provide upstream conditions for up flows, another viewing window has been selected at approximately 10D (D: Diameter of the pipe) below the tip of the rod so as to ascertain the attainment of fully-developed pipe flow conditions upstream of the rod. Key results also include measurement of horizontal and vertical profiles of the axial and horizontal components of velocity. Contour plots are available for these velocity components, Reynolds Stress Tensor components and vorticity. Select contour plots are presented in Figure 7 for the curved end for the free-clamped configuration.

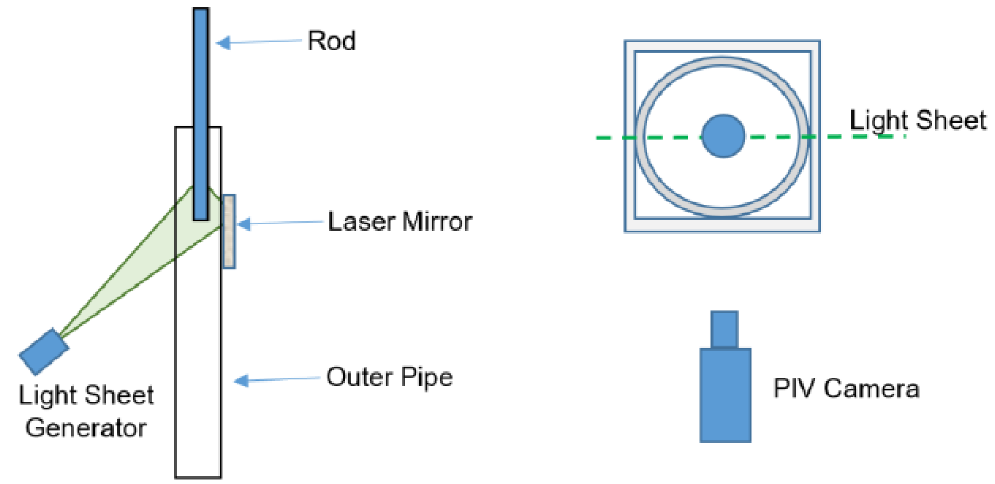

Figure 6. PIV set-up arrangement (Cioncolini, et al., 2022)

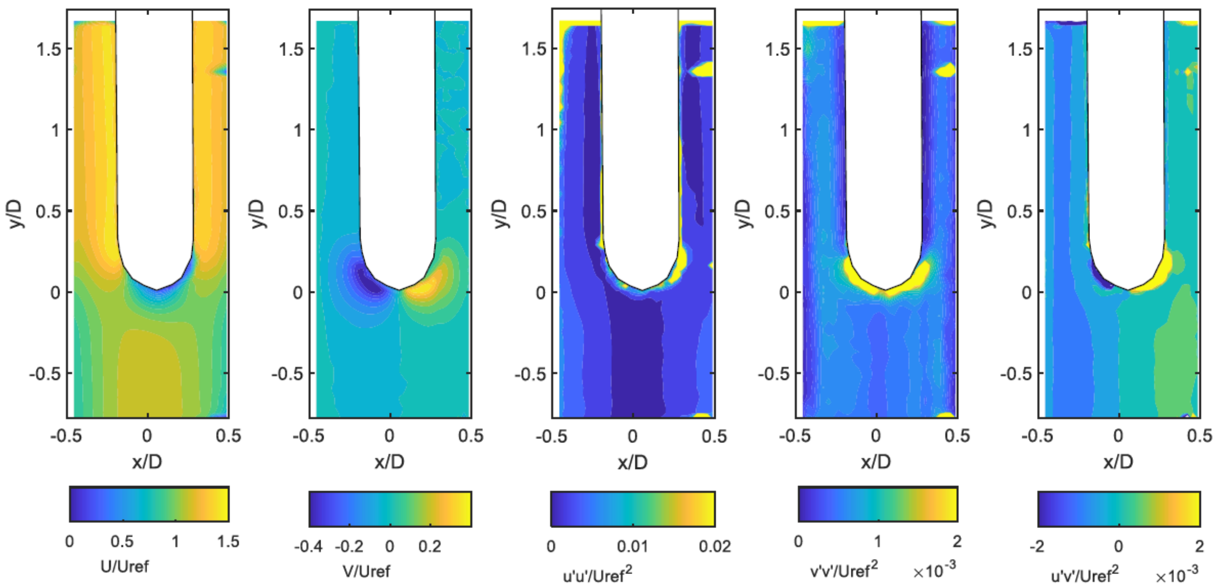

Figure 7. Time-averaged contours of the normalised axial mean velocity, U, radial mean velocity, V, normal turbulent stresses in the axial and radial directions, u'u' and v'v' respectively and turbulent shear stresses, u'v', (Uref is the mean velocity), for up flow at a Reynolds number of 40k. (Cioncolini, et al., 2022)

4. Benchmark

4.1 Introduction

The free-clamped flow at Re=21.2k for the rod with a hemispherical tip was the chosen configuration for the benchmark. The curved rod tip provides a numerically challenging case since the generation of vortices and flow separation would be inhibited. Thus, the vibrations are expected to be predominantly turbulence-induced, which is typical for axial FIV. The lower Re is chosen so that high fidelity methods such as LES would still be computationally feasible in an FSI context.

A total of 6 institutions have participated in this benchmark: PSU, EDF, VKI, NRG PALLAS, EDF-Energy, and IPP. Key details of the numerical simulations of the participants are provided in Section 4.2. The key results compared to the experiment are segregated based on flow fields and based on FIV rod response as presented in Section 4.3. The benchmark findings are concluded with a summary provided in Section 4.4.

4.2 Numerical simulations

Table 1 summarizes the participants' individual submissions. PSU performed pure Computational Fluid Dynamics (CFD) simulations while all others performed two-way FSI calculations. PSU, EDF, and VKI performed high fidelity simulations while NRG PALLAS, EDF-Energy and IPP performed medium resolution URANS simulations. Although the focus of this chapter will be on the benchmark case of Re=21.2k up-flow for the hemispherical rod tip, additional simulations were performed by the institutions and have been summarized in Table 2. Details on the results achieved by VKI can be found in chapter 5, while those for the other participants can be found in chapters 5 through 9 of (Hussain, et al., 2025).

Table 1. Key Information of the Submissions

Institution	Approach	Turbulence Modelling	Solid Modelling	Software(s)
PSU	CFD	DNS	NA	NekRS V23
EDF	Two-way FSI	WR-LES - Smagorinsky	Euler-Bernoulli Beam Model	Code_Saturne V8 + Beam Model implementation
VKI	Two-way FSI	WR-LES – one-equation Yoshizawa	Rigid body motion	OpenFOAM V2206 + preCICE V3.3
NRG PALLAS	Two-way FSI	URANS - Standard K-Epsilon Low Re (cubic)	Finite Element CSM	Simcenter STAR-CCM+ V2306
EDF-Energy	Two-way FSI	URANS - SSG RSM	Finite Element CSM	Simcenter STAR-CCM+ V2206
IPP	Two-way FSI	URANS - K-Omega SST	Euler-Bernoulli Beam Model	ANSYS CFX + User Library (FORTRAN) implementation of Beam Model

Funded by
the European Union

Table 2. Tested Cases

Institution	Cases Performed
PSU	Hemispherical End: Re=11.077k, 21.2k Blunt End: Re=12.19k
EDF	Hemispherical End: Re=21.2k
NRG PALLAS	Hemispherical End: Re=21.2k, 40k Hemispherical End with Offset: Re=21.2k Blunt End: Re=23.33k
VKI	Hemispherical End: Re=21.2k
EDF-Energy	Hemispherical End: Re=21k Blunt End: 16k, 46k
IPP	Hemispherical End: Re=21.2k

4.2.1 Geometry & Mesh

4.2.1.1 Solid Domain

The rod in the experiment was a composite one with a stainless steel hollow cylinder, an aluminum end plug and was filled with lead shots. The chosen geometries for the solid domain by the participants performing FSI simulations are summarized in Table 3.

NRG PALLAS has excluded only the lead shots, while all other participants performing FSI calculations have adopted a homogenous solid cylinder, which is represented by a rigid body by VKI, a beam model by EDF and IPP, while an FEM CSM is performed by EDF-Energy. VKI, NRG PALLAS, and IPP use a rod diameter of 10.01 mm (matching the experiment) while EDF and EDF-Energy use a rod diameter of 10 mm. PSU uses a rod diameter of 476.19 mm owing to the scaling of other parameters including inflow velocity, density and confining pipe diameter to unity. This is reflected in the fluid domain as PSU does not perform FSI calculations.

Table 3. Solid Domain Details

Institution	Geometry Model	Mesh Type	Mesh Count
EDF	Homogenous Rod with one Material	1D Elements	3.8k Elements
VKI	Homogenous Rod with one Material	Not Meshed, Rigid-Body Motion	NA
NRG PALLAS	Composite Rod with modified SS Hollow Cylinder + Aluminum Plug	Structured Hexahedral for the Hollow Cylinders, Tetrahedral for the Aluminum Plug	178.4k Cells
EDF-Energy	Homogenous Rod with one Material	Structured Hexahedral for the Cylinders, Tetrahedral for the Hemispherical End	62.5k Cells
IPP	Homogenous Rod with one Material	1D Elements	0.1k Points

4.2.1.2 Fluid Domain

In the experiment, the entire test loop can be considered the fluid domain inclusive of the tank and pumps. However, owing to computational constraints, this cannot be adopted. The chosen geometries for the fluid domain by the participants are summarized in Table 4.

NRG PALLAS and IPP have considered the full confining pipe length and the union cross with two outlets while the other participants have assumed a single outlet configuration considering only a portion of the confining pipe length upstream of the rod tip. VKI, NRG PALLAS and IPP use a confining pipe diameter of 20.86 mm (matching experiment) while EDF and EDF-Energy use a confining pipe diameter of 21 mm. PSU uses a scaled confining pipe diameter of 1 m.

Table 4. Fluid Domain Details

Institution	Geometry Model	Mesh Cell Type	Mesh Cell Count (M Cells)	Wall Y+	Courant Number
PSU	With respect to the experiment, 346 mm of Confining Pipe in Test Section considered of which 220 mm of the Rod Length is present. The scaled dimensions are correspondingly 16.476 m and 10.476 m respectively. 1 Inlet – 1 Outlet Configuration.	Structured Hexahedral	2.65 (Polynomial Order=7)	<1	Max. = 2.23
EDF	Entire Rod length + 6D_{pipe} considered. 1 Inlet – 1 Outlet Configuration.	Structured Hexahedral	144	Max. = 1.4 Surf. Avg. = 0.577	Max. = 1 Vol. Avg. = 0.126
VKI	Entire Rod length + 5D_{pipe} considered. 1 Inlet – 1 Outlet Configuration.	Structured Hexahedral	24.3	Max.= 1.9 Surf. Avg. = 0.71	Max. = 0.3
NRG PALLAS	Entire Rod Length + full Vertical Confining Pipe in Test Section + Union Cross considered. 1 Inlet-2 Outlet Configuration	Hexahedral	8.49	Max. = 0.5132 Surf. Avg. = 0.1196	Max. = 29.4672 Vol. Avg. = 0.2278
EDF-Energy	Rod length from Union Cross + 5D_{pipe} considered. 1 Inlet – 1 Outlet Configuration.	Hexahedral	0.2	Max. = 39.4 Surf. Avg. = 31.6	Max. = 0.5 Vol. Avg. = 0.1
IPP	Entire Rod Length + full Vertical Confining Pipe in Test Section + Union Cross considered. 1 Inlet-2 Outlet Configuration	Structured Hexahedral	2.03	Max. = 324.47 Surf. Avg. = 0.353	Max. = 999.9 Vol. Avg. = 33.2

Funded by the European Union

4.2.2 Material Properties

4.2.2.1 Solid Properties

The adopted solid properties are listed in Table 5 for all participants excluding PSU (since there are no solids). Single values are presented for all participants except NRG PALLAS who has used a composite solid. Roughness is only included by NRG PALLAS. Inherent structural damping is included by EDF, VKI, and NRG PALLAS.

Regarding the solid properties, they are chosen in a way that respects the total mass of the rod obtained from the linear mass density of 588 g/m quoted in the experiment. VKI uses a rigid body motion solver and thus directly sets the mass of the rod instead of density. Thereafter, those who use a 1D model (EDF, IPP) or those who have explicitly used a hollow cylinder (NRG PALLAS) end up with a much higher density than those who have a solid cylinder (EDF-Energy). Correspondingly, the Young's Modulus is selected either from standard properties (EDF, VKI, NRG PALLAS, IPP) or are modified to respect the flexural rigidity of the rod based on structural tests in vacuum and water (EDF-Energy).

Table 5. Solid Properties

Institution	Density (kg/m^3)	Young's Modulus (GPa)	Poissons Ratio (-)	Other Provided Data
EDF	33676.3131	193	NA	Quadratic moment of Area = 1.94E-10 m^4 Mechanical Damping Coefficient = 0.08 kg/(ms)
VKI	NA, Mass of the Rod = 0.61446kg	193	NA	Damping Coefficient: Rod = 0.228, Joint = 0.234 Moment of Inertia = (0.0559 0.0559 7.69E-6) kgm^2
NRG PALLAS	33676.313 (SS) 2740 (Aluminum)	193 (SS) 69 (Aluminum)	0.26 (SS) 0.33 (Aluminum)	Rayleigh Damping Model Constant = 7.701 s
EDF-Energy	7490	76.4	0.25	
IPP	33676.31312	193	0.3	Quadratic moment of Area = 1.9443E-10 m^4

4.2.2.2 Fluid Properties

The adopted fluid properties are listed in Table 6 for all participants. With the exception of PSU who has modified fluid properties, all participants adopt water properties at similar temperatures. VKI assumes a clean rounded value for calculations. Concerning the derivation of dynamic viscosity by PSU, the reader is referred to section 5.2.1.2 of (Hussain, et al., 2025).

Funded by the European Union

Table 6. Fluid Properties

<table>
<tr><th>Institution</th><th>Density (kg/m³)</th><th>Dynamic Viscosity (mPa.s)</th><th>Remarks</th></tr>
<tr><td>PSU</td><td>1</td><td>0.03195374325</td><td>Properties modified to achieve low compute cost while realizing same Re</td></tr>
<tr><td>VKI</td><td>1000</td><td>1.000</td><td>Clean rounded numbers assumed</td></tr>
<tr><td>EDF</td><td>997.567</td><td>1.047133</td><td rowspan="4">Slight difference arises from the choice of temperature of water or reference table from which material properties are extracted</td></tr>
<tr><td>NRG PALLAS</td><td>998.23</td><td>1.002</td></tr>
<tr><td>EDF-Energy</td><td>997.57</td><td>1.047</td></tr>
<tr><td>IPP</td><td>998.573</td><td>1.04737</td></tr>
</table>

4.2.3 Boundary Conditions

4.2.3.1 Solid Domain

The adopted solid boundary conditions are provided in Table 7 for all participants who perform FSI calculations.

Table 7. Solid Boundary Conditions

<table>
<tr><th>Institution</th><th>Top Surface/Node</th><th>Other Surfaces/Nodes</th><th>Remarks</th></tr>
<tr><td>EDF</td><td>Wall + Constrained</td><td rowspan="5">FSI Interface</td><td></td></tr>
<tr><td>VKI</td><td>Wall + Constrained</td><td>The cantilever rod is translated to a rigid body constrained by a joint on the top</td></tr>
<tr><td>NRG PALLAS</td><td>Wall + Constrained</td><td>Surface roughness applied to wetted surfaces = 2.5 μm (SS), 0.45 μm (Aluminum)</td></tr>
<tr><td>EDF-Energy</td><td>Symmetry + Constrained</td><td>Symmetry is applied because the full length of the rod is not present. Only the length from the union cross height to the tip is considered.</td></tr>
<tr><td>IPP</td><td>Wall + Constrained</td><td></td></tr>
</table>

4.2.3.2 Fluid Domain

The adopted fluid boundary conditions are listed in Table 8 for all participants. PSU uses modified inflow velocity of 1 m/s. The mass flow rate value used by IPP can be translated to an inflow velocity of 1.509 m/s, similar to the chosen value by NRG PALLAS and VKI. EDF and EDF-Energy have similar inflow velocities. The slight difference between the groups can be attributed to the slight difference in rod and confining pipe diameters while those within the groups can be attributed to the slight difference in chosen fluid material properties.

Table 8. Fluid Boundary Conditions

Institution	Inlet BC	Outlet(s) BC	Remarks
PSU	3D velocity profile with average 1 m/s	0Pa Gauge Pressure Outlet	Inflow velocity profile obtained by precursor simulation of flow through a pipe of length $4D_{pipe}$ with repeating/cyclic boundary conditions. Viscosity is modified to obtain required Re.
EDF	3D velocity profile with average 1.57 m/s		Inflow velocity profile obtained by precursor simulation of flow through a pipe of length $6D_{pipe}$ with repeating boundary conditions
VKI	3D velocity profile with average 1.503 m/s		Inflow velocity profile obtained by precursor simulation of flow through a pipe of length $5D_{pipe}$ with repeating boundary conditions
NRG PALLAS	Single value of 1.51 m/s applied to whole patch		Given that the whole confining pipe length is present, inflow is expected to develop well enough before rod tip.
EDF-Energy	Single value of 1.59 m/s applied to whole patch		Given that confining pipe length of $4.76D_{pipe}$ is present upstream of rod tip, inflow is expected to develop well enough before rod tip.
IPP	Mass Flow Rate of 0.5149 kg/s applied to Inlet patch		Given that the whole confining pipe length is present, inflow is expected to develop well enough before rod tip.

4.2.4 Numerical Settings

Each participant has made a choice for the numerical settings. This information is presented in Table 9.

Table 9. Numerical Settings

Institution	Time Step Size (ms)	Total Simulation Time (s)	Order of Discretization	Other Provided Data
PSU	0.0013422	8.59014	Temporal = 2nd (BDF2/EXT2) Spatial = 8th (N=7)	Average number of inner velocity iterations per time step = 1.4 Average number of inner pressure iterations per time step = 2 Number of subcycling steps per time step = 2
EDF	0.015	82	Temporal = 2nd Spatial = 2nd	Fractional step method similar to SIMPLEC Tolerance for velocity and pressure resolution = 1.0×10^{-5}

Funded by the European Union

EUDuC = 0E001

				Average number of inner iterations = 3.0 for velocity and 14.7 for pressure Max number of RHS reconstruction sweeps = 5 for pressure and 10 for velocity
VKI	0.02	6.72933	Temporal = 2nd Spatial = 2nd	PIMPLE pressure-velocity coupling Tolerance for velocity and pressure resolution = 1.0×10^{-6}
NRG PALLAS	0.1	19.643	Temporal = 2nd (BDF2) Spatial = 2nd	Number of inner iterations per time step = 25 SIMPLEC pressure-velocity coupling scheme
EDF-Energy	0.15	11.0001	Temporal = 2nd (BDF2) Spatial = MUSCL 3rd (momentum transport), 2nd (RST transport)	Number of inner iterations per time step = 25 SIMPLE pressure-velocity coupling scheme
IPP	20	40	Temporal = 2nd (Backward Euler) Spatial = 2nd (High Resolution)	Number of inner iterations per time step = 10 Coupled pressure-velocity coupling scheme

4.2.5 Computational Resources

The computational resources consumed by each participant in the endeavor of the benchmark are presented in Table 10.

Table 10. Computational Resources

Institution	Wall Clock Time	Equivalent CPU/Node hours	RAM	No. of (CPU/GPU) Cores	Other Provided Data
PSU	≈15d	≈25E3 node h	70 TB	560 GPUs	Averaging runs storage space = 234 TB Q-criterion video storage space = 124 TB Number of nodes used = 70 Each node has one 64-core AMD EPYC CPU and four AMD MI250X GPUs, which are treated as eight GPUs (or GCDs) by the system Approximate costs per time step:

					RHS assembly (makef) = 34% Velocity Solve = 9% Pressure Solve 40% Execute step (averaging)/TKE budg-ets = 5-10%
EDF	92d	6.96E6 CPU h	16.875 TB	3150 CPU cores	Number of nodes used = 90
VKI	NA	NA	NA	NA	Number of nodes used = 10
NRG PALLAS	145d 9h 20m	3.49E5 CPU h	256 GB	100 CPU cores	Number of nodes used = 1
EDF-En-ergy	14d	4E4 CPU h	480 GB	120 CPU cores	Number of nodes used = 3
IPP	25h 9m	5.037E2 CPU h	11.08 GB	20 CPU cores	Number of nodes used = 1

4.2.6 Simulation Strategy

Each participant has taken a unique approach to perform the simulation of the benchmark case. This is presented for each institution:

4.2.6.1 PSU

The following strategy is adopted:

- The inlet recycling length is equivalent to four pipe diameters and serves as the precursor domain. At first, the simulation is run with a lower Re, and the turbulence is fully developed.
- The simulations with the cantilevered rod is initialized with this fully developed turbulent pipe flow mapped to the pipe inlet.
- The Reynolds number is gradually increased for stability of the solver.

Once the target Re is achieved, to flush out any flow development effects, the simulation was run for five to ten flow passes before averaging, collecting turbulence statistics, and collecting time history data. The latter activities are carried out for the aforementioned ~8.59s (or approx. 20 flow throughs).

4.2.6.2 EDF

The following strategy is adopted:

- First, only the precursor domain is simulated to generate inflow boundary conditions. This is done for 10 s simulation time.
- Then, this is supplied to the inflow of the actual domain with the rod remaining fixed and is thus a pure CFD calculation to flood the domain with turbulent inflow and develop forces on the rod. This is done for a simulation of 12 s, i.e from 10 s to 22 s.
- Finally, the rod is released and the oscillations are captured. This goes on for another 60s, i.e from 22 s to 82 s, which marks the rest of the simulation.

To compare the results, the last 50 s is used to carry out the statistical analysis that is used to compare against the experimental data.

4.2.6.3 VKI

The following strategy is adopted:

- First, only the precursor simulation is performed. Once statistical steady state is reached the averaging was done for 5s.
- Then, the precursor simulation was connected to the main domain with the help of the preCICE coupling software to provide inflow data coherent in space and time.
- A stationary rod simulation was first performed for 6s, before adding rigid body movement. Once the rod was released, this movement was simulated for an additional 0.72933s. The total simulation time is thus 6.72933s for the main domain.

To compare the results, the last 0.72933 s is used to carry out the statistical analysis that is used to compare against the experimental data.

4.2.6.4 NRG PALLAS

The following strategy is adopted:

- First, a pure CFD RANS calculation is done starting the flow from rest and applying inflow boundary conditions. This is done for 2000 iterations which was observed to be enough to generate the flow field around the rod.
- Then, the solver is switched to URANS and the FSI simulation is carried out for a duration of 19.643 s or 14.28 flow passes (FP) where 1 FP = 1.375551606 s.

To perform the statistics in order to compare results, the first 3.5FP is ignored for the vibration while the first 4.5FP is ignored for the velocity fields.

4.2.6.5 EDF-Energy

The following strategy is adopted:

- First, a pure CFD URANS calculation is performed, with the solid rod domain fixed completely and uncoupled from the fluid domain for 1.0 seconds.
- Then, the FSI coupling is enabled at 1.0 s until the end of the simulation at 11 s. The FSI traction is ramped linearly from 1.00 s to 1.01 s.

To perform the statistics in order to compare results, the first 2.02 seconds of the time series are removed. The remaining was then used to perform the PSD calculation and calculate the characteristic frequencies of the system.

4.2.6.6 IPP

The following strategy is adopted:

- First, a pure CFD URANS calculation is done starting the flow from rest and applying inflow boundary conditions with the rod fixed. This is done for 10 s.
- Then, the rod is allowed to move and the FSI simulation is carried out for a duration of 30 s, i.e from 10 s to 40 s.

To perform the statistics in order to compare results, the entire 30 s of the FSI part of the calculation is used.

4.3 Obtained Results

The data obtained from the participants are consolidated into appropriate plots and are presented in this section. Comparison to the PIV experimental data are made in section 4.3.1 while those for the vibration data are provided in section 4.3.2.

4.3.1 Flow Field Data Comparison

Before presenting the results, a first look is taken at the verification taken by participants of the inflow profile at a significant distance upstream of the rod. There is experimental data available at 10D upstream of the rod tip which can be used for comparison. However, only NRG PALLAS and IPP have a simulation domain that extends to and beyond this location. EDF-Energy has provided data at 4.76D upstream of the rod tip while EDF and VKI have provided data at a location inside the precursor domain which implies perfectly developed pipe flow without any influence of the downstream rod. PSU did not submit any upstream data.

The available data is plotted and displayed in Figure 8, Figure 9 and Figure 10 for the non-dimensional axial velocity, non-dimensional radial velocity and non-dimensional Reynolds stress component u'v' respectively. Focusing on Figure 8, what is seen from the experimental results is that the non-dimensional velocity profile is independent of the inflow velocity. It is thus possible to use it to compare against numerical results at Re=21.2k. The high fidelity results and medium resolution results agree well within their groups. The maximum disagreement between high and medium resolution solutions is at the centre of the confining pipe where the maximum non-dimensional velocity is captured. The maximum variation of ~9% is observed between the solution of VKI and NRG PALLAS for the maximum velocity. Despite these differences in the solution amongst the participants, all of them can still be considered to be a good match against the experiment.

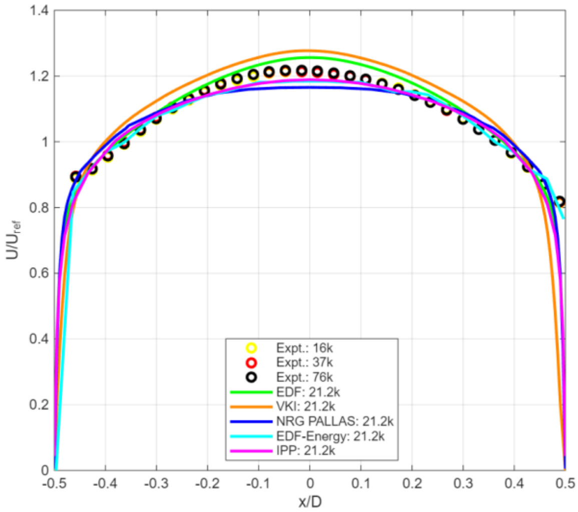

Figure 8. Time-Averaged Non-dimensional Axial Velocity 10D (Expt., EDF, VKI, NRG PALLAS, IPP) and 4.76D (EDF-Energy) ahead of Rod Tip

From Figure 9, it is observed that the experimental results appear to show some dependency on the inflow Re. However, considering the scale of the results and the uncertainty in the U_{ref}, the experimental results can still be considered to suggest Reynolds number independence and can be used for the comparison to numerical results. The trend of the experiment reveals the fluid to move to the left (negative values) in the left half while move to the right (positive values) in the right half, with some scattered data close to the confining pipe walls.

The numerical results all underpredict the radial component of velocity compared to the experiment. Observing the zoomed plot, the numerical results predict a similar order of magnitude. In particular, the solutions by NRG PALLAS and IPP show a very smooth and almost symmetric curve matching the trend expected from the experiment (excluding scattered data). The solution by EDF predicts mostly a positive radial velocity except for a distance of 0.1D at the left pipe wall. This can be explained from the fact that the EDF solution is taken from the precursor domain where the situation is turbulent pipe flow with no influence of the cantilever rod. The solution by VKI also shows no clear preference for direction of radial flow. As with EDF, the VKI solution is also taken from the precursor domain. A consideration here is also the low data acquisition time used for the time-averaging which may also have had an impact. Finally, the solution of EDF-Energy predicts a higher magnitude of radial velocity, but this is explained from the fact that the data is collected 4.76D ahead of the rod tip instead of 10D.

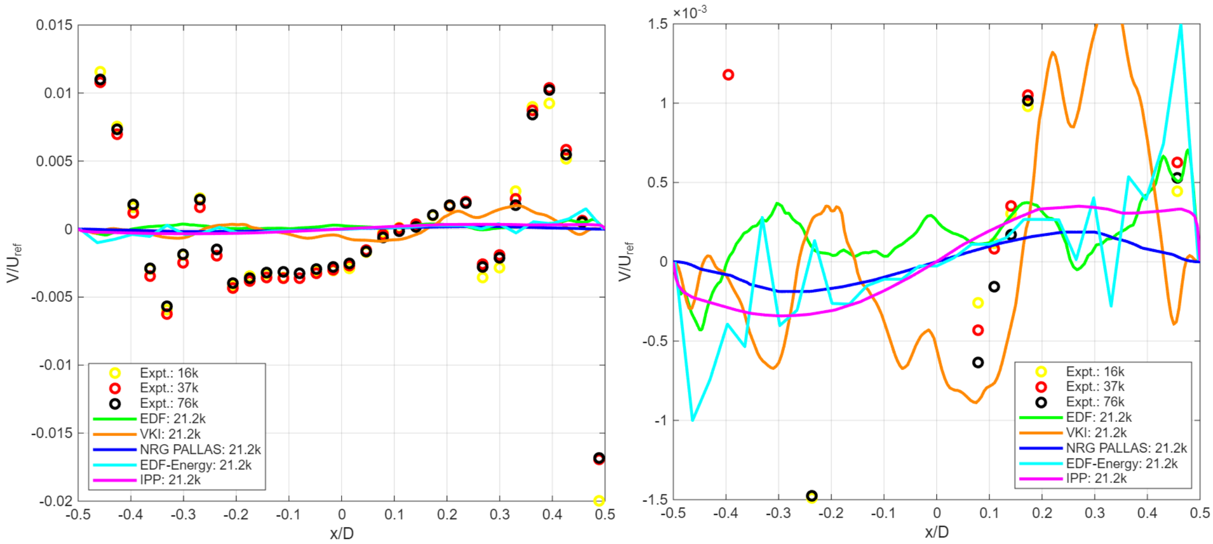

Figure 9. Time-Averaged Non-dimensional Radial Velocity 10D (Expt., EDF, VKI, NRG PALLAS, IPP) and 4.76D (EDF-Energy) ahead of Rod Tip

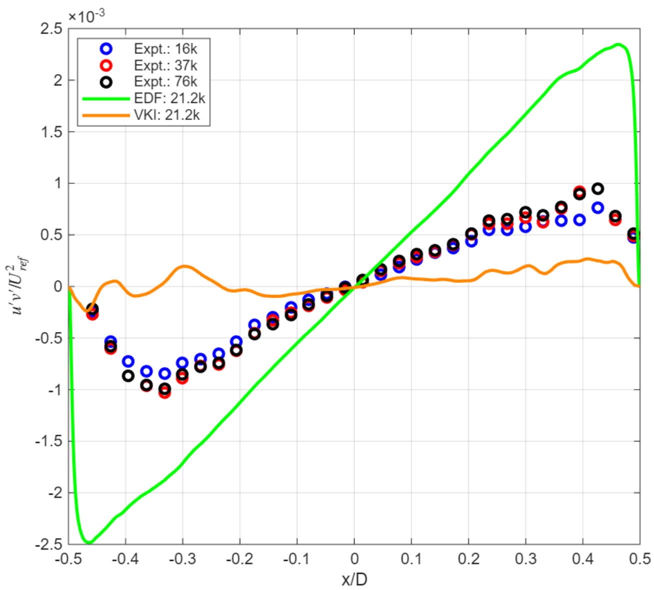

Figure 10. Time-Averaged Non-dimensional Reynolds Stress Component (u'v') 10D ahead of Rod Tip

Figure 10 shows the second order statistics. For reasons similar to that presented for the non-dimensional radial velocity, the experimental solution can be considered to be effectively Re independent. The numerical solution of EDF predicts a trend similar to the experiment but overpredicts the magnitude compared to the experiment. This may be hypothesized to come from the PIV method involving spatial filtering that is done on the interrogation areas which effectively averages out the small, high-frequency turbulent structures, and potentially also due to noise/bias, which could arise from velocity bias (peak locking) and poor time resolution (aliasing) (Lavoie, et al., 2007) (Sarno, et al., 2019). The numerical solution of VKI conforms neither to the experimental trend nor the trend of EDF. This may be due to insufficient time-averaging or incorrect data extraction.

The time-averaged non-dimensional velocity contour plots are shown in Figure 11 and Figure 12. From these results, the flow in the vicinity of the rod tip is revealed. For this upward flow case, the flow upstream of the rod starts to change from a typical fully developed pipe flow owing to the obstruction in flow path caused by the vibrating rod. The flow smoothly curves around the tip of the rod and proceeds upwards through the annular gap between the rod and the confining pipe. Due to a decrease in available cross-section, the flow is seen to speed up in this region. A stagnation point at the rod tip is also observed. The numerical results are found to be in good agreement with the experimental results. The PSU, and especially, VKI, results reveal insufficient time-averaging.

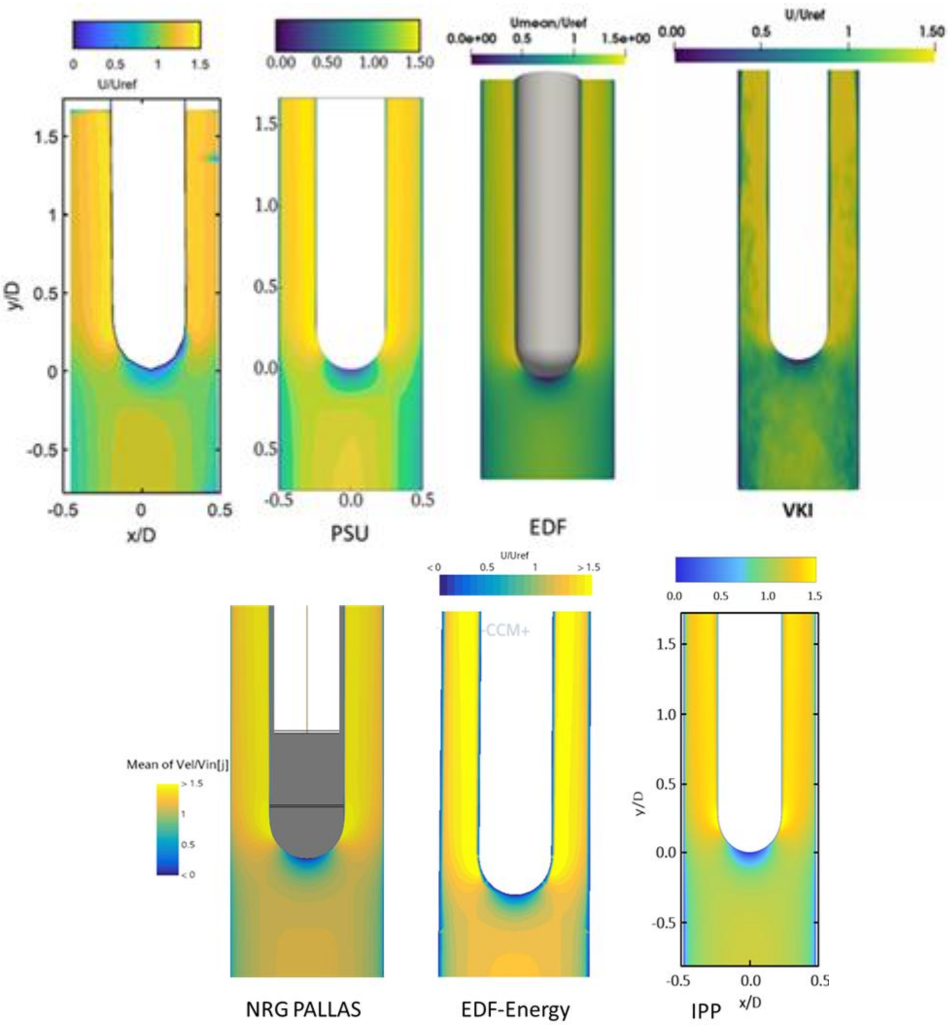

Figure 11. Comparison of Experimental (Cioncolini, et al., 2022) (top left) and Numerical Results for Non-dimensionalized Axial Component of Velocity

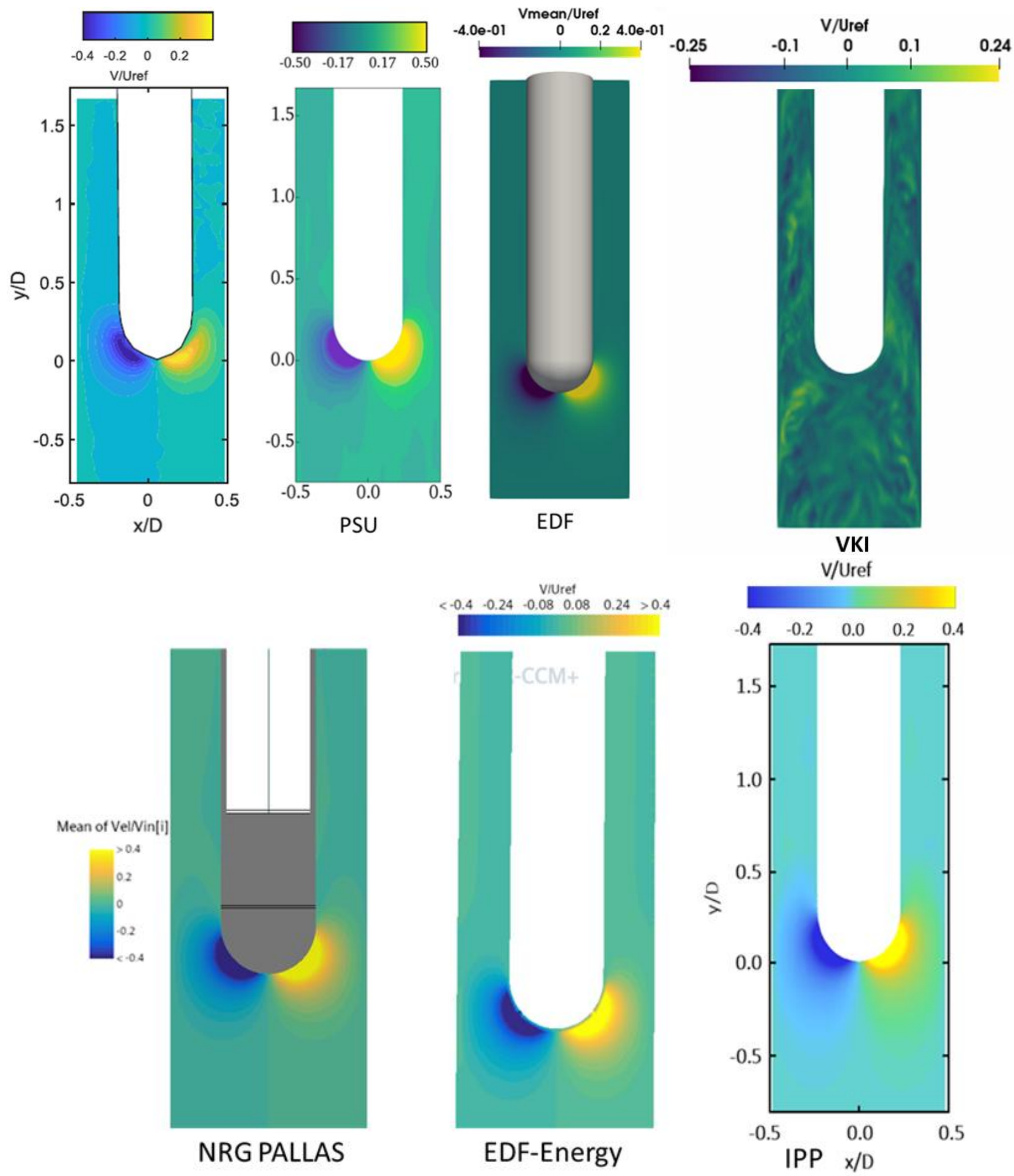

Figure 12. Comparison of Experimental (Cioncolini, et al., 2022) (top left) and Numerical Results for Non-dimensionalized Radial Component of Velocity

The time-averaged non-dimensional stress component contours are shown in Figure 13 for PSU and EDF, who performed high fidelity simulations. The numerical results are again found to be in good agreement with the experimental results and with each other.

Funded by
the European Union

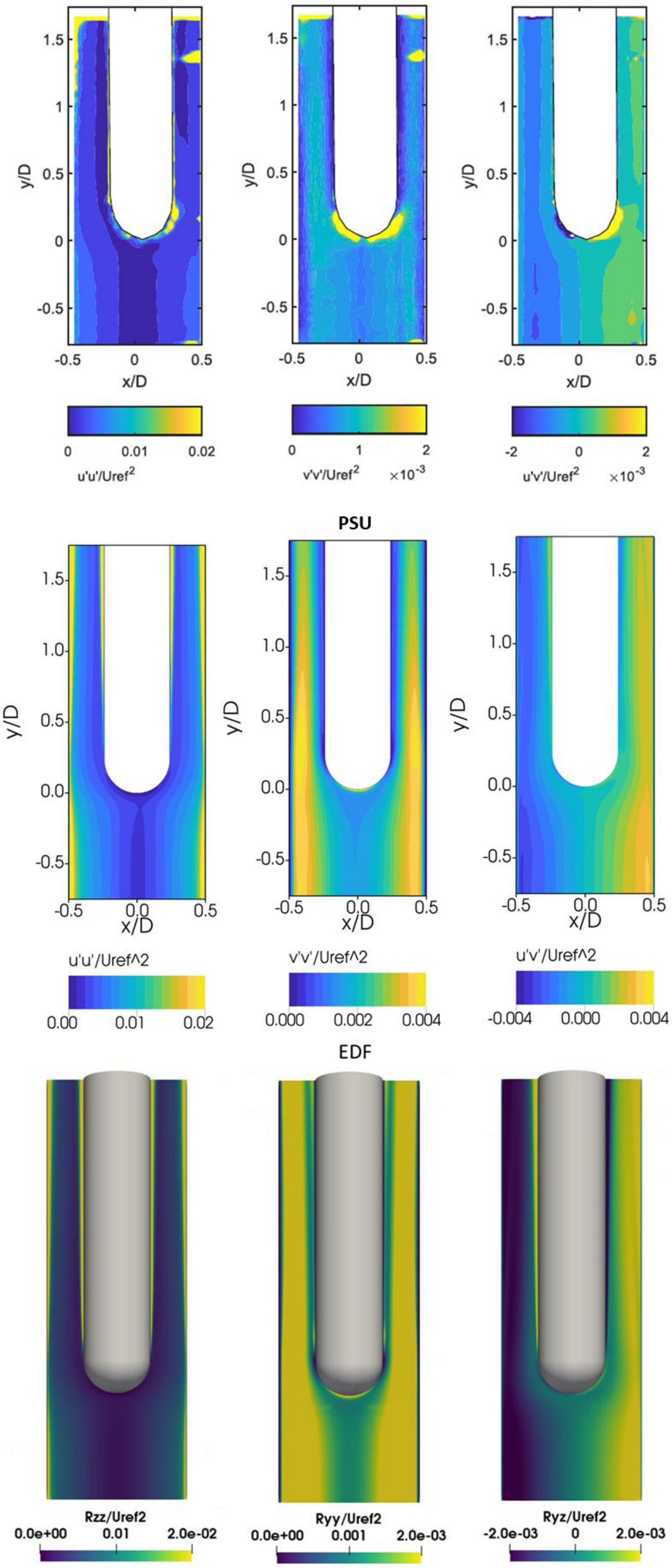

Figure 13. Comparison of Experimental (Cioncolini, et al., 2022) (top) and Numerical Results for Non-dimensionalized Stress Components

Several radial profiles at the PIV measurement locations are provided in Figure 14 to Figure 19. The PIV data inside of the beam are discarded owing to metallic reflections. The time-averaged axial and transverse velocity profiles are drawn. The experimental results for the axial velocity component show that as the fluid approaches the rod tip, the standard pipe flow profile transitions to that expected for annular flow. However, the experimental profiles also show clear asymmetry. This is reasoned by the potential offset in the vibrating rod tip from the axis of the confining pipe. This is later also confirmed with the rod vibration analysis in section 4.3.2.

Concerning the experimental results for the radial velocity component, at a large distance (15.6 mm) before the rod tip, the magnitudes are revealed to be quite low similar to that observed for the location 10D (Figure 9) before the rod tip as well as some scatter in the data close to the confining pipe wall. As the rod tip is approached, this component of velocity understandably increases indicating the flow accommodating itself in the annular cross-sectional area due to the obstruction of the rod. As with the axial velocity component, asymmetry in the profiles are observed which could be reasoned with the rod tip offset. In particular, for dissimilarity of the left and right profiles of Figure 18 and Figure 19, this is reasoned to be from a potential measurement error.

Concerning the numerical results, all numerical results predict a similar evolution of velocity component profiles moving towards the rod. Concerning the flow profiles, the effect of the choice of turbulence modelling appears to dictate its prediction. The attention is first brought to the axial component of velocity. The high fidelity approaches of PSU (DNS) and EDF (WR-LES) lead to results that are well in agreement with each other for all locations and especially with the experiment at a location 15.6 mm upstream of the rod (Figure 14) where the effect of the rod offset is not observed. The high fidelity approach of VKI (WR-LES) reveals wiggly and asymmetric profiles owing to insufficient time-averaging. The closest of the medium resolution approaches to these high fidelity solutions at locations of 15.6 mm (Figure 14) and 3.8 mm (Figure 15) are the results of EDF-Energy (SSG RSM) followed by results of similar accuracy by NRG PALLAS (K-Epsilon) and IPP (K-Omega SST).

Just before the rod tip (Figure 16), all numerical results agree with each other except at the center, where EDF-Energy predicts a higher minimum velocity, and at the peak values where VKI overpredicts compared to the other participants. At locations further downstream (Figure 17-Figure 19), all numerical results are also well in agreement with each other, with results in order of (slightly) decreasing agreement with high fidelity results being NRG PALLAS, EDF-Energy and IPP.

Observing the radial component of velocity, the observations are slightly different. Far away from the rod tip (Figure 14), the high fidelity solutions show different trends where EDF predicts a positive albeit small magnitude of radial velocity (flow moving rightward) while PSU predicts negative values in the left half and positive values in the right half, and VKI predicts mostly negative values with the exception of a zone near the right wall. The medium resolution results all show a smooth and symmetric profile with similar low magnitude predictions. Between them, NRG PALLAS and IPP (eddy viscosity models) are closer to each other compared to EDF-Energy (SSG RSM).

Moving further downstream in the vicinity of the rod tip (Figure 15-Figure 18), the high fidelity solutions show better agreement with the EDF solution being a bit more wiggly than the PSU solution, and the VKI solution being less affected by the insufficient time-averaging near the rod tip (Figure 16-Figure 17). The trends of the medium resolution results are similar to the high fidelity solutions but they increasingly underpredict the peak magnitudes moving downstream, with the exception of the location 6.7 mm downstream of the rod tip (Figure 18). This observation can thus be expected to hold in the vicinity of the rod tip, where the flow actively re-orients itself from pipe flow to annular flow. As observed earlier, the solutions of NRG PALLAS and IPP (eddy viscosity models) are closer to each other compared to EDF-Energy (SSG RSM), the latter also being more wiggly in comparison to the former two.

Funded by
the European Union

Moving even further away from the rod tip (Figure 19), all numerical results except VKI predict low magnitudes of radial velocity. However, the trend predicted by PSU is different compared to the other numerical results. This could be because of the fact that the effect of rod vibrations are not accounted for by PSU. The results of IPP and EDF-Energy are observed to be well in agreement with each other as well as with the high fidelity FSI approach solution of EDF. NRG PALLAS shows a similar trend but underpredicts compared to the EDF results at the location of peaks.

Compared to the experiment, all numerical results for the radial velocity component are observed to overpredict compared to the experimental results in the vicinity of the rod tip (Figure 15-Figure 17) while underpredicting further downstream (only the right half profile of Figure 18). In combination to what was observed for the axial flow component, it could be postulated that the numerical results predict a faster (meaning requiring lesser length) establishment of annular flow from pipe flow compared to the experiment.

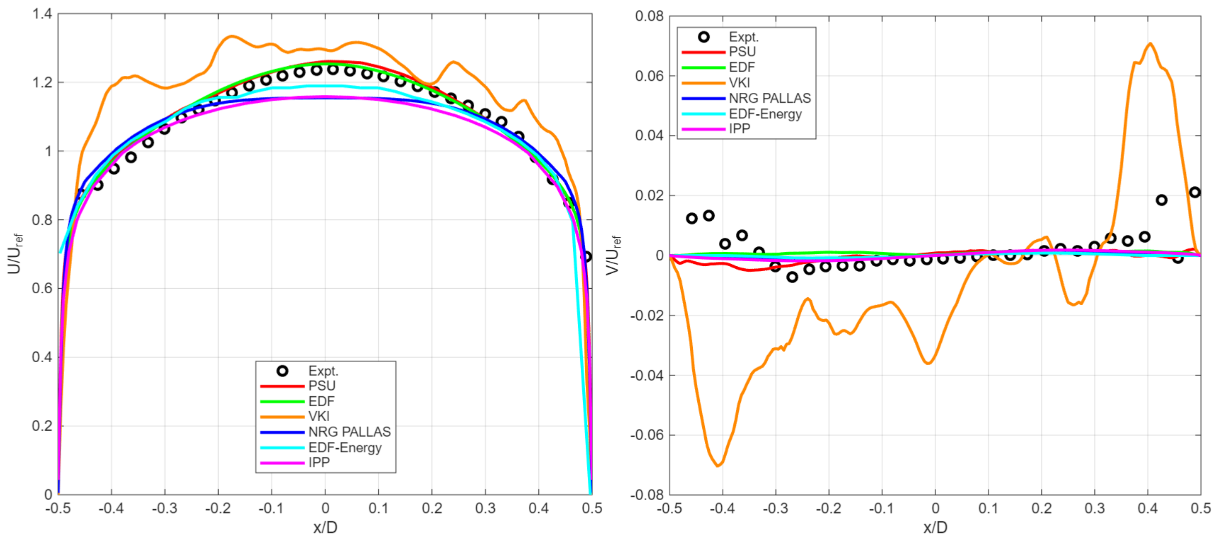

Figure 14. Time-Averaged Non-dimensional Axial (left) and Transverse (right) Velocity Profiles 15.63786 mm Upstream of the Rod Tip

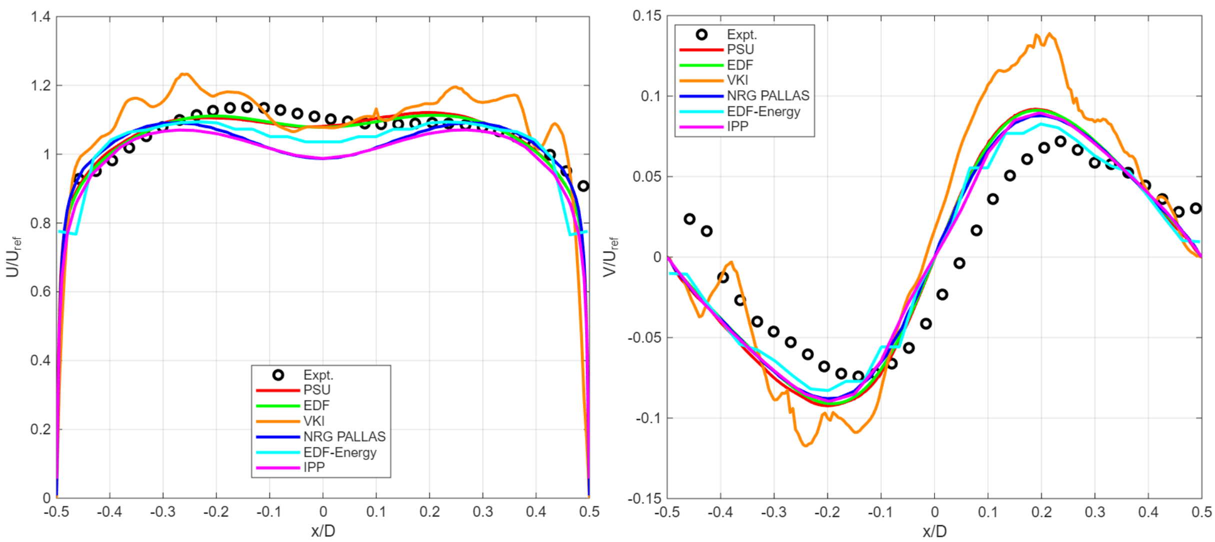

Figure 15. Time-Averaged Non-dimensional Axial (left) and Transverse (right) Velocity Profiles 3.786006 mm Upstream of the Rod Tip

Funded by
the European Union

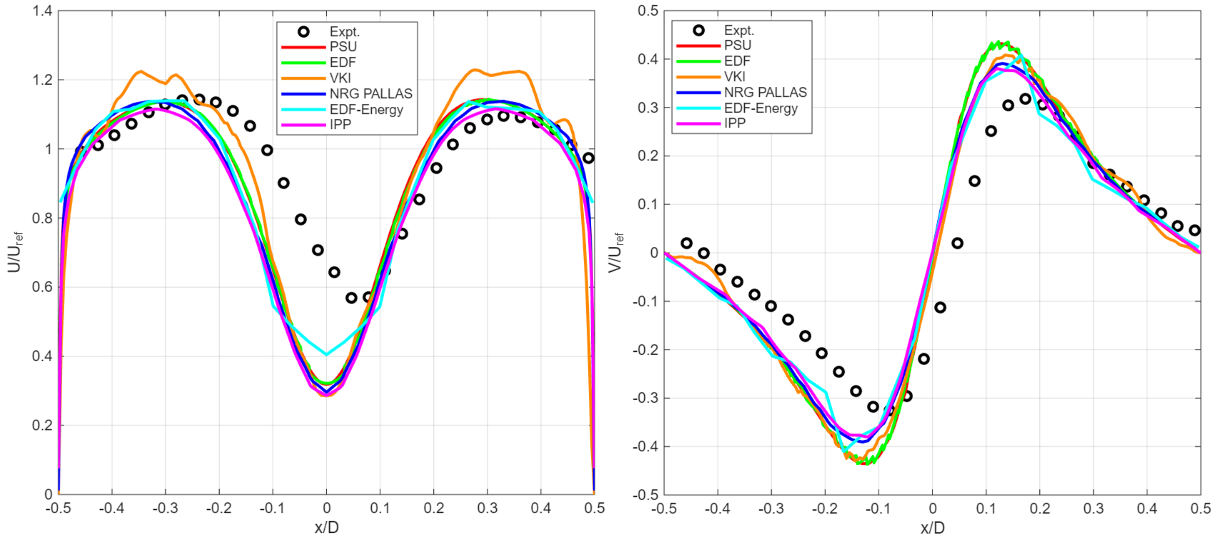

Figure 16. Time-Averaged Non-dimensional Axial (left) and Transverse (right) Velocity Profiles 0.493836 mm Upstream of the Rod Tip

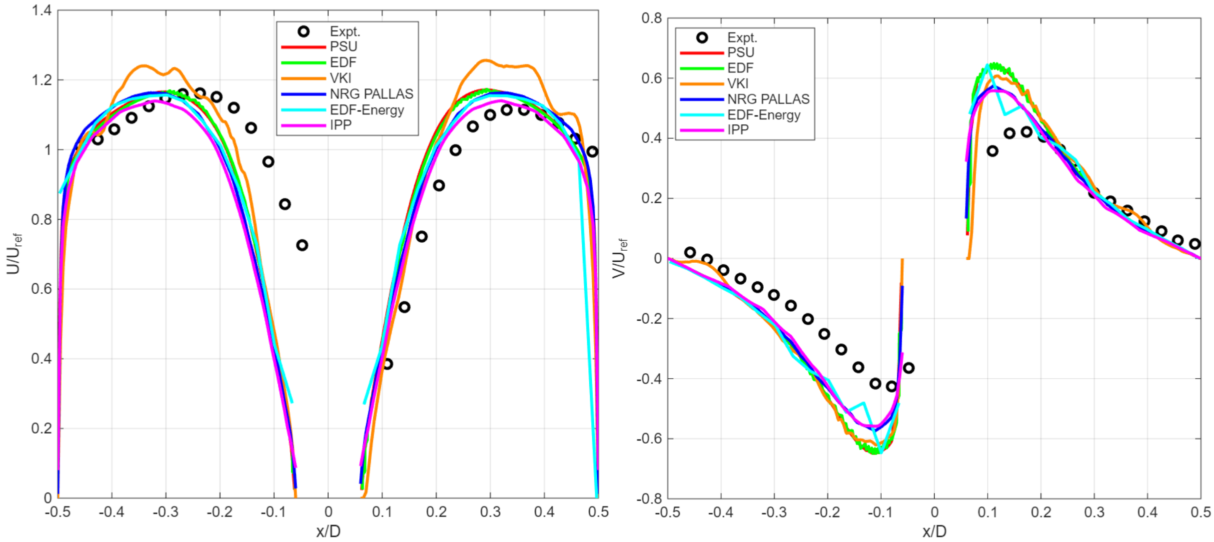

Figure 17. Time-Averaged Non-dimensional Axial (left) and Transverse (right) Velocity Profiles 0.164619 mm Downstream of the Rod Tip

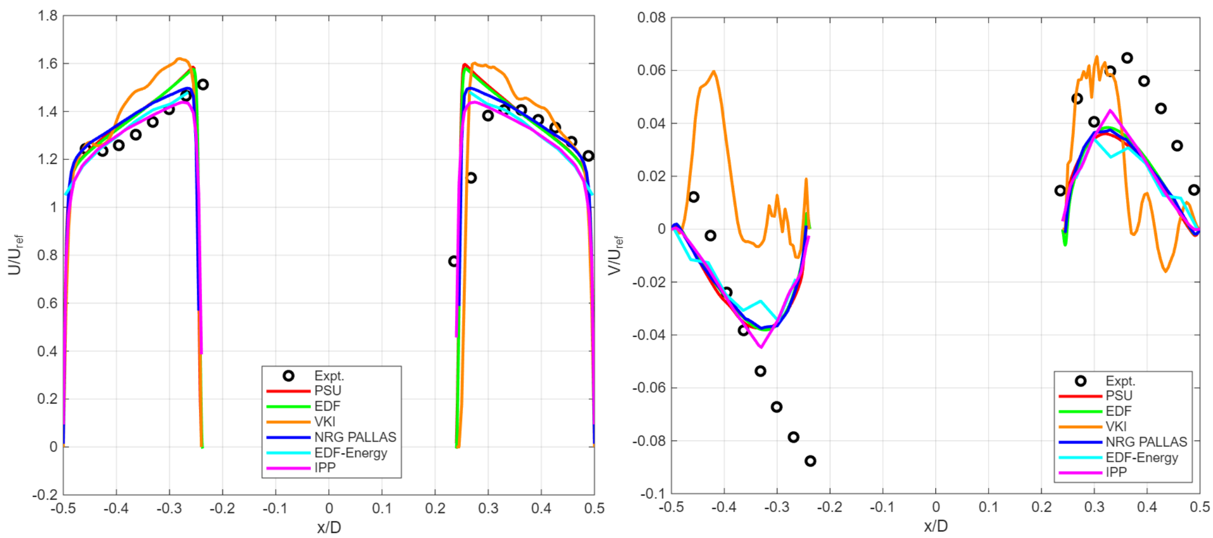

Figure 18. Time-Averaged Non-dimensional Axial (left) and Transverse (right) Velocity Profiles 6.74898 mm Downstream of the Rod Tip

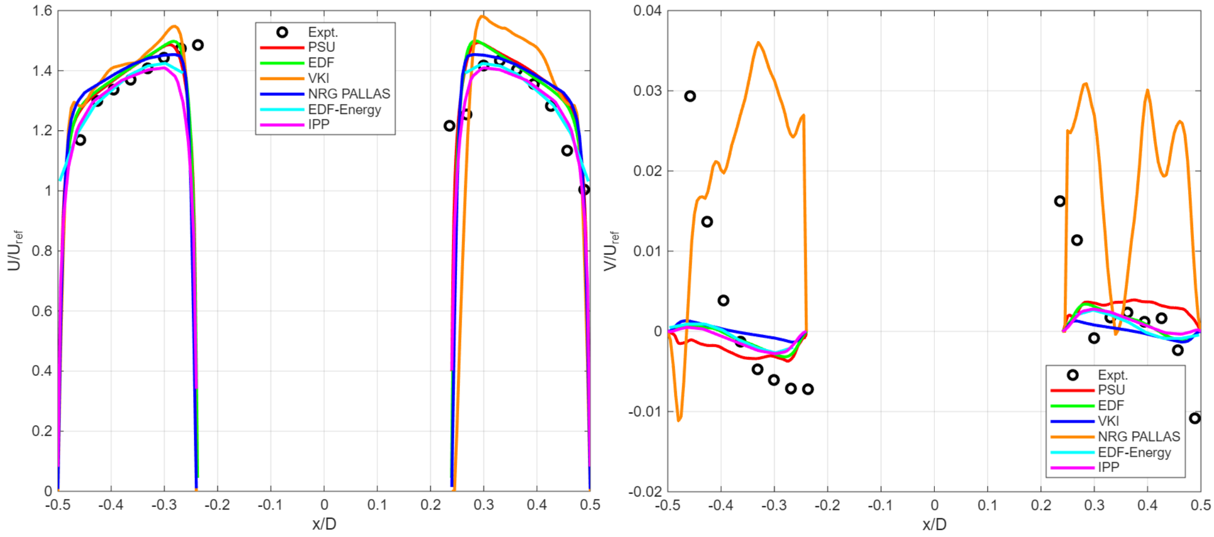

Figure 19. Time-Averaged Non-dimensional Axial (left) and Transverse (right) Velocity Profiles 29.135799 mm Downstream of the Rod Tip

Additional profiles concerning the time averaged second order statistics (u'v' and turbulent kinetic energy, TKE or k) are presented in Figure 20 through Figure 25, for the participants using high fidelity approaches. Considering the experimental PIV results for the u'v' data, they are observed to predict general trends, however owing to the aforementioned reasons, their magnitudes are expected to be severely underpredicted with respect to reality. The underestimation is likely most severe in the regions of highest energy and smallest scales least severe where turbulent scales are larger and more diffused.

This is also confirmed by observing the numerical results of PSU and EDF which provide similar profile trends but much higher magnitudes. The numerical results of VKI appear to be rather distorted for u'v' and highly underpredicted for TKE, not conforming to the trends of the experiment or other numerical results. This may be on account of the insufficient time-averaging or incorrect sampling of data. Further discussion is thus made considering only the PSU and EDF results.

The second order statistics clearly reveal the evolution of the boundary layer at the confining pipe wall as well as the rod surface through the peaks. Comparing the two high fidelity approach solutions, they show excellent agreement between them for the u'v' except for the location 29 mm downstream (Figure 25) and mostly showing good agreement also for the TKE, except the peaks in the boundary layer where the gap between the predictions of DNS and LES appear to increase moving downstream.

The curves of DNS also appear to be less smooth compared to LES, except at the location 0.16 mm downstream (Figure 23) where the LES result near the rod shows wiggles while DNS does not. DNS appears rougher because it resolves all scales (the true chaotic reality). The roughness suggests that the DNS simulation, despite its high cost, was perhaps not run for a long enough time to achieve perfect statistical convergence for the u'v' quantity in the highly unsteady region. As for the LES solution being jagged in Figure 23, it could be an indicator of an issue related to the WR-LES filtering process or the resolution of the grid. The wiggle is thus the numerical solution attempting to reconcile the physical turbulence with the limitations of the local grid.

Funded by the European Union

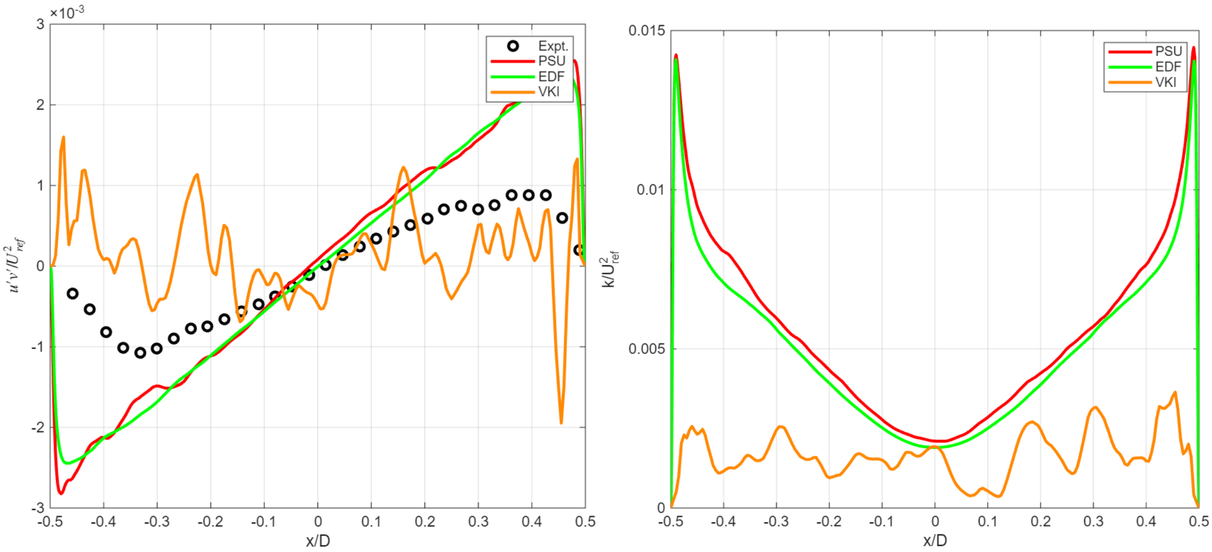

Figure 20. Time-Averaged Non-dimensional Reynolds Stress Component (u'v') (left) and Turbulent Kinetic Energy (right) Profiles 15.63786 mm Upstream of the Rod Tip

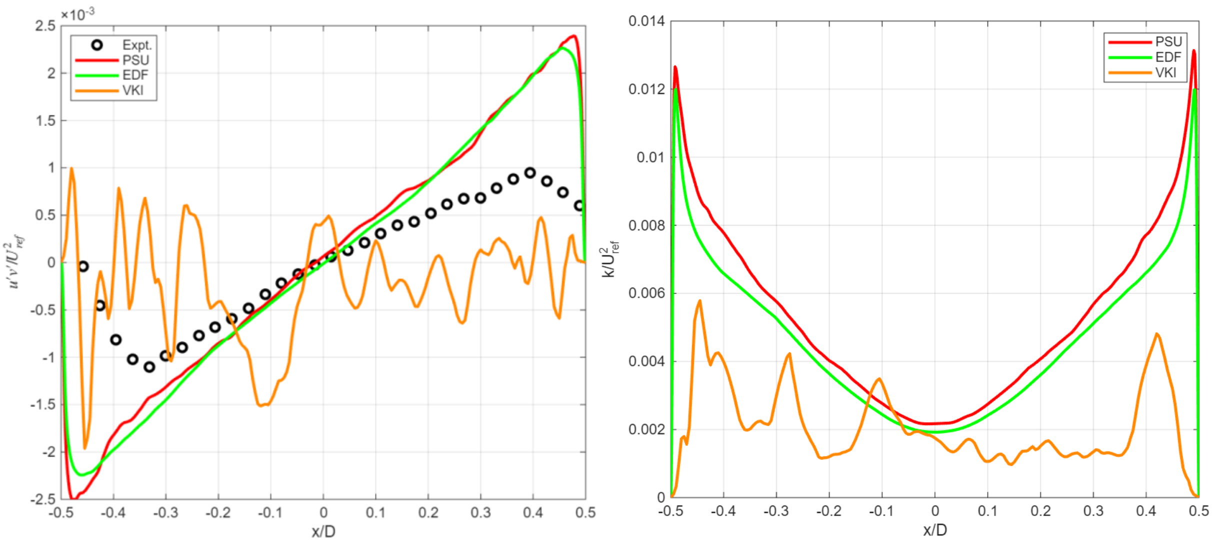

Figure 21. Time-Averaged Non-dimensional Reynolds Stress Component (u'v') (left) and Turbulent Kinetic Energy (right) Profiles 3.786006 mm Upstream of the Rod Tip

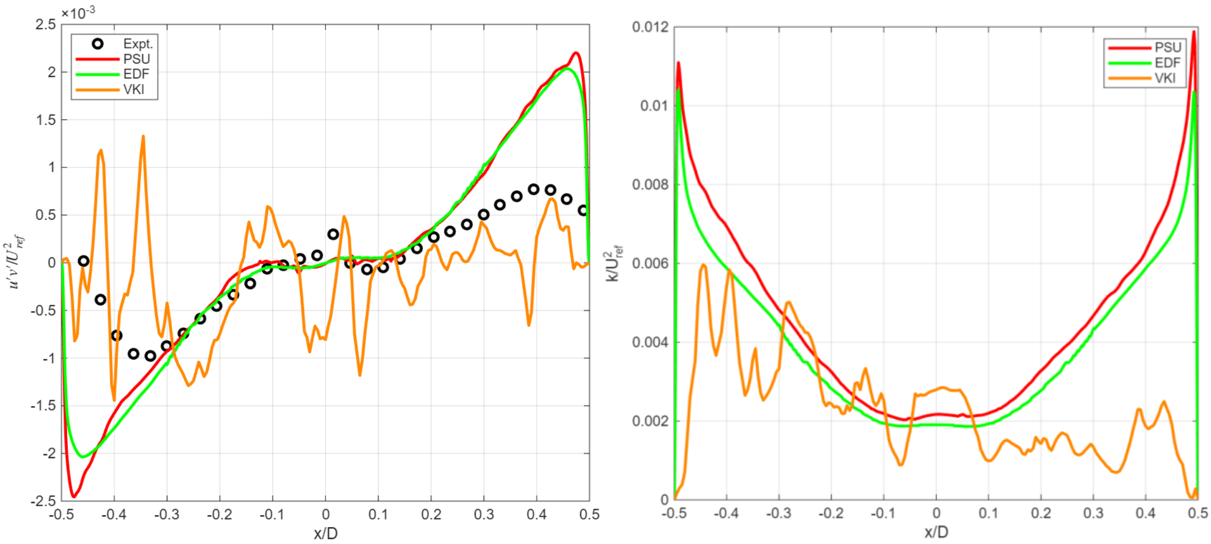

Figure 22. Time-Averaged Non-dimensional Reynolds Stress Component (u'v') (left) and Turbulent Kinetic Energy (right) Profiles 0.493836 mm Upstream of the Rod Tip

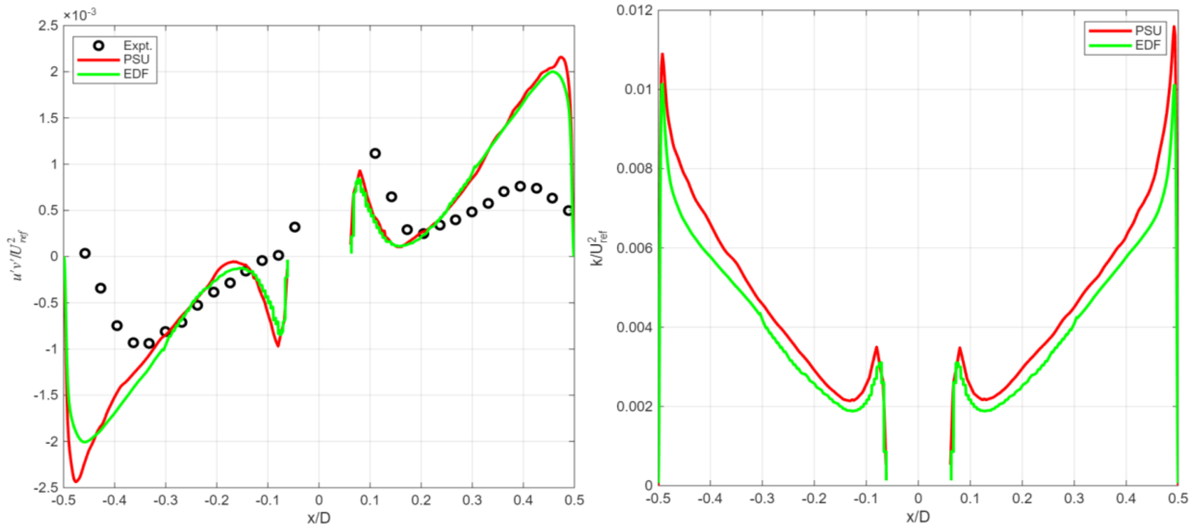

Figure 23. Time-Averaged Non-dimensional Reynolds Stress Component (u'v') (left) and Turbulent Kinetic Energy (right) Profiles 0.164619 mm Downstream of the Rod Tip

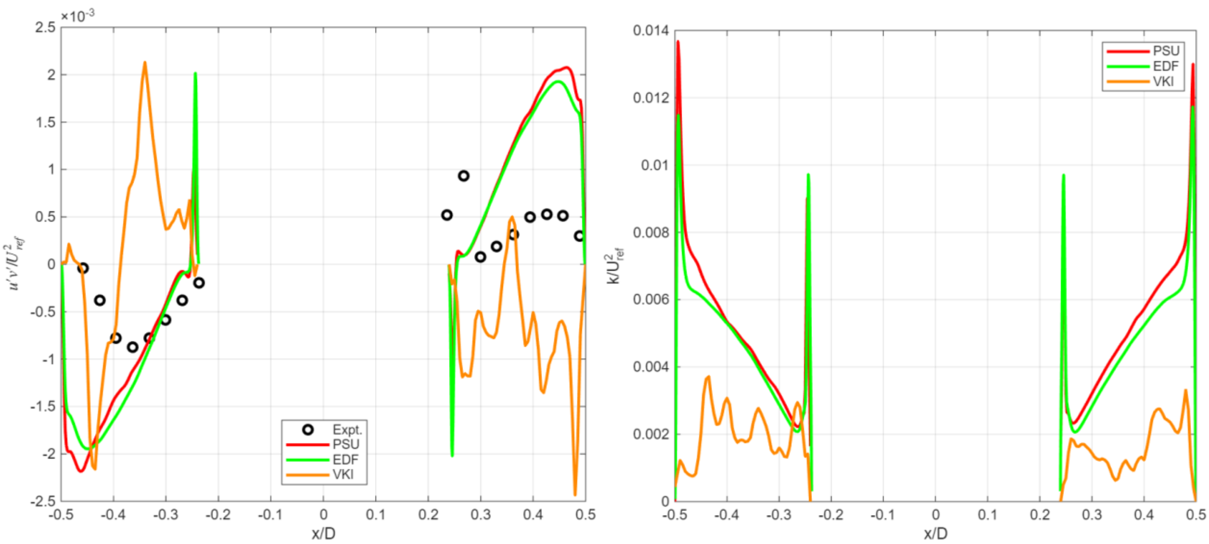

Figure 24. Time-Averaged Non-dimensional Reynolds Stress Component (u'v') (left) and Turbulent Kinetic Energy (right) Profiles 6.74898 mm Downstream of the Rod Tip

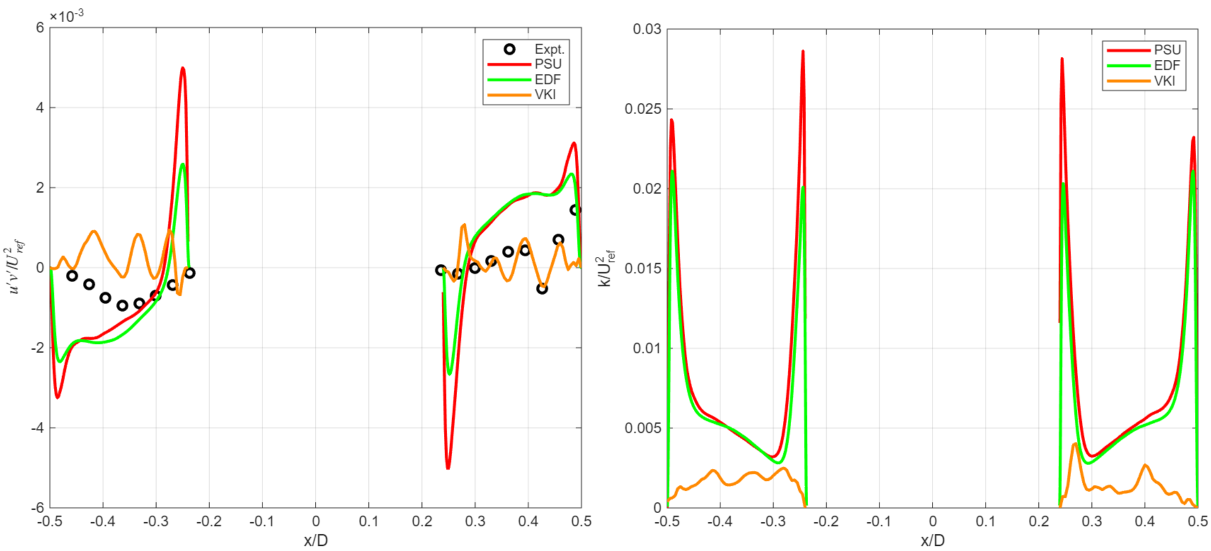

Figure 25. Time-Averaged Non-dimensional Reynolds Stress Component (u'v') (left) and Turbulent Kinetic Energy (right) Profiles 29.135799 mm Downstream of the Rod Tip

Funded by
the European Union

Vertical time-averaged profiles at the PIV measurement locations moving downstream from the rod tip elevation (non-dimensionalized by the rod diameter) are considered. These were recorded at different radial locations by the participants and are tabulated along with those of the experiment in Table 11. High fidelity solution data is available only for the positive locations while medium resolution solution data is also available at the negative locations. EDF provided data at positive radial locations slightly different from the rest of the participants as seen in Table 11.

Table 11. Vertical Profile Data Collection

Institution	Measurement Location, l (mm)	
	- : Left of Rod	+ : Right of Rod
PSU*		+5.583627, +6.242061, +7.558929
EDF		+5.60465, +6.27455, +7.56725
VKI		+5.583627, +6.242061, +7.558929
NRG PALLAS	-7.585095, -6.926661, -5.609793	+5.583627, +6.242061, +7.558929
EDF-Energy	-7.585095, -6.926661, -5.609793	+5.583627, +6.242061, +7.558929
IPP	-7.585095, -6.926661, -5.609793	+5.583627, +6.242061, +7.558929
Experiment	-7.585095, -6.926661, -5.609793	+5.583627, +6.242061, +7.558929

* Locations correspond to unscaled geometry. To get the location in the scaled geometry in 'm', use $l_{scaled} = l/21$

The solutions at the positive radial locations for the velocity components are presented in the top row in Figure 26 through Figure 28 while those for the negative radial locations are presented in the bottom row of the same figures. The experimental data for this comparison can only be used to determine the expected trend of the solution but not the expected magnitude. This is because some data suffers from metallic reflections and simply cannot be used, as in top plots of Figure 26 and Figure 27 for example, while the remaining data is not representative of the expected symmetric annular gap in the simulations owing to the rod tip offset, leading to unequal gaps on either side of the vibrating rod. This is confirmed by comparing the corresponding similar positive and negative locations in the experimental data, for example at +7.558929 mm and -7.585095 mm (Figure 28).

Focusing on the numerical results, it is observed that for the positive locations, the high fidelity solutions of EDF and PSU agree well with each other for both velocity components, taking into account the slightly different measurement location of EDF. The high fidelity solutions of VKI remain an outlier possibly on account of the insufficient time-averaging and are thus not used to judge the medium resolution approaches. For the medium resolution approaches, the agreement with the high fidelity data varies depending on the measurement location.

Near the rod wall at a position of ~+5.6 mm, the results of NRG PALLAS and EDF-Energy agree well with each other up to a height of z/d=2, beyond which differences are observed, where the EDF-Energy solution predicts a rate of decrease of axial velocity more in line with the high fidelity solution. IPP predicts the right trend but consistently underpredicts the axial velocity. For the radial velocity component, all medium resolution solutions are well in agreement with each other with differences noticed for the peak velocity. Here, IPP results match more closely to the high fidelity results than those of NRG PALLAS and EDF-Energy which underpredict the peak radial velocity.

Moving further away from the rod wall, at ~+6.2 mm, the axial velocity solutions in order of decreasing agreement (increasing underprediction) with the high fidelity results are NRG PALLAS, EDF-Energy and IPP. But for the radial velocity, the observation is the same as that of the ~+5.6 mm location.

Moving even further away from the rod wall at a location ~+7.5 mm, which is approximately halfway between the rod wall and confining pipe wall, the axial velocity plot reveals an almost overlapping profile of NRG PALLAS compared to the high fidelity solutions followed by EDF-Energy and IPP in order of increasing underprediction. For the radial velocity, the observation is different than the previous locations. While the general trends all agree well with each other, it is observed that for the peak radial velocity, NRG PALLAS agrees in the prediction to the high fidelity solutions, while EDF-Energy underpredicts and IPP overpredicts the same.

For the negative radial locations, the trends of the axial velocity are found to be similar to the positive location counterparts while the radial velocity shows a different profile but this is simply due to the sign convention where the flow now moves leftward in this region.

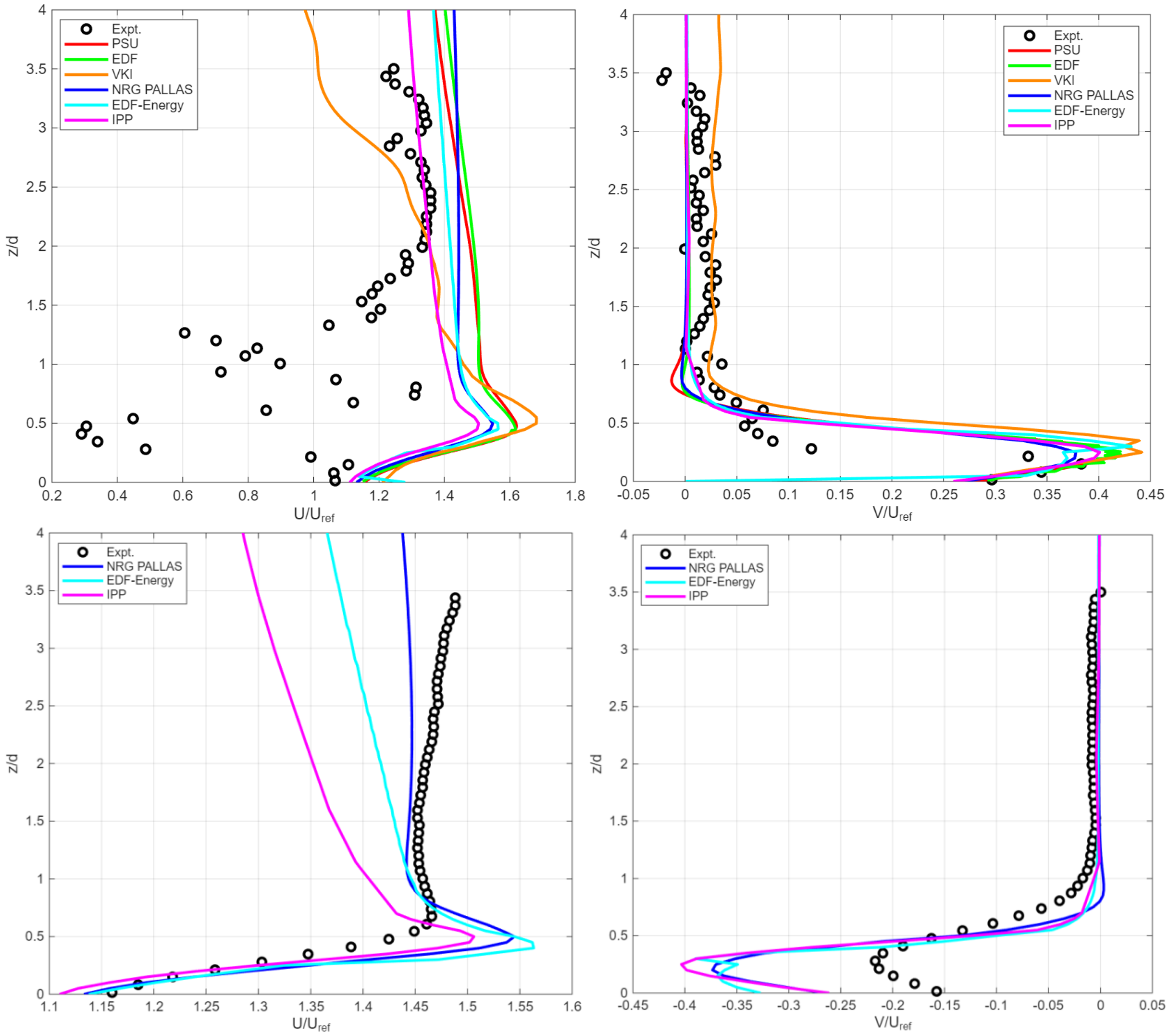

Figure 26. Time-Averaged Non-dimensional Axial (left) and Transverse (right) Velocity Profiles. Top: at Locations +5.583627 mm (Experiment, PSU, VKI, NRG PALLAS, EDF-Energy, IPP) and +5.60465 mm (EDF); Bottom: at Locations -5.609793 mm (Experiment, NRG PALLAS, EDF-Energy, IPP)

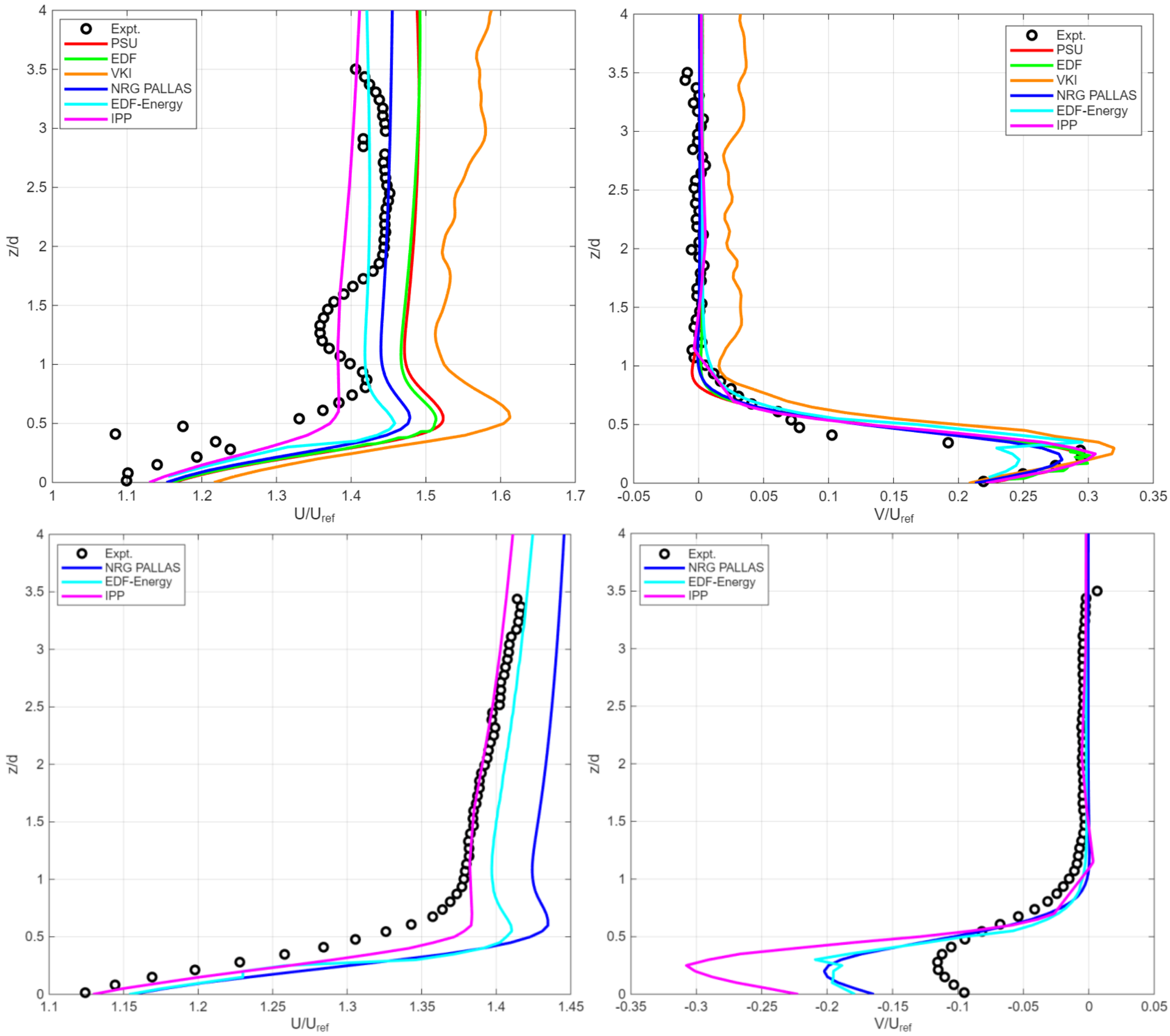

Figure 27. Time-Averaged Non-dimensional Axial (left) and Transverse (right) Velocity Profiles. Top: at Locations +6.242061 mm (Experiment, PSU, VKI, NRG PALLAS, EDF-Energy, IPP) and +6.27455 mm (EDF); Bottom: at Locations -6.926661 mm (Experiment, NRG PALLAS, EDF-Energy, IPP)

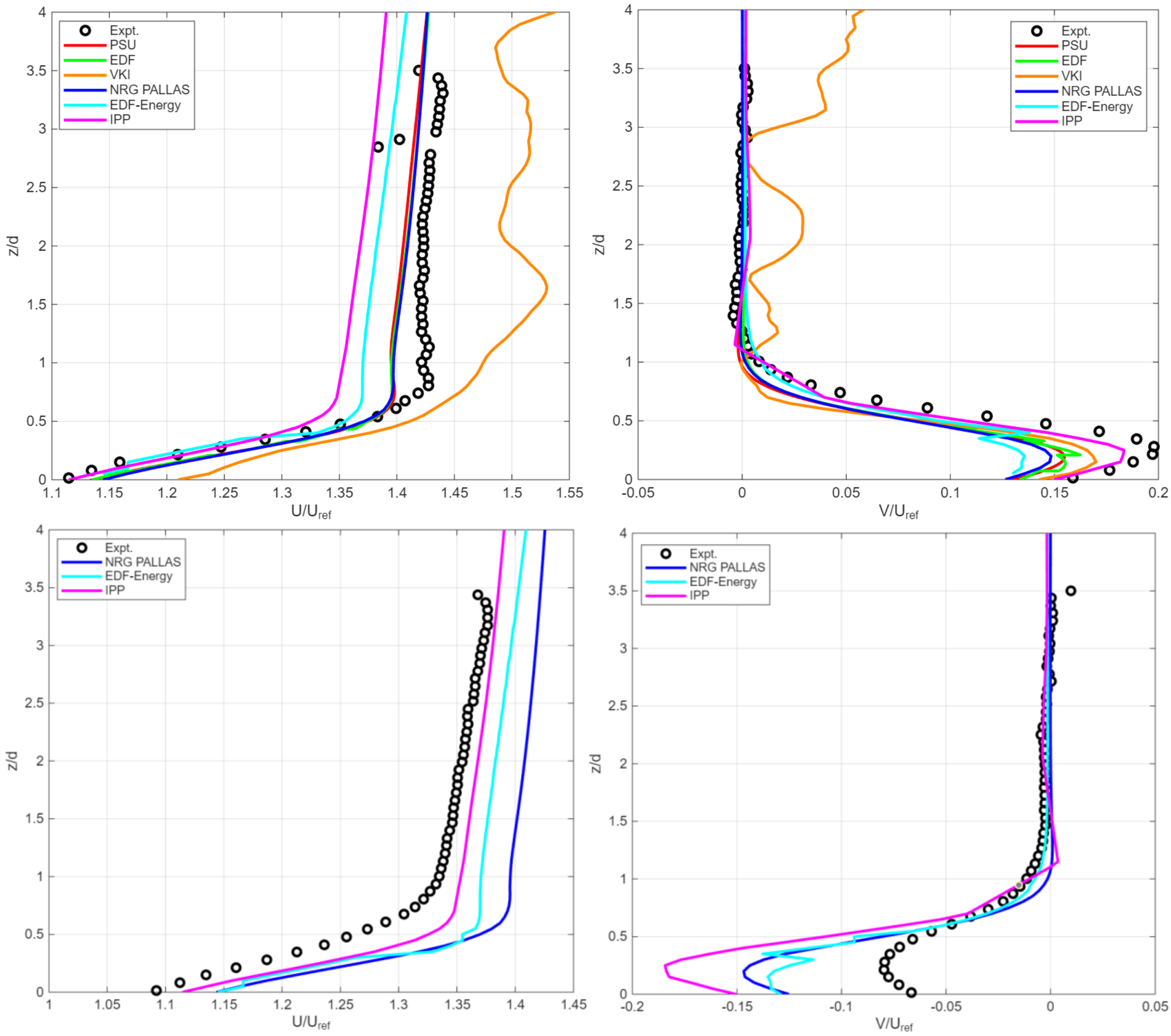

Figure 28. Time-Averaged Non-dimensional Axial (left) and Transverse (right) Velocity Profiles. Top: at Locations +7.558929 mm (Experiment, PSU, VKI, NRG PALLAS, EDF-Energy, IPP) and +7.56725 mm (EDF); Bottom: at Locations -7.585095 mm (Experiment, NRG PALLAS, EDF-Energy, IPP)

At the positive locations where high fidelity data is available, second order statistics (u'v' and TKE) are also considered along with experimental data. These are plotted in Figure 29 through Figure 31. The experimental results cannot be used for validation of numerical results owing to the rod tip offset in the experiment as well as the aforementioned hypothesis that the current PIV is not very reliable concerning second order statistics. The VKI results remain an outlier for the aforementioned reason of insufficient time-averaging. It is also seen that the TKE is generally underpredicted compared to the other two results conforming to the earlier observations from the horizontal profiles (Figure 20 through Figure 25).

The remaining two high fidelity results agree well in terms of the observed trends and also for the magnitude of the evolution of u'v' which gets better in agreement moving away from the rod wall. However, the TKE plots show solutions of similar magnitudes but with the EDF solution consistently underpredicting compared to the PSU solution. While part of the discrepancy can be explained by the slight mismatch in measurement location, it is not sufficient, since gaps were also observed in the TKE comparison of the horizontal profiles at the same measurement locations.

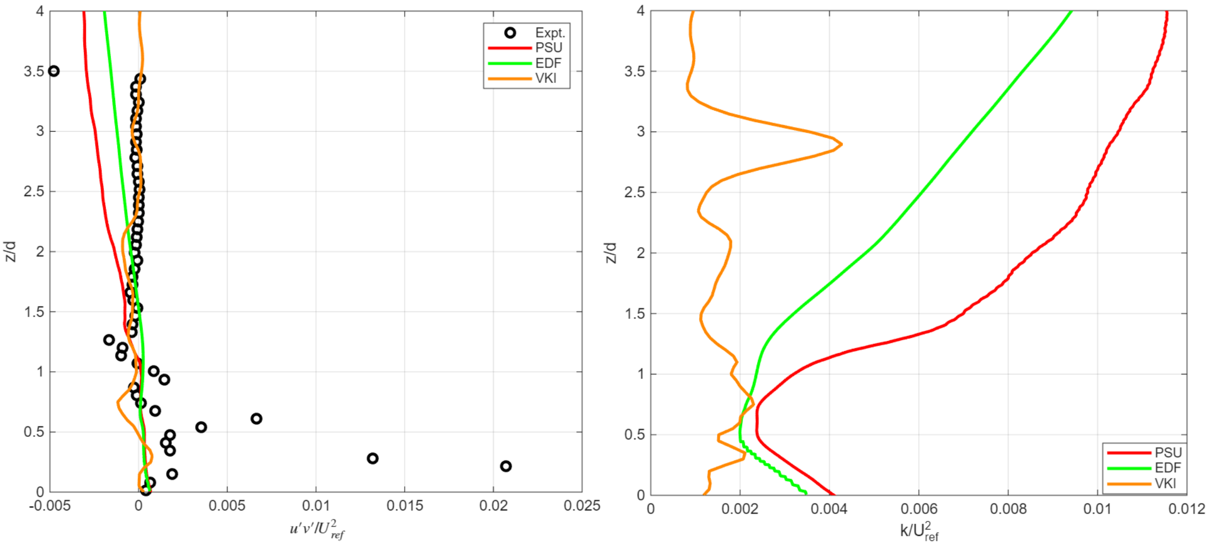

Figure 29. Time-Averaged Non-dimensional Reynolds Stress Component (u'v') (left) and Turbulent Kinetic Energy (right) Profiles at Location +5.583627 mm (Experiment, PSU, VKI) and +5.60465 mm (EDF)

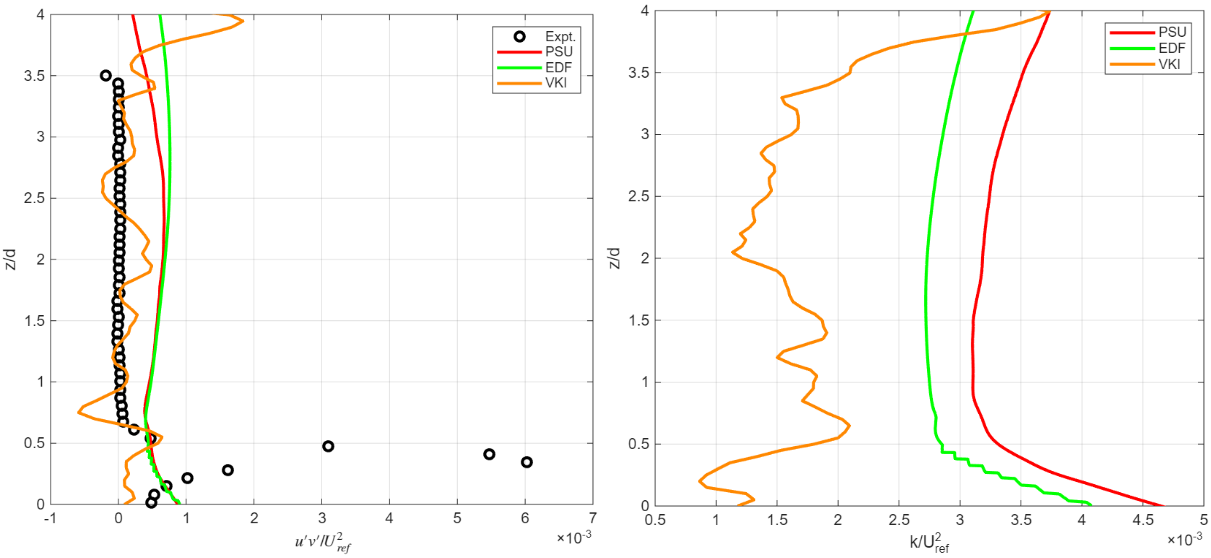

Figure 30. Time-Averaged Non-dimensional Reynolds Stress Component (u'v') (left) and Turbulent Kinetic Energy (right) Profiles at Locations +6.242061 mm (Experiment, PSU, VKI) and +6.27455 mm (EDF)

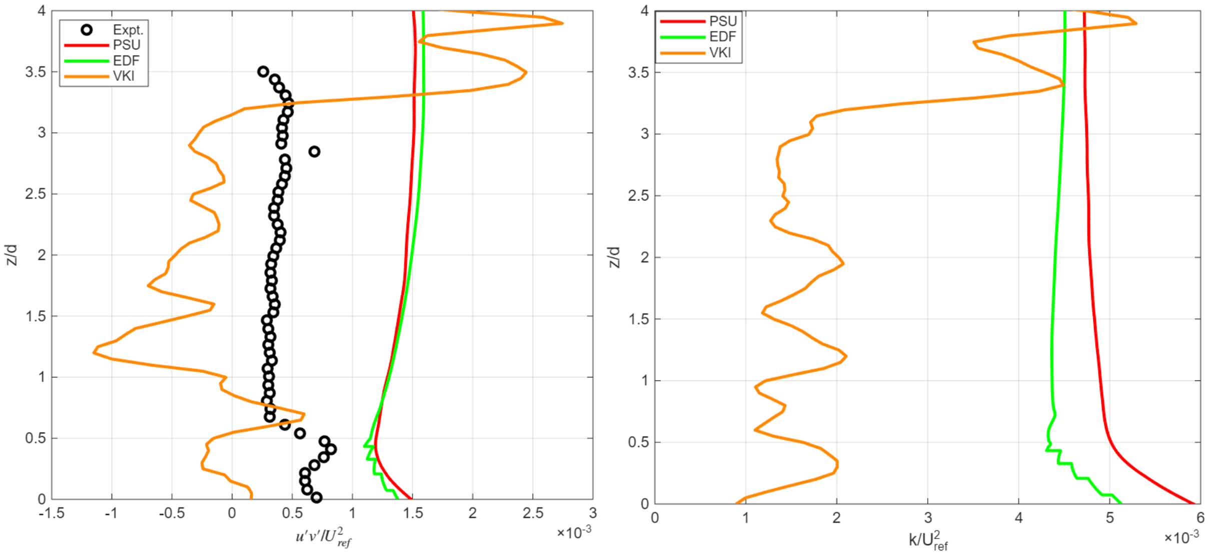

Figure 31. Time-Averaged Non-dimensional Reynolds Stress Component (u'v') (left) and Turbulent Kinetic Energy (right) Profiles at Locations +7.558929 mm (Experiment, PSU, VKI) and +7.56725 mm (EDF)

4.3.2 Vibration Data Comparison

The motion of the rod tip has been monitored during the simulations for all participants except PSU who performed pure CFD simulations. Each participants performed simulations for unequal durations of physical time depending on the available resources. The time histories obtained from the simulations are compared against the experiment in Figure 32. The displacements are non-dimensionalized using the rod diameter. Both the experimental and numerical results were centered about the 0 axis by removing the mean of the data excluding the initial transient. This is unique for each submission depending on the simulation strategy.

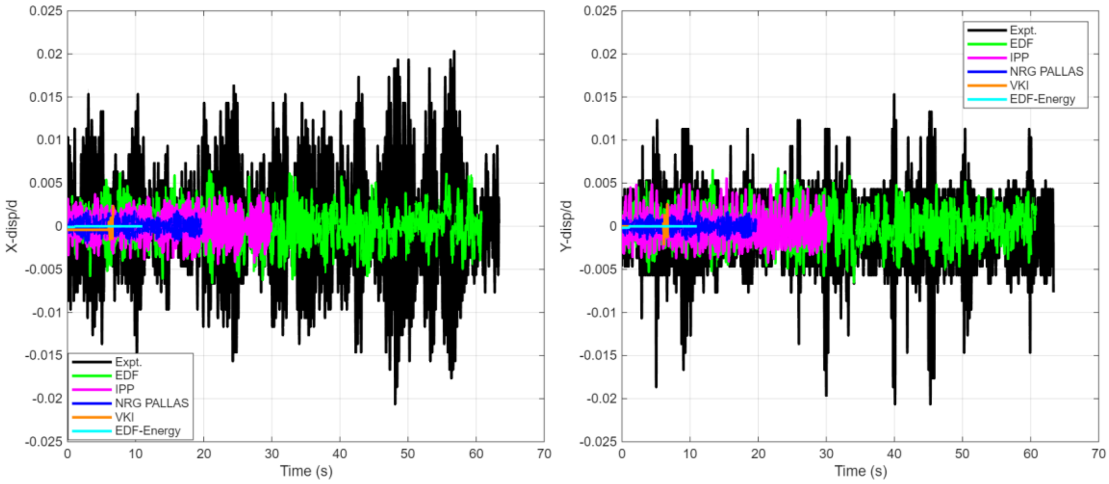

Figure 32. Time History of the Non-dimensional Rod Tip Front (left) and Side (right) Displacements

The obtained time histories are also presented as 3D plots in Figure 33 without removing the mean for the numerical results. Qualitatively, the numerical results show the same chaotic pattern as the experiment with the exception of EDF-Energy, whose displacements are very small compared to the already small numerical offset, and VKI, who has too short of an FSI run to judge accurately.

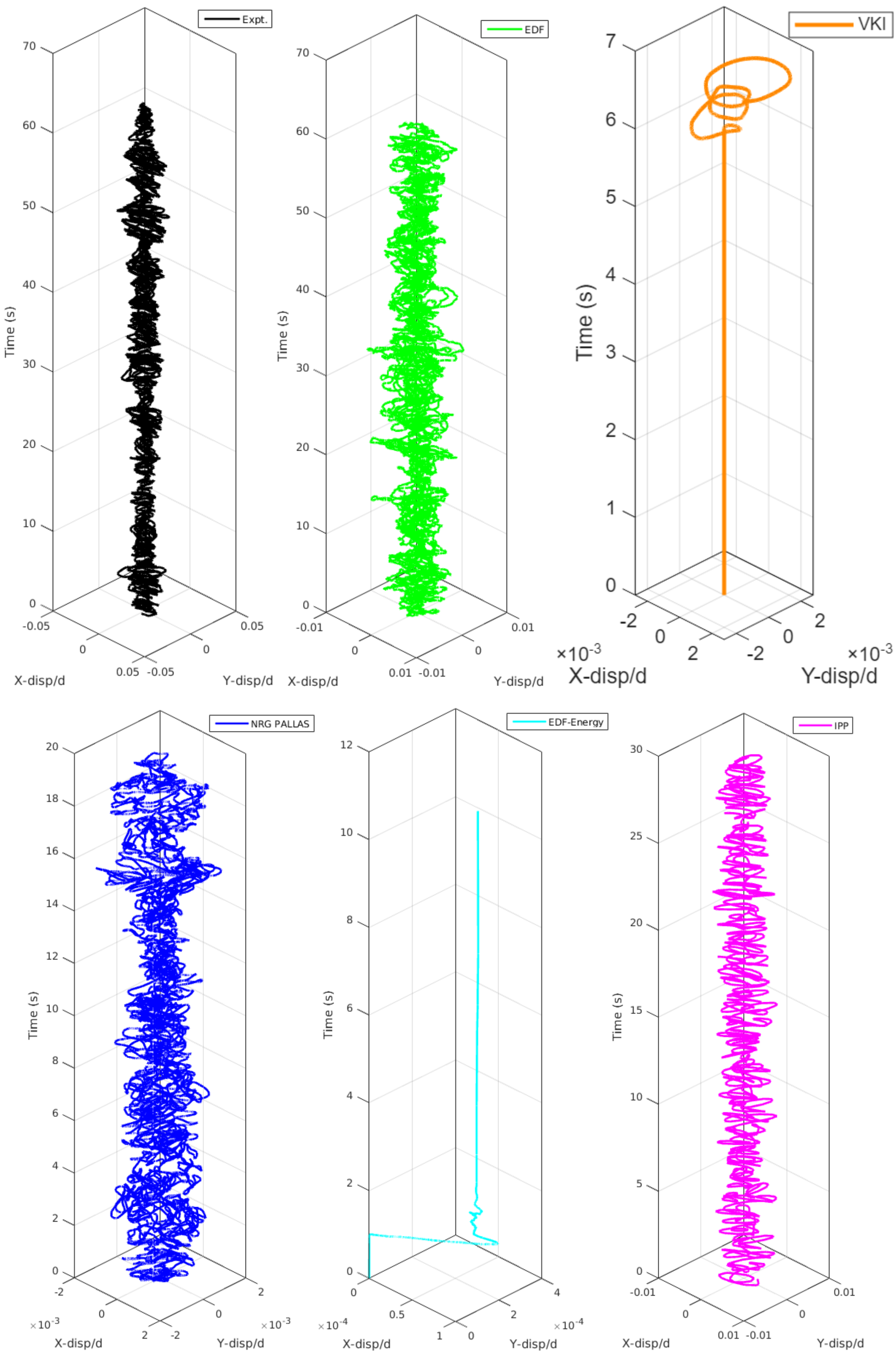

Figure 33. 3D Time History of Rod Tip Displacements

During the procedure, it was found that the rod tip was oscillating at an offset in the experiment and the numerical results. This is tabulated in Table 12. The numerical offsets are much smaller in comparison to the experiment and are considered to be a numerical artifact.

Table 12. Observed Rod Tip Offset

Institution	Front-Offset (mm)	Side-Offset (mm)	Net Offset (mm)
EDF	0.00088232	0.001089	0.0014
VKI	0.0040718	0.000082608	0.0041
NRG PALLAS	0.0018765	-0.0015263	0.0024
EDF-Energy	0.0008038	0.0018157	0.0020
IPP	0.0021148	-0.00036823	0.0021
Experiment	1.47675	0.02654	1.4770

Key results obtained from the time history are presented in Table 13. The RMS polar displacement is numerically predicted to be smaller than the experiment. The predictions are closest by EDF which is expected given the use of the high resolution approach, with an underprediction of a factor of 2.87. The next is IPP with displacement in the same order of magnitude as EDF, which is remarkable considering the use of medium resolution approach and a coarse time step size. The underprediction is by a factor of 3.34. Next is the high fidelity approach of VKI with an underprediction factor of 5.42. NRG PALLAS who also use a medium resolution approach but using a composite rod model underpredict the displacement by an order of magnitude or a factor of 9.84. EDF-Energy underpredicts vibrations by 4 orders of magnitude or, more precisely, a factor of 9492.73.

The RMS front (x-) and side (y-) displacements are found to be very dissimilar for the experiment and the numerical predictions except for EDF. This could stem from the rod tip offset which was significant for the experiment. For the numerical results, the asymmetry in the simulated test section of NRG PALLAS and IPP may have had a role. However, this is not applicable for EDF-Energy and VKI who also predict different displacements in both directions, although the displacements of EDF-Energy can be considered to be in the range of numerical noise. For VKI, the short FSI sampling or simplified rigid body motion of the straight rod may also have had a role to play.

Table 13. Obtained Displacement Results:

Institution	RMS X-Disp. (μm)	RMS Y-Disp. (μm)	RMS Polar Disp. (μm)
EDF	20.4478	19.2663	28.0945
VKI	9.5732	11.4100	14.8941
NRG PALLAS	6.1213	5.4553	8.1994
EDF-Energy	0.0073	0.0044	0.0085
IPP	16.1641	17.9912	24.1860
Experiment	64.7558	48.138	80.6882

The Power Spectral Density (PSD) of the rod tip front (x-) displacement is compared to the experimental data in Figure 34. The number of time steps simulated by the participants affects the frequency range which can be represented. Since IPP simulated only 1500 time steps, only frequency data upto 25 Hz is available. In general, the numerical trends themselves agree well with the experiment and each other. However, the numerical results are mostly found to be lower in energy content compared to the experiment to varying degrees depending on the participant.

Funded by
the European Union

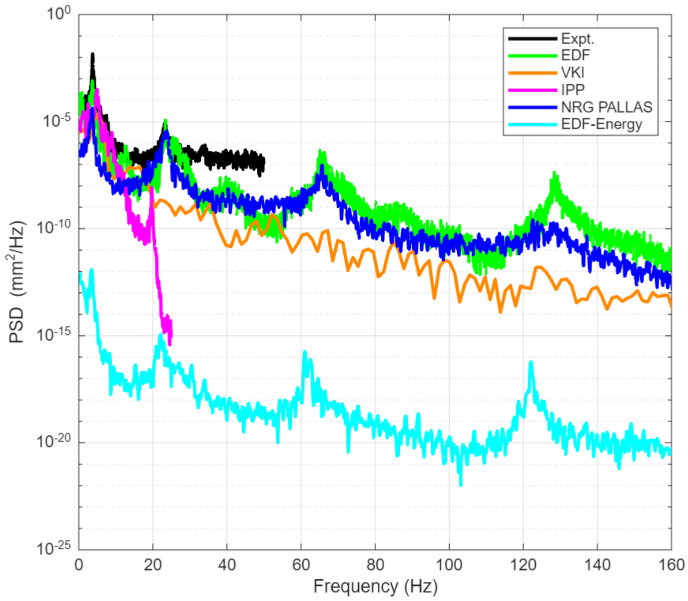

Figure 34. PSD of the Tip Displacement in the Front (x-) Direction

For the first peak, EDF and IPP show similar underpredictions followed by NRG PALLAS and VKI. For the second peak, EDF slightly overpredicts the energy level while NRG PALLAS slightly underpredicts it followed by IPP who have larger underpredictions. For the remaining frequency range, NRG PALLAS makes predictions in the same ball park as EDF but with the discrepancy increasing with increasing frequency. This is followed by VKI with a further underpredicted curve. EDF-Energy is observed to consistently show severe underprediction of the energy content throughout the frequency range which is expected considering the RMS values.

The frequencies of the peaks obtained numerically, experimentally and analytically via classical Euler-Bernoulli beam theory (refer section **Fehler! Verweisquelle konnte nicht gefunden werden.**) are provided in Table 14. Given VKI's small time step size, the frequency range issue of IPP is not a problem, however, the low FSI calculation time makes it a challenge to pick the peaks after the first one as all are at the level of noise. For the first two peaks available in the experimental data, the numerical predictions show agreements in the decreasing order of EDF, NRG PALLAS, EDF-Energy, IPP and VKI. For the higher frequency peaks, NRG PALLAS and EDF show good agreement with each other followed with the predictions being lower by EDF-Energy. In all cases, the peak frequencies significantly differ from the analytical solution at higher modes of natural frequencies.

Table 14. Frequencies of the Numerical and Experimental Front Displacement PSD Peaks Compared to the Beam Natural Frequencies Obtained Analytically

Approach	#1 (Hz)	#2 (Hz)	#3 (Hz)	#4 (Hz)
EDF	3.70	23.42	65.13	128.4
VKI	5.48	NA	NA	NA
NRG PALLAS	3.64	23.81	65.68	128.2
EDF-Energy	3.50	22.12	61.00	122.0
IPP	5.00	19.67	N/A	N/A
Experiment	3.76	23.47	N/A	N/A
Analytical	3.71	25.6	71.8	141

Funded by the European Union

A similar look is also taken for the rod tip side (y-) displacement as shown in Figure 35. Only the first peak is distinctly visible in the experimental results while the numerical results show a very similar trend as the front displacement (Figure 34). The first mode frequency for both directions is summarized in Table 15. The frequencies obtained from the front and side displacement are similar in the experiment, VKI, and EDF-Energy results, show slight dissimilarity for EDF and NRG PALLAS results, and show significant dissimilarity for IPP results. For the average frequency, the numerical predictions show agreements in the decreasing order of EDF, NRG PALLAS, EDF-Energy, IPP and VKI to the experimental and analytical value.

Table 15. Frequencies of the Numerical and Experimental Side Displacement PSD Peak #1 Compared to the Beam Natural Frequencies Obtained Analytically

Approach	Front (Hz)	Side (Hz)	Average (Hz)
EDF	3.70	3.80	3.75
VKI	5.48	5.48	5.48
NRG PALLAS	3.64	3.71	3.68
EDF-Energy	3.50	3.50	3.50
IPP	5.00	1.50	3.25
Experiment	3.76	3.71	3.73
Analytical	3.71	3.71	3.71

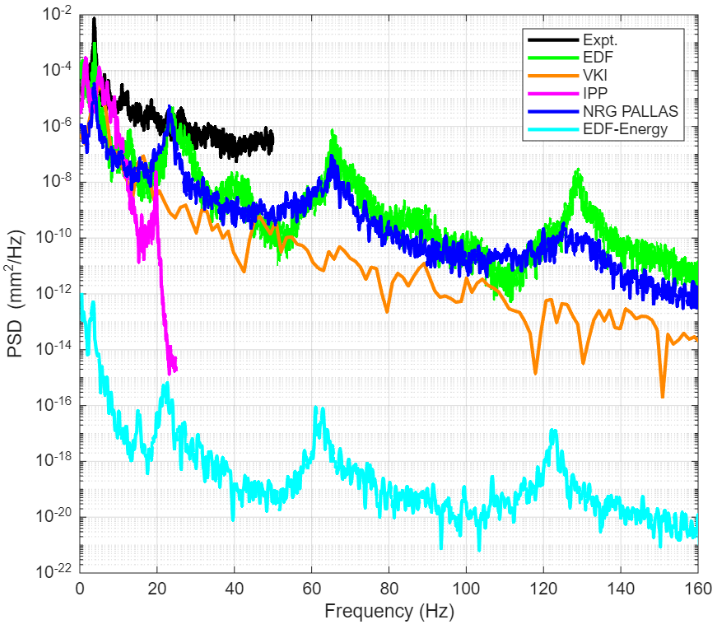

Figure 35. PSD of the Tip Displacement in the Side (y-) Direction

4.4 Benchmark summary and conclusions

In this chapter, the benchmark case, chosen to be the free-clamped flow at Re=21.2k for the rod with a hemispherical tip, was discussed. Six participants provided their results for comparison: PSU, EDF, VKI, NRG PALLAS, EDF-Energy and IPP. Each participant used different modelling approaches: pure CFD vs two-way FSI, the simulated geometry respecting the experimental test section or modifying it, modelling of the vibrating rod, differences in material properties, meshing strategy and lastly but most importantly the turbulence modelling of the fluid.

Funded by
the European Union

Such a wide range of differences make the benchmark quite rich, but it also brings forth the challenge of identifying a single aspect of the simulation strategy that can be said to make or break the accuracy of the calculations. However, based on the compared results the following key comments can be made:

- Flow Field Accuracy:
    - To obtain high accuracy results with a focus only on flow field data, comparing solely the high fidelity approaches, it appears to be more fruitful to go for a pure CFD approach with DNS than a two-way FSI with LES.
    - From the medium resolution approaches of SSG-RSM, K-Epsilon (cubic), and K-Omega SST, there is no clear "best" model that provided solutions close to the high fidelity solution at all locations.
    - For horizontal measurement profiles, the classical eddy viscosity models (K-Epsilon (cubic) and K-Omega SST) performed similarly while differences were observed in the vertical measurement profiles. SSG-RSM performed either slightly better than the eddy viscosity models or somewhere in between in terms of accuracy.
- Vibration Accuracy:
    - As one expects, the better your flow prediction, in particular, pressure and stresses is over the rod, the better would be the accuracy of the vibration amplitudes. The LES results of EDF conformed to this expectation with being the closest to the experimental data amongst the participants. However, it is still to be remarked that this "best solution" still underpredicted the RMS vibration amplitude by a factor of 2.8 with subsequent participants' medium resolution solutions further degrading in accuracy. The LES approach of VKI needs a longer run time to draw conclusions.
    - However, the above expectation is not met within the medium resolution results. SSG-RSM approach ended up with vibration amplitudes several orders of magnitude lower than the experimental results. This is suspected to be connected to the mesh being wall modelled rather than wall resolved. The eddy viscosity models approach were much better but still either underpredicted the amplitude by an order of magnitude for the K-Epsilon (cubic) approach or by a factor of 3.3 for the K-Omega model, which is quite good considering how LES performed.
    - Concerning the vibration frequency, all approaches provide a good estimate for the same compared to the experiment except the one using the K-Omega SST approach and LES approach of VKI. It is quite peculiar that for the former, the prediction of vibrating frequency in the two principle directions were so starkly different, while for the latter the frequencies were equally overpredicted. Of course, it is not just the turbulence model which could have led to this result.
    - The general accuracy ranking for the vibration frequency is thus LES, K-Epsilon (cubic), SSG-RSM and K-Omega SST.
- Other considerations:
    - The effect of replicating the test section exactly as well as modelling the vibrating rod with a full CSM structural model appears to yield low increase in accuracy, if any, compared to using a single inlet-outlet configuration and beam model respectively. The effect of the chosen turbulence model overshadows any possible impact of these model choices. Making this simplification eases mesh constraints, and can potentially speed up the calculations as remarked by the computational cost comparison.

- The above comment cannot yet be extended to VKI's rigid body modelling for the rod. The physics governing the motion changes, as in reality one would expect influence of a number of bending modes on the final rod shape while this strategy assumes the rod to be straight and moving about a joint/hinge. This point can be revisited once VKI runs a longer total simulation.
- While there is suspected to be an effect of the meshing strategy taken by the participants, the current comparison cannot shed light on the superiority of any approach. However, what can be observed from the medium resolution results is that the participants using a wall resolved approach in conjunction with eddy viscosity models were able to predict vibrations to a large extent as opposed to the participant who used a better SSG RSM model but in conjunction with a wall modelled mesh. This indicates that the wall treatment in combination with corresponding turbulence model plays an essential role for the prediction accuracy.
- The impact of the different material properties chosen by the participants also appears to be overshadowed. The vibration tests of the rod in air/vacuum and water are a good approach to validate chosen material properties.

5. Simulations performed by VKI

5.1 Problem definition

In the present study, the Free-Clamped configuration at Re = 21200 for the rod with a hemispherical tip is investigated. The curved geometry suppresses the generation of vortices and flow separation, so the resulting vibrations are expected to be predominantly turbulence-induced, a response typical for axial FIV. To simplify this configuration, the outlet pipes are excluded from the computational domain, as their distance from the rod tip renders their influence on the rod dynamics negligible. At the inlet, a fully developed turbulent velocity profile is prescribed, obtained from a precursor simulation and mapped onto the main domain. At the outlet boundary, the rod displacement is set to zero, consistent with the clamped end of the cantilever configuration. A schematic representation of the simplified problem is shown in Figure 36.

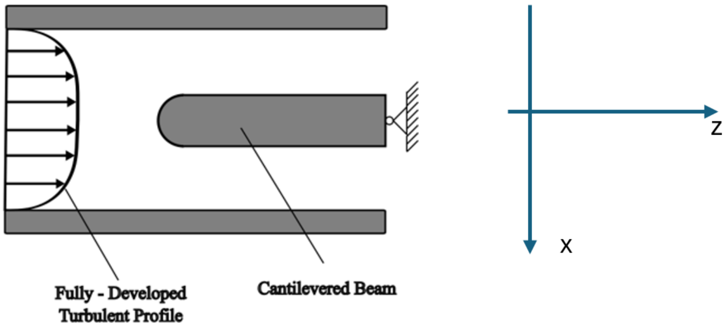

Figure 36. Schematic representation of the simplified problem

5.2 Geometry and mesh generation

The precursor simulation is a pipe with diameter 20.86mm and length 104.3mm. The mesh is conformal and made of 1.72M structured hexahedra cells with the open-source Gmsh software (Geuzaine & Remacle, 2009) as shown in Figure 37.

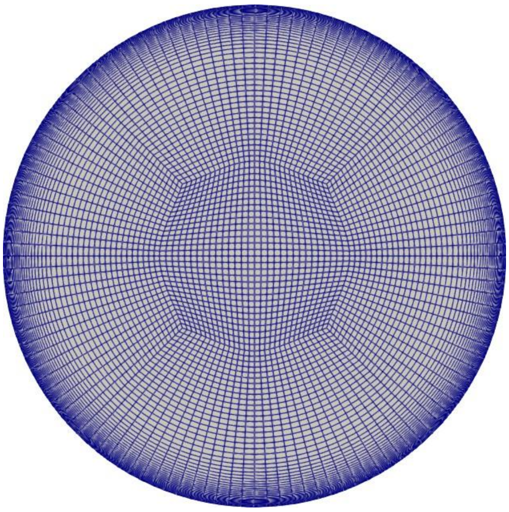

Figure 37: Cross section view of precursor pipe mesh

Funded by
the European Union

The main simulation comprises the confining pipe with a length of 1149.3mm, and the moving rod with diameter 10.01mm and length 1045mm with the rod tip located at z = 104.3mm. The mesh is conformal and made of 24.3M structured hexahedra cells with the OpenFOAM utility blockMesh. In Figure 38 and Figure 39 a cut view of the mesh around the rod is shown, as well as the surface mesh of the rod. The level of refinement at the walls has been analyzed beforehand, from a precursor URANS simulation, for wall-resolved LES. For both simulations, Figure 40 provides a histogram of the y+ values at solid walls.

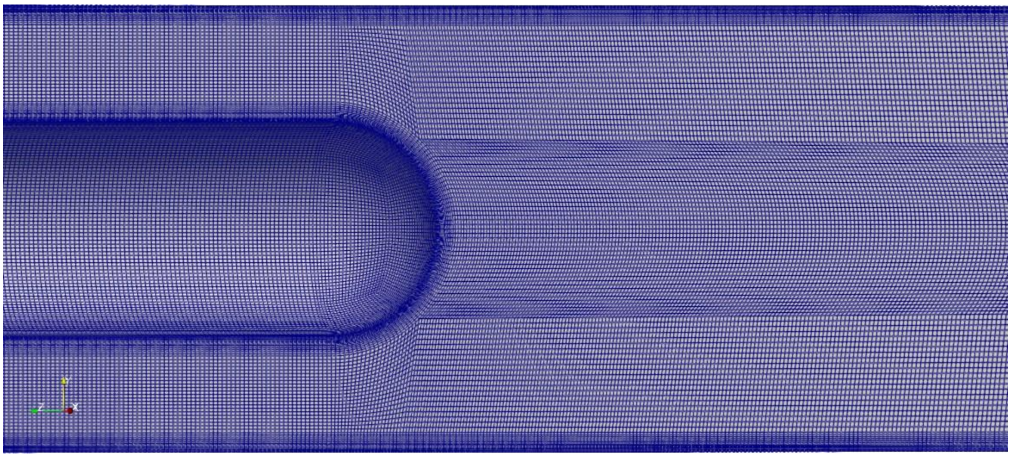

Figure 38: Cut view of the mesh around the rod tip

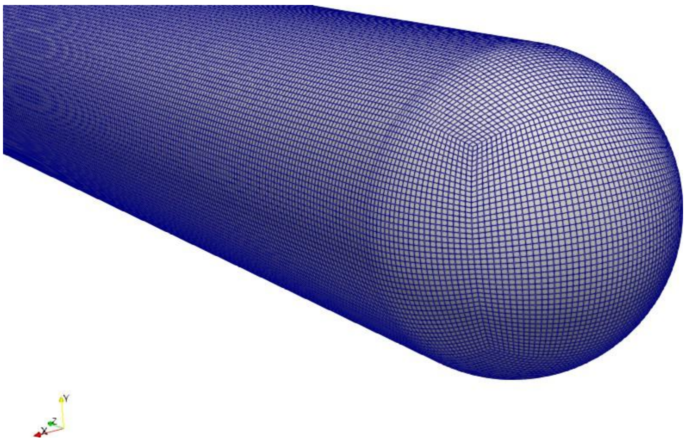

Figure 39: Surface mesh of rod tip

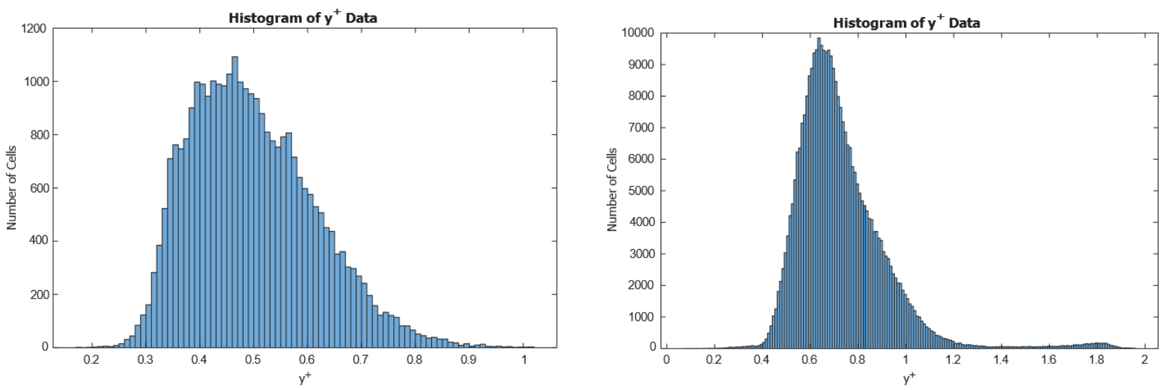

(a) Histogram of y^+ values at tube walls

(b) Histogram of y^+ values at rod surface

Figure 40: Distribution of y+ for both simulations

5.3 Physical modeling

The flow considered is incompressible and the working fluid is liquid water, with constant density, dynamic and kinematic viscosity values, respectively equal to ρ = 1000 kg m−3, μ = 10−3 Pa s and ν = 10−6 m2 s−1. Turbulence is modeled using wall-resolved Large Eddy Simulation (WR-LES) with the one-equation Yoshizawa subgrid-scale model (Yoshizawa, 1986). The above are specified in turbulenceProperties and transportProperties dictionaries respectively.

To account for the rod motion, several simplifying assumptions are introduced. The solid rod is modeled as a rigid body, with a spherical joint at the clamped end that prevents translation while allowing free rotation in all directions. An angular spring and damper are provided to represent the structural stiffness of the rod and to dissipate the initial transient response, respectively. Consequently, the rod motion is represented by a second-order model, capable of capturing only the first natural frequency of the continuous body. This assumption is justified by the slenderness of the rod, the small displacements observed experimentally, and the PSD of the measured response, which shows a dominant peak at the first natural frequency (Cioncolini, et al., 2018). Under these assumptions, the model is expected to reproduce the tip trajectory with reasonable accuracy.

The equation of motion governing the rod is derived from Newton's second law applied to the rigid body rotating about the clamped end:

$$I_{pivot}\ddot{\theta} + c_{\theta}\dot{\theta} + k_{\theta}\theta = M_{fluid}$$

I_{pivot} is the moment of inertia about the clamped end, c_ϑ is the damping coefficient and k_ϑ the stiffness of the spring. The moment of inertia about the pivot is given by the parallel axis theorem:

$$I_{pivot} = I_{CoM} + \frac{mL_1^2}{4}$$

where I_{CoM} is the moment of inertia about the center of mass and m is the mass of the rod. The hemispherical tip is ignored for the calculations of I_{CoM} as its influence is negligible.

The angular stiffness is derived from the lateral stiffness of a cantilever beam. If the rod rotates by an angle ϑ about the clamped end, the tip displaces by $\delta = L_1\vartheta$, and the equivalent lateral restoring force at the tip is:

$$F = \frac{3EI}{L_1^3}\delta$$

where E is Young's modulus and I is the second moment of area. The corresponding restoring moment about the clamped end is:

$$M = FL_1 = \frac{3EI}{L_1}\theta$$

The angular stiffness follows directly as:

$$k_{\theta} = 3\frac{EI}{L_1}$$

For the present rod, $E = 1.93 \times 10^{11} Pa$ and $I = 4.9 \times 10^{-10} m^4$. The damping coefficient is related to the damping ratio ζ by:

$$c_\theta = 2\zeta\sqrt{k_\theta I_{pivot}}$$

The damping ratio was estimated experimentally from the free vibration response of the cantilever with a flat end-piece and an imposed initial displacement (Li, et al., 2024), yielding $\zeta = 0.01 \pm 0.001$. The resulting natural frequency of the rigid-body model is $\omega_n = 5.56$ Hz.

Fluid-structure interaction in OpenFOAM is controlled through the dynamicMeshDict dictionary, located in the `constant` directory. This dictionary governs the mesh morphing solver, which updates the computational mesh in response to body motion and enforces the corresponding velocity boundary conditions on the fluid domain. Several mesh motion solvers are available in OpenFOAM, differing in how they handle mesh morphing and rigid body motion. In the present study, the sixDoFRigidBodyMotion solver is used, which solves the equations of motion for a general six-degree-of-freedom rigid body and supports the application of constraints to reduce the active degrees of freedom. The dynamicMeshDict dictionary defines the following: the mesh morphing parameters, the physical properties of the rigid body, the solver settings for the equations of motion, and the force and motion constraints applied to the body. In Listing 1, the first part of the dynamicMeshDict dictionary is shown where the mesh motion solver is declared.

```
dynamicFvMesh          dynamicMotion SolverFv Mesh ;

motion SolverLibs      ( "libsixDo FRigid Body Motion Dev .so"  );

solver                 sixDo FRigid Body Motion ;
```

Listing 1: Declaration of mesh motion solver

The mesh morphing behavior is controlled by two parameters defined in the sixDoFRigidBodyMotionCoeffs sub-dictionary: innerDistance and outerDistance. Mesh nodes within innerDistance of the body surface are displaced as a rigid body, following the motion exactly. Nodes between innerDistance and outerDistance are morphed, transitioning smoothly between the rigid motion zone and the fixed outer mesh. Nodes beyond outerDistance remain stationary. Note that outerDistance must always exceed innerDistance. The values specified in Listing 2 are chosen such that the inflation layers surrounding the rod remain within the rigid motion zone and are not subjected to morphing.

```
sixDo FRigid Body Motion Coeffs
{
    //Mesh Morphing Control
    innerDistance      0.001;
    outerDistance      0.004;
```

Listing 2: Mesh morphing controls

To solve the ODE describing the body motion, *Newmark* solver is selected with its default parameters.

```
    //6DoF  Solver  Control
    solver
    {
        type      Newmark ;
        gamma     0.5;    // Velocity  integration  coefficient
        beta      0.25;   // Position  integration  coefficient
    }
```

Listing 3: Solver for equations of motion

Funded by
the European Union

The mass properties of the rigid body are specified through three parameters. The mass parameter defines the total mass of the body, which can be found from the linear density of the rod. The centreOfMass specifies the position of the body centroid in the world coordinate system at the initial configuration. The momentOfInertia defines the diagonal components of the inertia tensor in the three principal axes (I_{xx}, I_{yy}, I_{zz}), expressed directly as moments of inertia rather than radii of gyration. The off-diagonal cross products of inertia are not required by the solver and are therefore omitted. Both centreOfMass and momentOfInertia are specified as three-component vectors. Furthermore, a velocity vector is defined that specifying the initial velocity of the body.

```
//Body Definition
mass            0.61446;
centreOfMass    ( 0 0 0.6268 );
momentOfInertia ( 0.0559 0.0559 7.69e-6 );
rho             rhoInf;
rhoInf          1000;
velocity        ( 0 0 0 );
```

Listing 4: Body definition

The forces acting on the rigid body are specified in Listing 5. The patch entry defines the mesh patches representing the rigid body surface, from which *OpenFOAM* automatically integrates the pressure and viscous stresses to compute the total hydrodynamic load. Additional restraint forces, other than the fluid forces, are defined in the restraints sub-dictionary. In the present study, the linearAxialAngularSpring model is used, which applies to a restoring moment about a single fixed axis in opposition to the body rotation. This model is governed by the following parameters: axis, which defines the axis of rotation; stiffness, the angular spring stiffness; damping, the angular damping coefficient; and referenceOrientation, which specifies the reference orientation at which the restraint forces are zero.

```
//Force Definitions
patches ( rod );
restraints
{
    xAxis_spring
    {
        sixDoFRigidBodyMotionRestraint  linearAxialAngularSpring;
        axis                            ( 1 0 0 );
        stiffness                       273.066;
        damping                         0.228;
        referenceOrientation            ( 1 0 0 0 1 0 0 0 1 );
    }

    yAxis_spring
    {
        sixDoFRigidBodyMotionRestraint  linearAxialAngularSpring;
        axis                            ( 0 1 0 );
        stiffness                       273.066;
        damping                         0.234;
        referenceOrientation            ( 1 0 0 0 1 0 0 0 1 );
    }
}
```

Listing 5: Force definitions

The final section of the dynamicMeshDict, shown in Listing 6, defines the motion constraints applied to the rod. Unlike restraints, which apply reactive forces, constraints directly restrict the degrees of freedom of the body without generating any force. In the present simulation, a single pointConstraint is applied, which eliminates all translational motion while allowing unconstrained rotation in any direction about a defined centre of rotation. This centre of rotation is specified through the centreOfRotation keyword and must not coincide with the centre of mass of the body. This configuration is equivalent to a spherical joint, consistent with the rigid body model described above.

```
//Motion Definitions
constraints
{
    pointConstraint
    {
        sixDofRigidBodyMotionConstraint  point;
        centreOfRotation                 ( 0 0 1.1493 );
    }
}
```

Listing 6: Motion definitions

5.4 Coupling methodology

The coupling is performed with the open-source software preCICE, designed for general partitioned multi-physics and multi-scale simulations, including fluid-structure interaction, conjugate heat transfer and fluid-fluid coupling (Chourdakis, 2022). Rather than implementing a monolithic solver, preCICE coordinates existing solvers, each responsible for a subpart of the overall simulation. It provides a range of coupling methods, data mapping schemes, and inter-process communication methods, making it applicable to a wide variety of multi-physics configurations. The connection to OpenFOAM is established through a dedicated preCICE adapter, which integrates into the solver as a function object (Chourdakis, et al., 2023), requiring no modification of the OpenFOAM source code.

The case is configured through the precice-config.xml file, which specifies the participating solvers, the fields exchanged between them, the numerical methods used for data mapping and the coupling schemes. As discussed in Section 3.2, the precursor simulation is connected in series with the main domain to generate fully developed turbulent inlet conditions. At each timestep, the resulting velocity and turbulent kinetic energy fields are extracted from the precursor outlet and mapped onto the inlet of the main domain, ensuring a continuous, unsteady turbulent inflow throughout the simulation (one-way coupling).

```
<data:vector name="Velocity" />
<data:scalar name="TKE" />

<mesh name="Fluid1-Mesh" dimensions="3">
  <use-data name="Velocity" />
  <use-data name="TKE" />
</mesh>

<mesh name="Fluid2-Mesh" dimensions="3">
  <use-data name="Velocity" />
  <use-data name="TKE" />
</mesh>
```

Listing 7: Configuration file: Coupling data and meshes

The preCICE configuration file is structured into several sections. The first section defines the exchanged data, and the interface coupling meshes. As shown in Listing 7, two meshes are defined to exchange velocity and turbulent kinetic energy data. The dimensions parameter specifies the spatial dimension of each mesh, set to 3 for the present three-dimensional configuration. By default, the preCICE adapter does not support the transfer of turbulent kinetic energy between coupled simulations. To enable this, the adapter source code was extended accordingly.

In general, when coupling two participants at a common interface, and the two surface meshes do not match, a mapping method must be defined to transfer data between them. As shown in Listing 8, each data mapping definition refers to two meshes: a provider mesh, defined by the sending participant, and a receiver mesh, defined by the receiving participant. In the present configuration Fluid1-Mesh corresponds to the precursor domain and Fluid2-Mesh to the main domain. The direction entry specifies how these meshes are assigned to the *from* and *to* slots, indicating on which mesh data is written and on which it is read. Here, the precursor domain writes the velocity and turbulent kinetic energy fields to the main domain mesh after each time step, while the main domain reads these fields before proceeding with its computations.

```
<participant name="Fluid1">
  <provide-mesh name="Fluid1-Mesh" />
  <receive-mesh name="Fluid2-Mesh" from="Fluid2" />
  <write-data name="Velocity" mesh="Fluid1-Mesh" />
  <write-data name="TKE" mesh="Fluid1-Mesh" />
  <mapping:nearest-neighbor
    direction="write"
    from="Fluid1-Mesh"
    to="Fluid2-Mesh"
    constraint="conservative"/>
</participant>

<participant name="Fluid2">
  <provide-mesh name="Fluid2-Mesh" />
  <receive-mesh name="Fluid1-Mesh" from="Fluid1" />
  <read-data name="Velocity" mesh="Fluid2-Mesh" />
  <read-data name="TKE" mesh="Fluid2-Mesh" />
  <export:vtu every-n-time-windows="-1" directory="Debug" every-iteration="0"/>
  <mapping:nearest-neighbor
    direction="read"
    from="Fluid1-Mesh"
    to="Fluid2-Mesh"
    constraint="consistent" />
</participant>
```

Listing 8: Configuration file: Mapping configuration

The mapping method used is nearest-neighbour, a first-order method, that assigns to each target mesh vertex the value of the nearest source mesh vertex. While computationally efficient, this method introduces errors on non-matching meshes and is therefore more suitable when the meshes are sufficiently similar in resolution. Finally, since the simulations are executed in parallel, preCICE restricts the available constraint types to read-consistent and write-conservative. The consistent constraint is suitable for intensive quantities, such as temperature, and ensures that each target vertex receives the value of its nearest source vertex, preserving pointwise field values across the interface. The conservative constraint, by contrast, is suitable for extensive quantities, such as mass, and ensures that the global sum of the transferred quantity is preserved between the source and target meshes. In the present case, the mesh resolution of the precursor outlet patch is almost the same as the mesh resolution of the main domain inlet patch. Thus, the mapping should not distort the transferred fields regardless of the type of mapping constraint.

The coupling scheme is configured as parallel-explicit: both participants execute simultaneously at each timestep and exchange data once per time step without iterative sub-cycling. This is appropriate for the present one-way coupling, where no iterative convergence between the two domains is required. The coupling timestep is set equal to the solver timestep, ensuring that data is exchanged at every computational step. The total simulation time is controlled through the max-time entry.

```
<coupling-scheme:parallel-explicit>
  <time-window-size value="0.00003" />
  <max-time value="2.4"/>

  <participants first="Fluid1" second="Fluid2" />
  <exchange data="Velocity"
    mesh="Fluid1-Mesh"
    from="Fluid1"
    to="Fluid2"
    initialize="yes"/>
  <exchange data="TKE"
    mesh="Fluid1-Mesh"
    from="Fluid1"
    to="Fluid2"
    initialize="yes"/>
</coupling-scheme:parallel-explicit>
```

Listing 9: Configuration file: Coupling scheme configuration

5.5 Boundary conditions and numerics

As described in Section 5.3, turbulence is modeled using wall-resolved LES with the one-equation Yoshizawa subgrid-scale model. Accordingly, boundary conditions are prescribed for the velocity, pressure, turbulent viscosity, and turbulent kinetic energy fields in both simulations.

The precursor simulation consists of a periodic pipe, in which the inlet and outlet patches are coupled using the cyclic boundary condition in OpenFOAM, which links a pair of conformal patches such that flow leaving one patch immediately enters the other. Accordingly, the inlet and outlet boundary conditions for all fields in the precursor simulation are of type cyclic. The remaining boundary is the pipe wall. For the velocity field, the noSlip condition is applied, enforcing zero velocity at the wall. For pressure and turbulent viscosity, a zeroGradient condition is applied. For the turbulent kinetic energy, a fixedValue condition is applied with a value of zero, consistent with the assumption of no turbulent fluctuations at the wall. The above are listed in Table 16. The flow was forced to a mean velocity of 1.503m/s.

Table 16: Boundary conditions for precursor simulation.

Boundary	Velocity	Pressure	Turbulent Kinetic Energy	Turbulent Viscosity
Inlet	cyclic	cyclic	cyclic	cyclic
Outlet	cyclic	cyclic	cyclic	cyclic
Walls	noSlip	zeroGradient	fixedValue	zeroGradient

Funded by the European Union

The main domain comprises four boundary patches: the inlet, outlet, tube wall, and rod surface. Since the mesh morphs according to the rigid body motion, OpenFOAM requires boundary conditions for the pointDisplacement field, which describes the displacement of the rigid body. The rod surface patch is assigned to a calculated condition, specifying that its displacement is computed internally by the motion solver. All remaining patches are assigned a fixedValue condition of zero, enforcing no mesh displacement. For the velocity field, a movingWallVelocity condition is applied to the rod surface, enforcing the local body velocity on the fluid domain. At the inlet, the velocity and turbulent kinetic energy fields are prescribed through the preCICE coupling, as described in Section 5.4, superseding any default boundary condition. For turbulent viscosity, a zeroGradient condition is applied at the outlet and tube wall, while a calculated condition is applied at the inlet. For pressure, a zeroGradient condition is applied everywhere except the outlet patch where a fixedValue condition of value zero is defined. The boundary conditions of the main domain are displayed in Table 17.

Table 17: Boundary conditions for main simulation.

Boundary	Velocity	Pressure	Turbulent Kinetic Energy	Turbulent Viscosity	Displacement
Inlet	-	zeroGradient	-	calculated	fixedValue
Outlet	zeroGradient	fixedValue	zeroGradient	zeroGradient	fixedValue
Tube	noSlip	zeroGradient	fixedValue	zeroGradient	fixedValue
Rod	movingWallVelocity	zeroGradient	fixedValue	zeroGradient	calculated

For the periodic pipe, a momentum source term must be added to the Navier-Stokes equations to drive the flow and establish the desired mass flow rate. In OpenFOAM, this is implemented through the fvOptions dictionary, as shown in Listing 10. The patchMeanVelocityForce option applies to a momentum source term that adjusts dynamically until the mean velocity at the specified patch matches the target value Ubar. The mass flow rate corresponds to a Re = 21200 in the annular domain.

```
momentumSource
{
    type            patchMeanVelocityForce;
    patch           inlet;
    selectionMode   all;
    fields          (U);
    Ubar            (0 0 1.503);
}
```

Listing 10: Declaration of mesh motion solver

Both simulations are advanced in time using the second-order implicit backward differencing scheme. The convective and diffusive terms are discretised using a second-order Gauss linear scheme, with cell-limited gradient reconstruction. Laplacian terms are discretised using a Gauss linear scheme with corrected non-orthogonal correction in the precursor simulation.

In the main domain, where mesh motion introduces non-orthogonality, a limited non-orthogonal correction with a limiter value of 1 is applied instead, together with a consistent limited surface normal gradient scheme, providing greater robustness under mesh deformation. Interpolation from cell centres to face centres uses a standard linear scheme in both simulations. The pressure-velocity coupling is handled by the PIMPLE algorithm in both simulations. For the precursor simulation, a single outer corrector step with two momentum corrector steps is applied per timestep, with the momentum predictor enabled. The main simulation requires two outer corrector steps and three momentum corrector steps per timestep to account for the additional accelerations introduced into the fluid domain by the rigid body mesh motion. The timestep for both simulations is 2 × 10−5sec and ensures the CFL to be bellow one.

5.6 Results

5.6.1 Precursor simulation

The mean velocity and Reynolds stress radial profiles obtained from the fully developed precursor LES are shown in Figure 41 and Figure 42, respectively. In Figure 41a, the streamwise velocity profile is compared against the experimental data of (Zagarola, 1996), showing reasonable agreement with small discrepancies that remain within acceptable limits. Furthermore, the shape factor H of the LES profile is 1.5, consistent with the expected value for fully developed turbulent pipe flow, confirming that the precursor simulation generates inlet conditions representative of the target flow regime. Also, the mean radial velocity profile, Figure 41b, is almost zero in the simulation, which indicates that the averages are well converged. In conclusion, the precursor simulation strategy managed to produce turbulent conditions for the wall-resolved LES of the main domain.

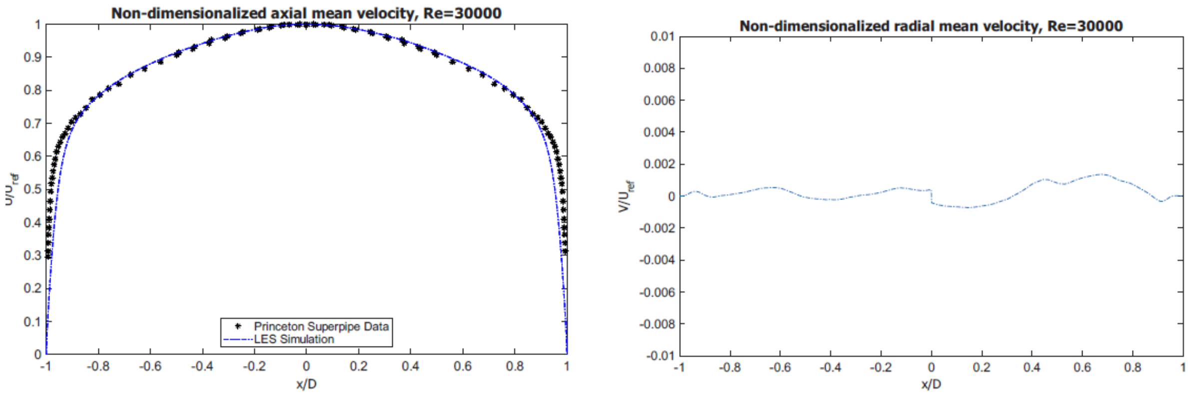

(a) Non-dimensionalized axial mean velocity (b) Non-dimensionalized radial mean velocity

Figure 41: Non-dimensionilized mean velocity horizontal profiles

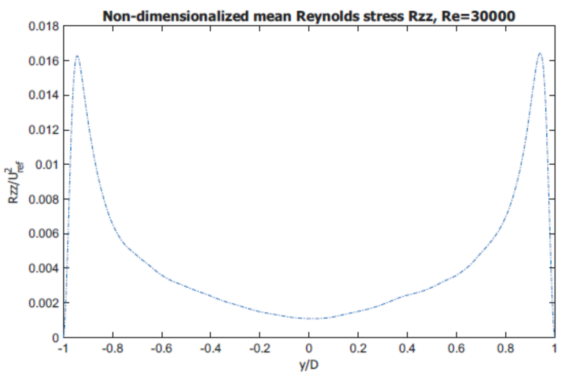

(a) Non-dimensionalized mean Reynolds stress R_{zz}

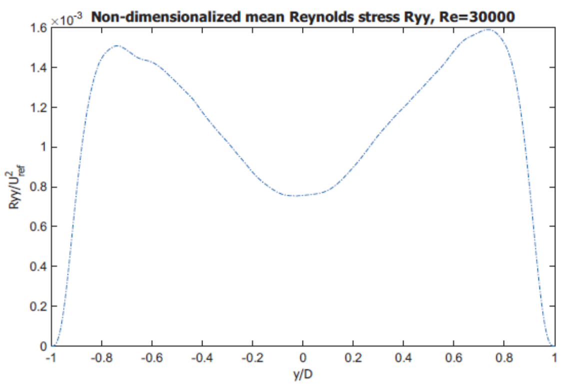

(b) Non-dimensionalized mean Reynolds stress R_{yy}

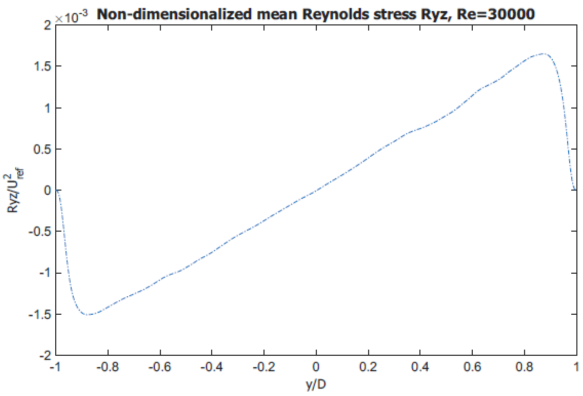

(c) Non-dimensionalized mean Reynolds stress R_{yz}

Figure 42: Non-dimensionilized mean Reynolds stress radial profiles

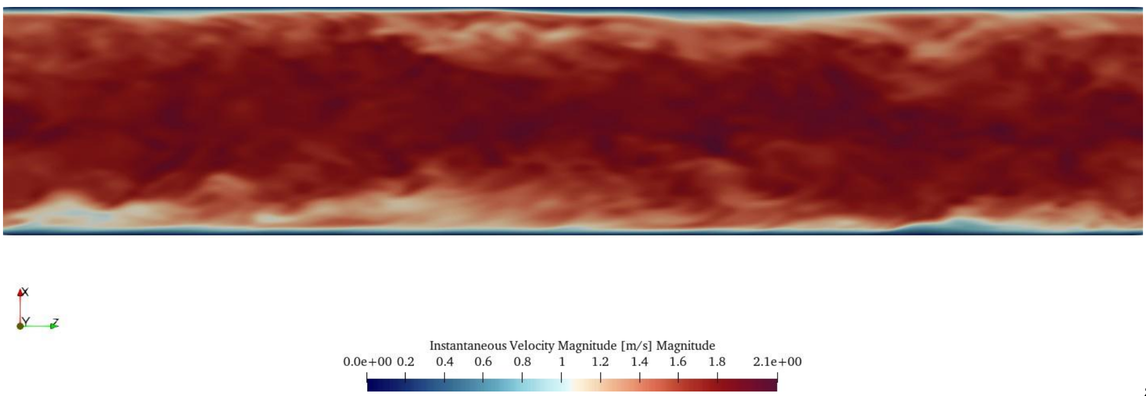

In , a cut view of the instantaneous velocity field is provided, while Figure 44, Figure 45 and Figure 46 depict cut views of the Reynolds stresses fields. In Figure 47, it is shown that the fraction of resolved turbulent kinetic energy is around 80%, indicating a good mesh resolution for the precursor simulation.

Funded by the European Union

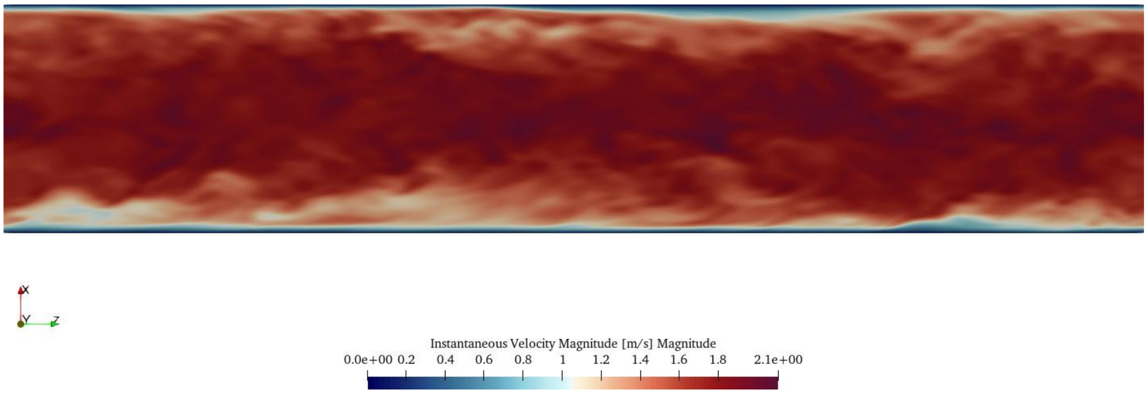

Figure 43: Instantaneous velocity field [m/s]

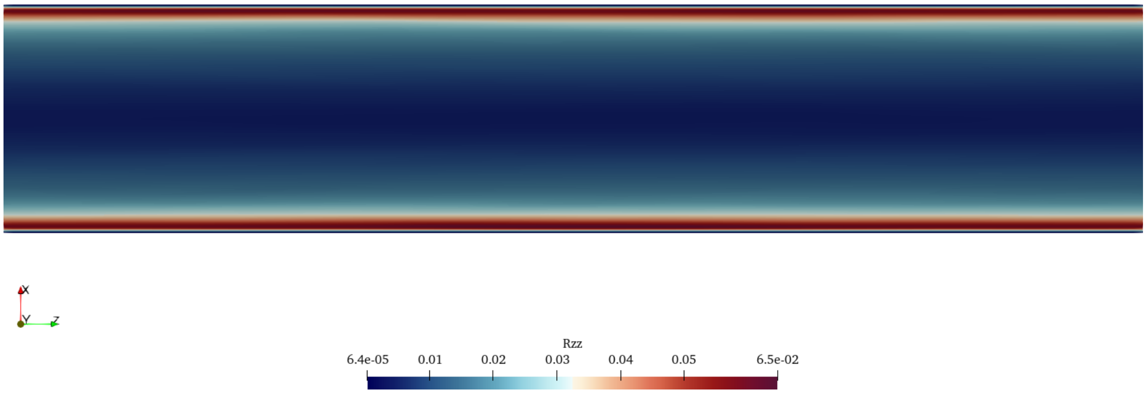

Figure 44: Reynolds stress Rzz [m2/s2]

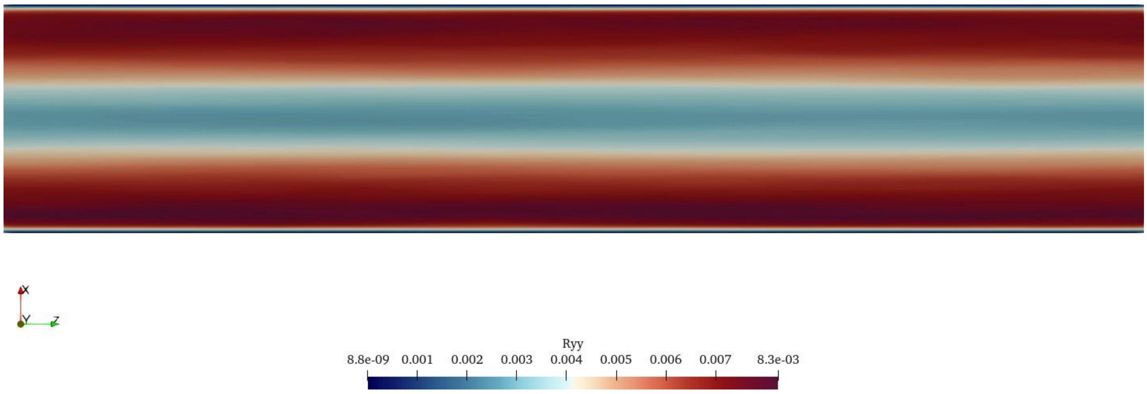

Figure 45: Reynolds stress Ryy [m2/s2]

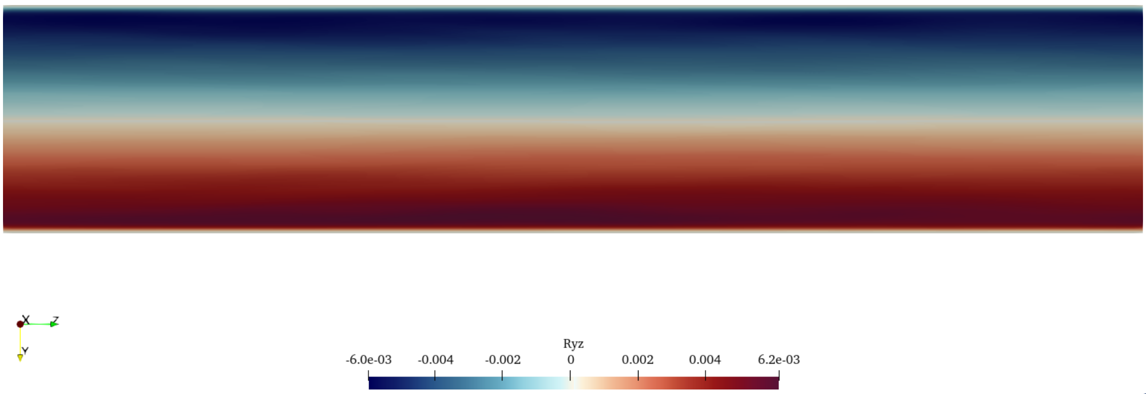

Figure 46: Reynolds stress Ryz [m2/s2]

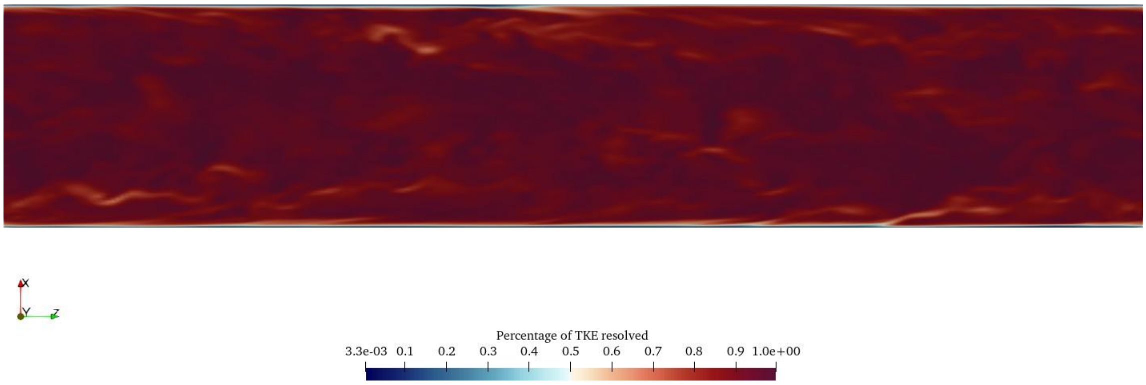

Figure 47: Fraction of resolved TKE

5.6.2 Main domain simulation

The main domain simulation was run for a total averaging time of 0.6 s. The results are compared against experimental PIV measurements at six axial planes, shown schematically in Figure 48, where the parameter z denotes the distance from the rod tip.

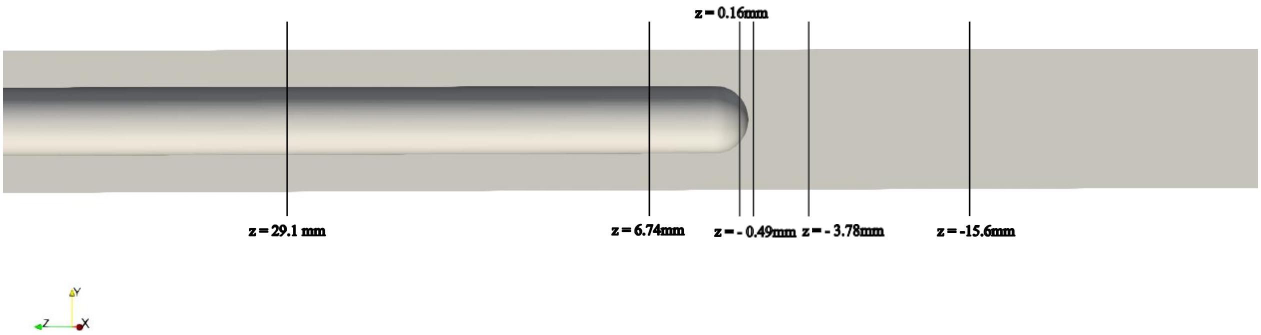

Figure 48: Planes for measurements

The mean streamwise and radial velocity profiles at each plane are shown in Figure 49-Figure 57. The streamwise velocity profiles show promising agreement with the Particle Image Velocimetry (PIV) measurements across most planes. However, the radial velocity profiles at the planes closest to the rod tip (Figure 49 and Figure 51) deviate from the expected symmetric distribution, exhibiting non-zero values and irregular streamwise profiles, indicating that the averaging time is not yet sufficient for full statistical convergence in this region.

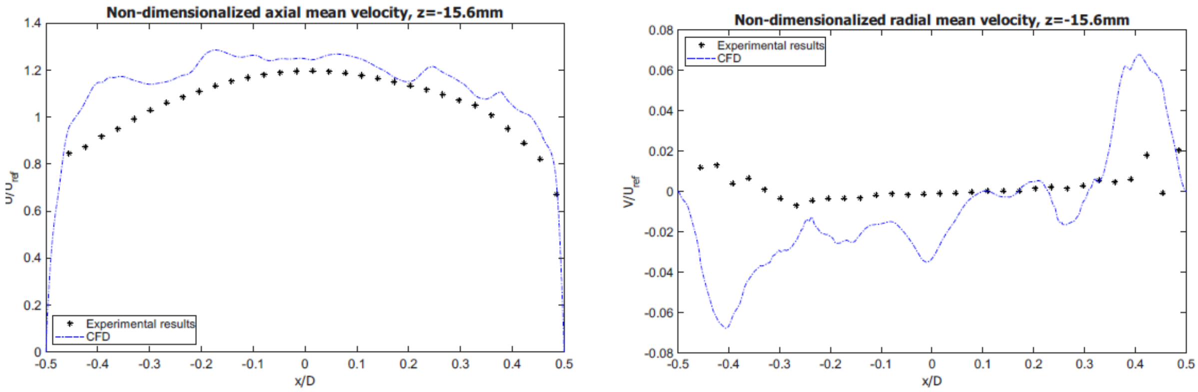

(a) Non-dimensionalized axial mean velocity (b) Non-dimensionalized radial mean velocity

Figure 49:Comparison of non-dimensionilized mean velocity horizontal profiles, z = −15.6mm

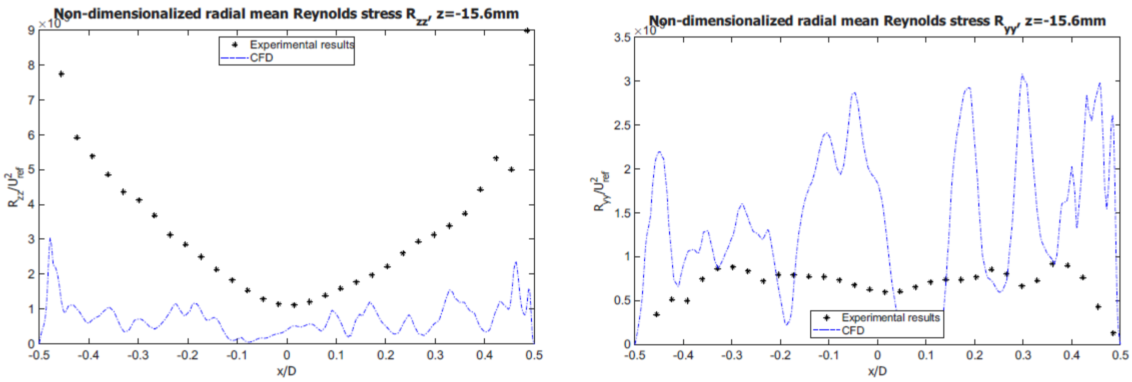

(a) Non-dimensionalized mean Reynolds stress R_{zz} (b) Non-dimensionalized mean Reynolds stress R_{yy}

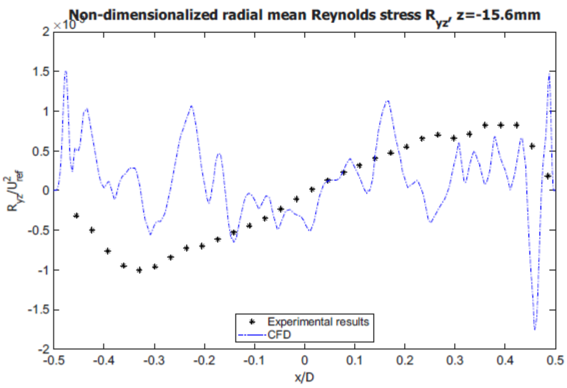

(c) Non-dimensionalized mean Reynolds stress R_{yz}

Figure 50: Comparison of non-dimensionalized mean Reynolds stresses horizontal profiles, z = −15.6mm

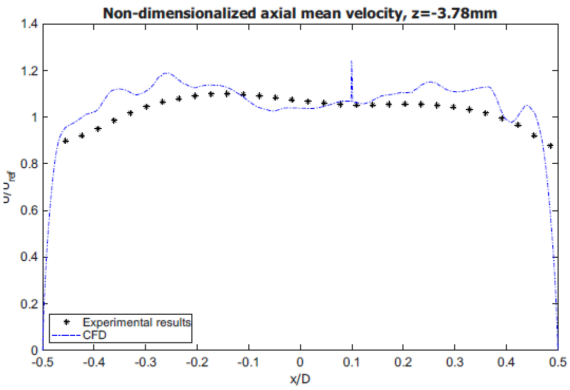

(a) Non-dimensionalized axial mean velocity

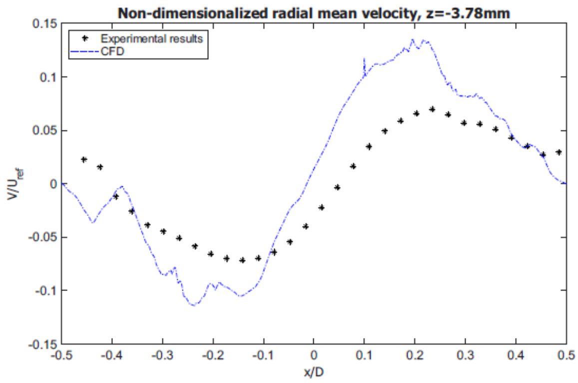

(b) Non-dimensionalized radial mean velocity

Figure 51:Comparison of non-dimensionalized mean velocity horizontal profiles, z = −3.78mm

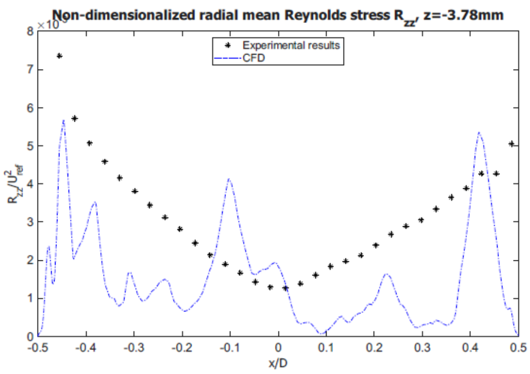

(a) Non-dimensionalized mean Reynolds stress R_{zz}

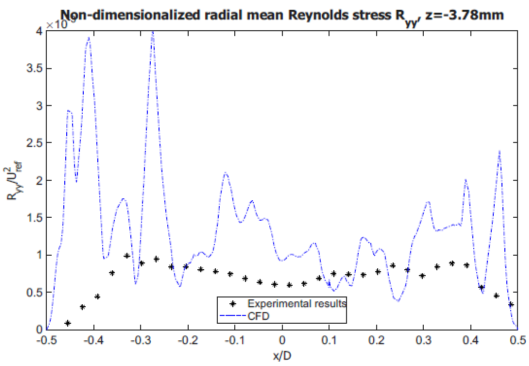

(b) Non-dimensionalized mean Reynolds stress R_{yy}

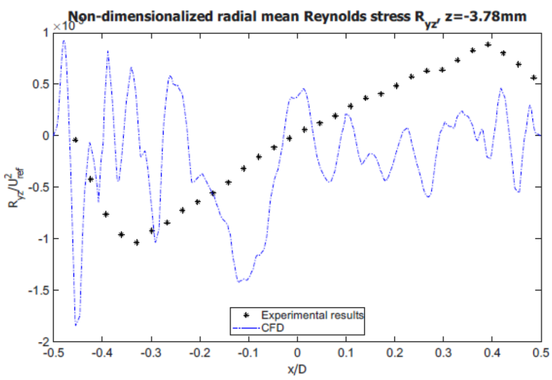

(c) Non-dimensionalized mean Reynolds stress R_{yz}

Figure 52: Comparison of non-dimensionalized mean Reynolds stresses horizontal profiles, z = −3.78mm

Downstream of the rod tip (Figure 53–Figure 57), the expected flow separation and subsequent profile recovery are clearly captured. The Reynolds stress profiles at each plane are shown in Figure 50–Figure 58. As with the velocity field, the profiles reflect the preliminary nature of the averaging, with the characteristic profile shapes not yet fully resolved in most planes.

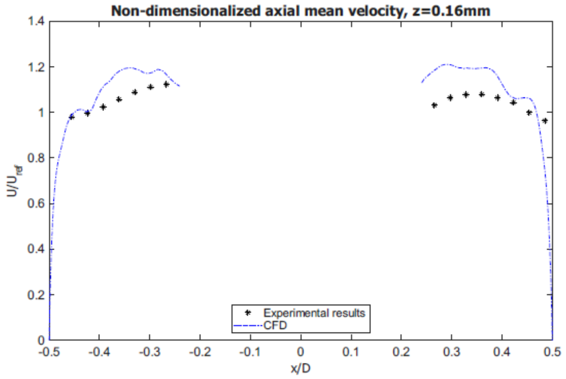

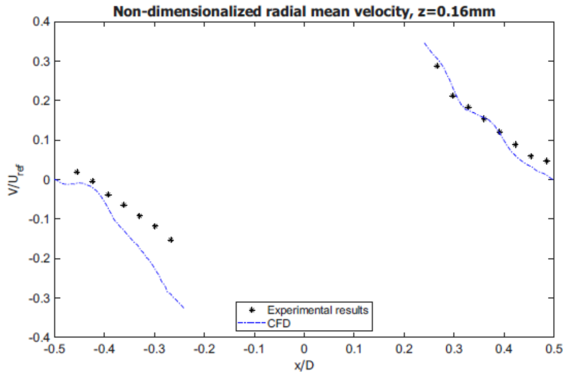

(a) Non-dimensionalized axial mean velocity (b) Non-dimensionalized radial mean velocity

Figure 53: Comparison of non-dimensionalized mean velocity horizontal profiles, z = 0.16mm

Nevertheless, the radial Reynolds stress profiles at the downstream planes (Figure 54-Figure 58) already show reasonable agreement with the PIV data, suggesting that the simulation is converging toward the correct solution. Vertical profiles of the mean velocity and Reynolds stresses at three radial locations are provided in Figure 59-Figure 61.

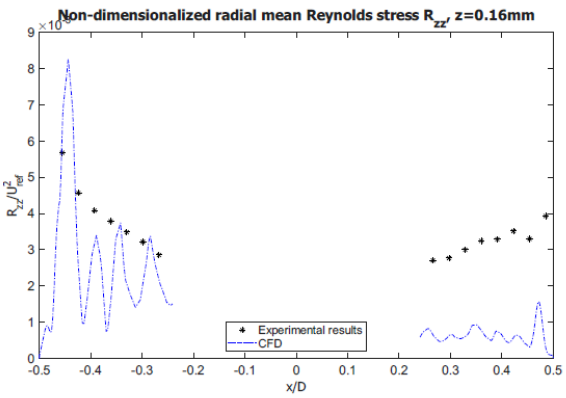

(a) Non-dimensionalized mean Reynolds stress R_{zz}

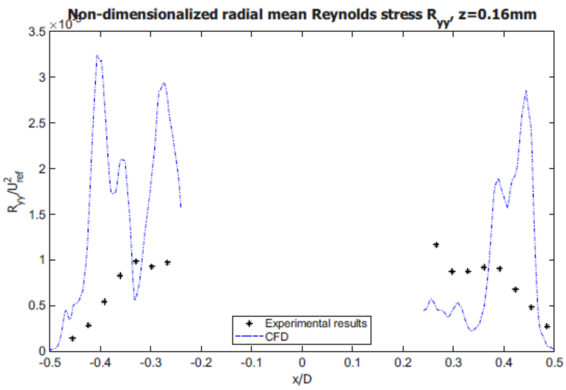

(b) Non-dimensionalized mean Reynolds stress R_{yy}

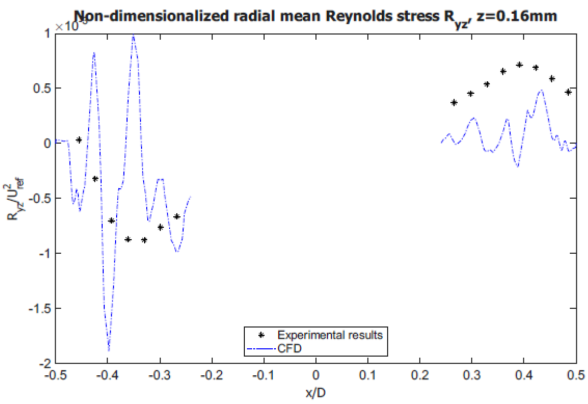

(c) Non-dimensionalized mean Reynolds stress R_{yz}

Figure 54: Comparison of non-dimensionalized mean Reynolds stresses horizontal profiles, z = 0.16mm

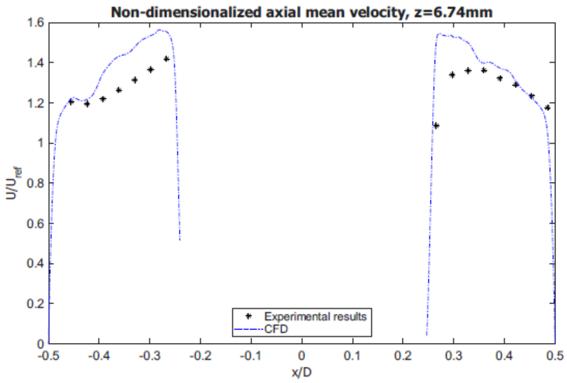

(a) Non-dimensionalized axial mean velocity

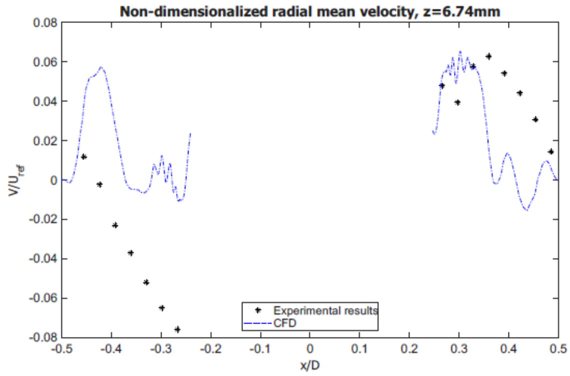

(b) Non-dimensionalized radial mean velocity

Figure 55: Comparison of non-dimensionalized mean velocity horizontal profiles, z = 6.74mm

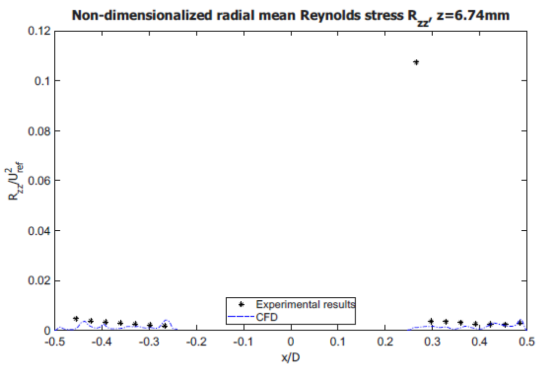

(a) Non-dimensionalized mean Reynolds stress R_{zz}

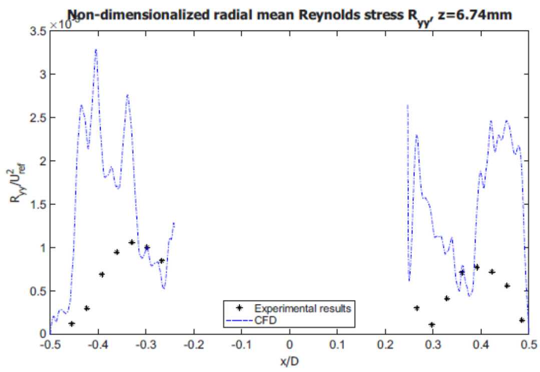

(b) Non-dimensionalized mean Reynolds stress R_{yy}

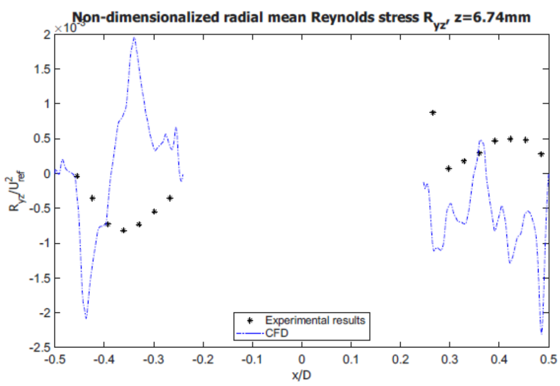

(c) Non-dimensionalized mean Reynolds stress R_{yz}

Figure 56: Comparison of non-dimensionalized mean Reynolds stresses horizontal profiles, z = 6.74mm

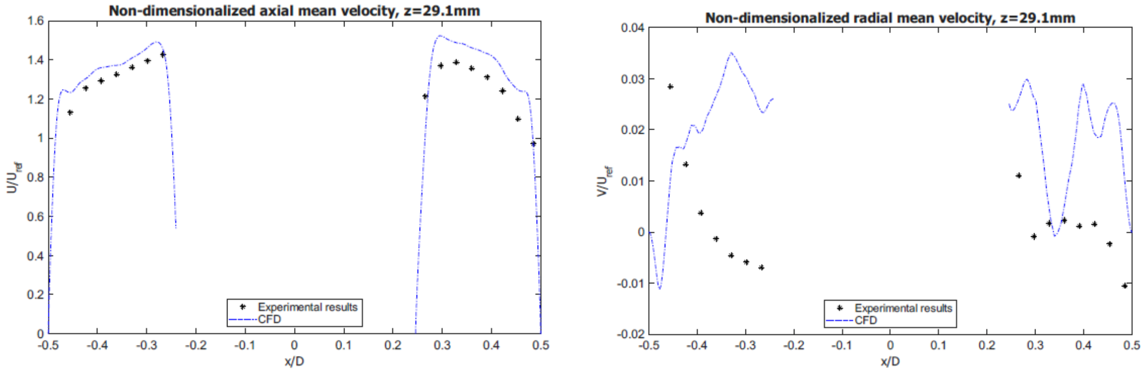

(a) Non-dimensionalized axial mean velocity (b) Non-dimensionalized radial mean velocity

Figure 57: Comparison of non-dimensionalized mean velocity horizontal profiles, z = 29.1mm

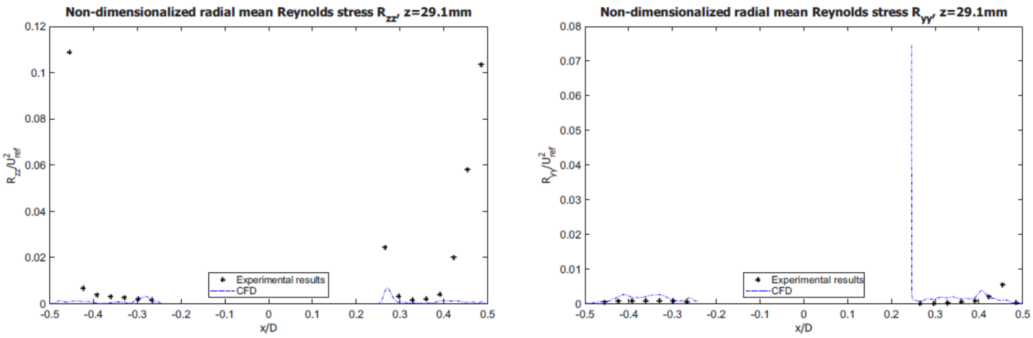

(a) Non-dimensionalized mean Reynolds stress R_{zz} (b) Non-dimensionalized mean Reynolds stress R_{yy}

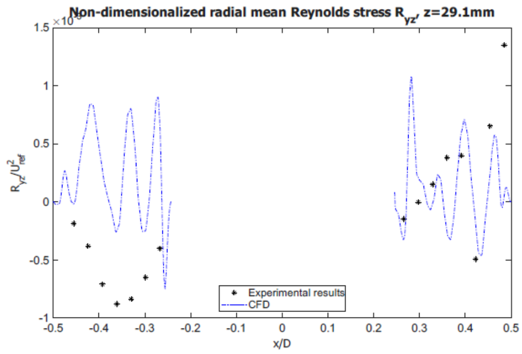

(c) Non-dimensionalized mean Reynolds stress R_{yz}

Figure 58: Comparison of non-dimensionalized mean Reynolds stresses horizontal profiles, z = 29.1mm

Funded by the European Union

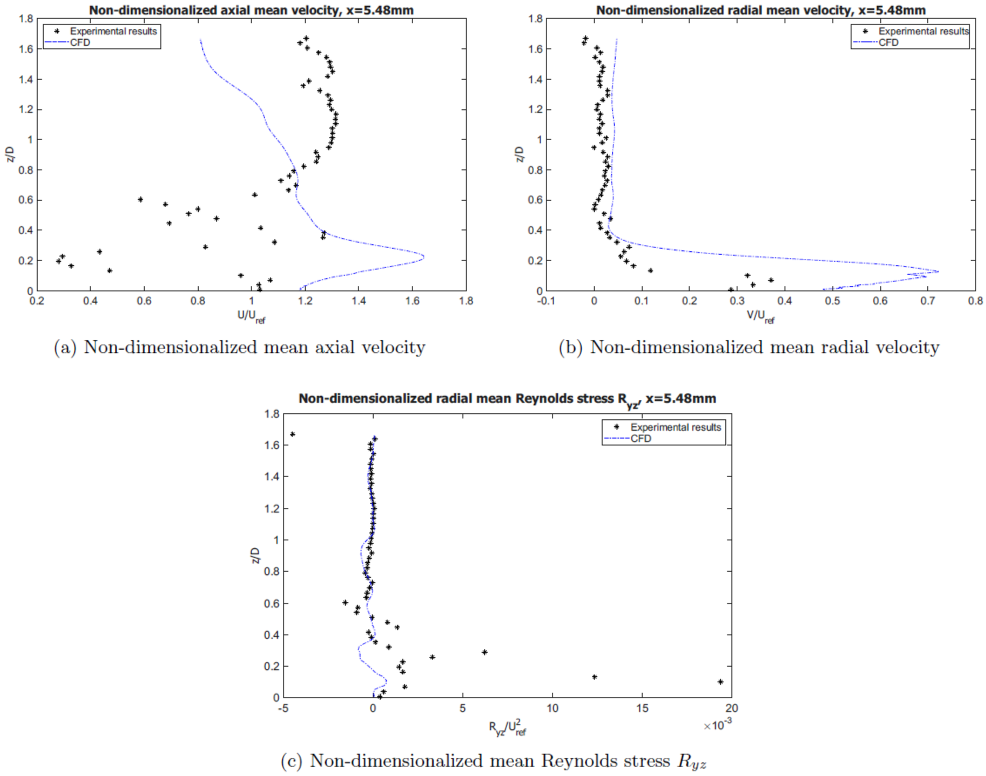

(a) Non-dimensionalized mean axial velocity

(b) Non-dimensionalized mean radial velocity

(c) Non-dimensionalized mean Reynolds stress R_{yz}

Figure 59: Non-dimensionalized mean vertical profiles, x = 5.48mm

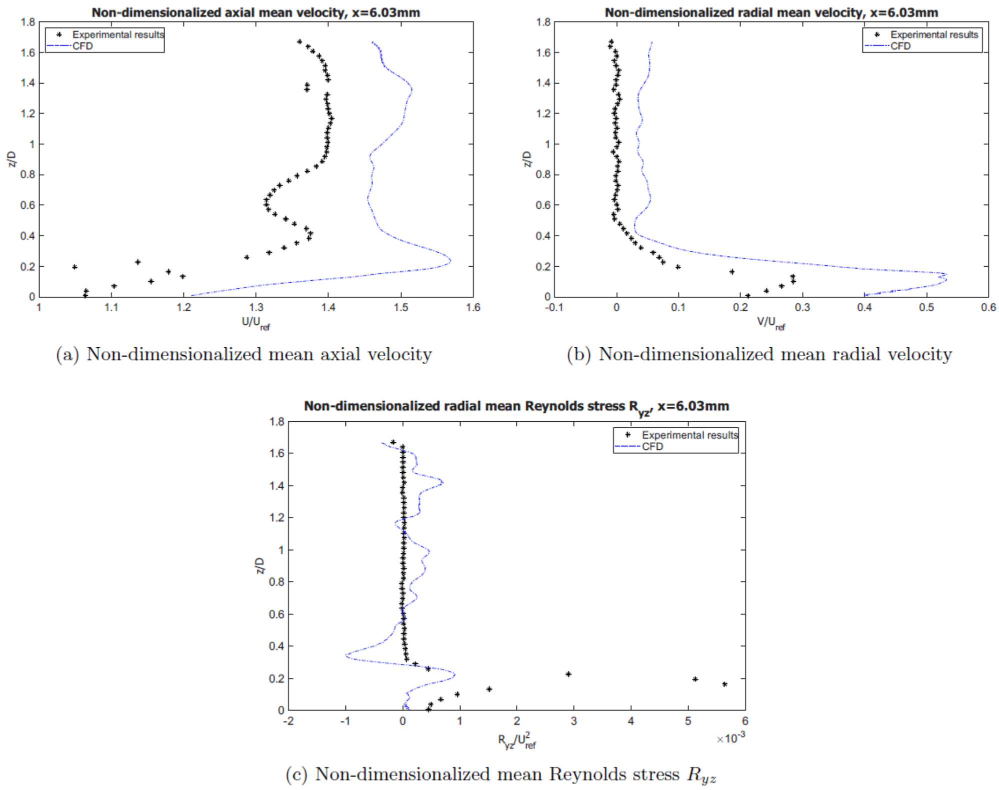

(a) Non-dimensionalized mean axial velocity

(b) Non-dimensionalized mean radial velocity

(c) Non-dimensionalized mean Reynolds stress R_{yz}

Figure 60: Non- dimensionalized mean vertical profiles, x = 6.03mm

Funded by the European Union

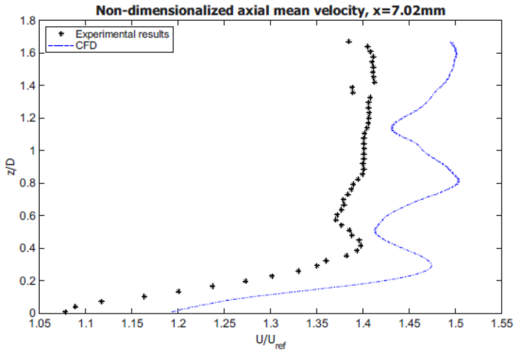

(a) Non-dimensionalized mean axial velocity

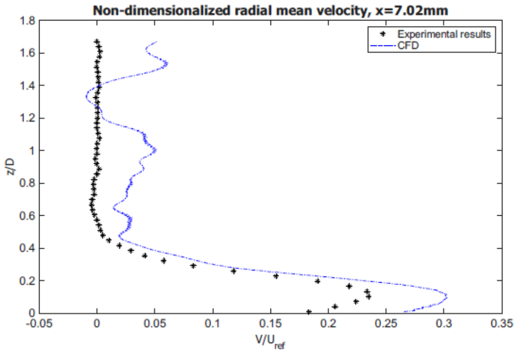

(b) Non-dimensionalized mean radial velocity

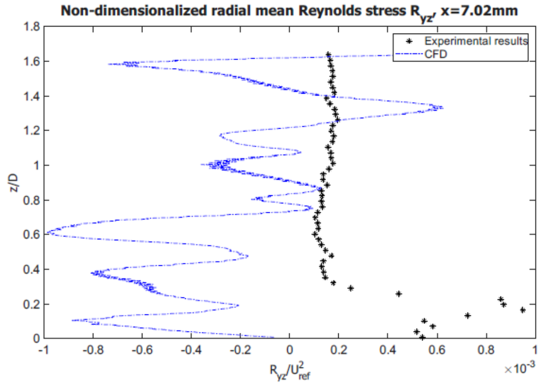

(c) Non-dimensionalized mean Reynolds stress R_{yz}

Figure 61: Non- dimensionalized mean vertical profiles, x = 7.02mm

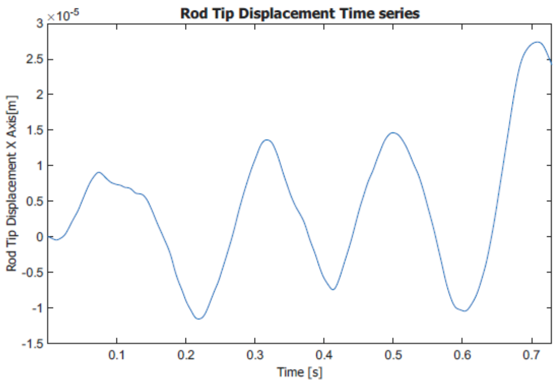

(a) Time series of rod movement - x axis.

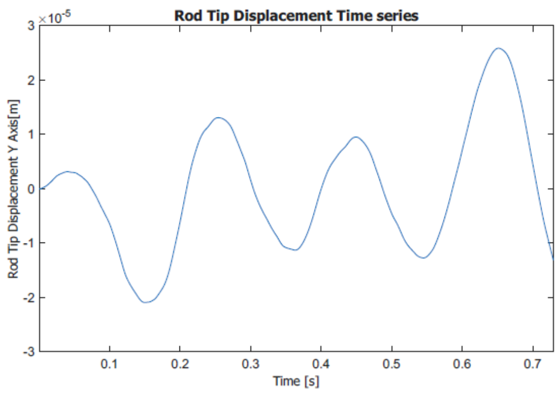

(b) Time series of rod movement - y axis.

Figure 62: Time series of rod movement

The rod displacement history is shown in Figure 62. Contour plots of the instantaneous velocity, time-averaged velocity, and mean pressure fields are presented in Figure 63, Figure 64 and Figure 65, respectively. The pressure contours clearly reveal the stagnation region upstream of the rod tip and the pressure recovery downstream, consistent with the expected flow behaviour around a bluff body.

Funded by the European Union

Overall, while the results are preliminary and additional averaging time is required for full statistical convergence, the simulation already captures the key flow features and shows promising agreement with the experimental data, particularly for the streamwise velocity and downstream Reynolds stress profile.

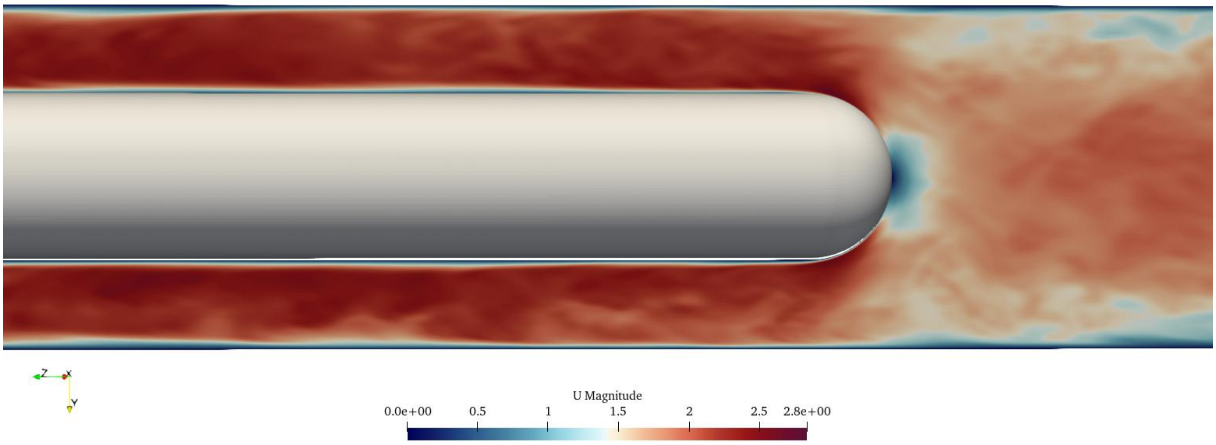

Figure 63: Instantaneous velocity field [m/s]

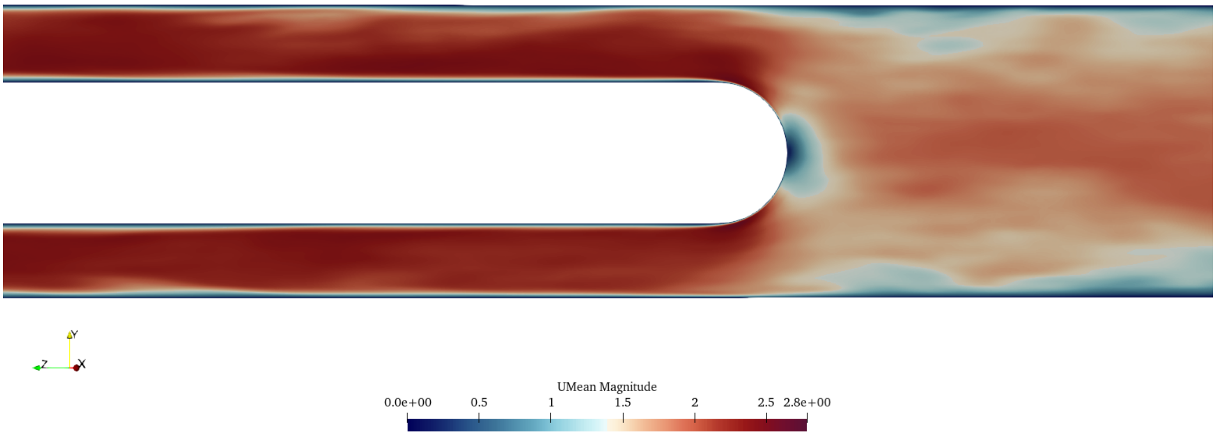

Figure 64: Mean velocity field [m/s]

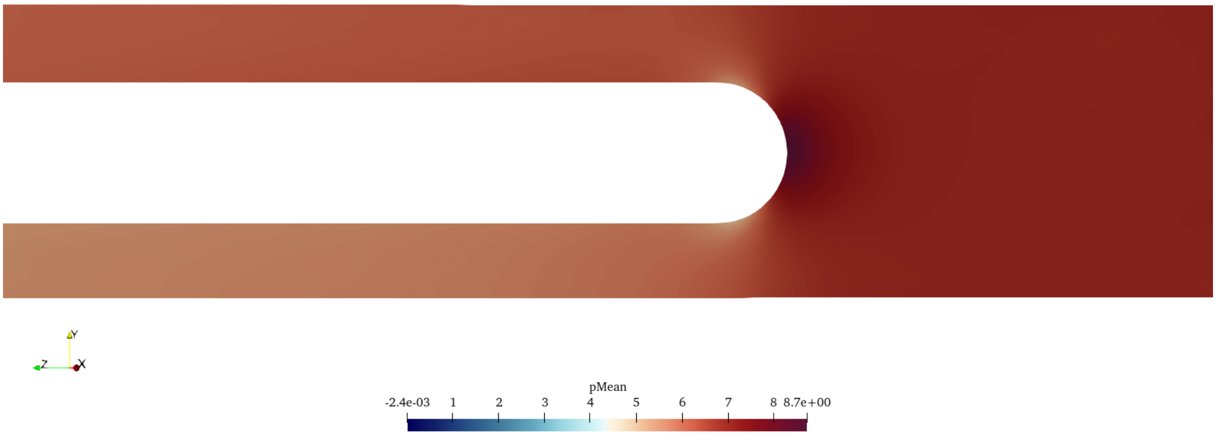

Figure 65: Mean pressure

5.7 Conclusions

This chapter described the numerical model developed by VKI, focusing on the Free-Clamped configuration at $Re = 21200$ with a hemispherical rod tip. The computational framework is based on OpenFOAM and uses wall-resolved Large Eddy Simulation, a rigid-body representation of the rod motion, dynamic mesh morphing, and one-way coupling with a precursor pipe simulation through preCICE in order to generate fully developed turbulent inflow conditions for the main domain.

The results were analyzed to assess the capabilities and limitations of the adopted methodology through comparison with experimental data. The precursor simulation is shown to provide physically consistent turbulent inlet conditions, with mean velocity and Reynolds stress profiles in reasonable agreement with reference data and an adequate fraction of resolved turbulent kinetic energy. In the main domain, the simulations capture the main flow features around the rod tip, including flow separation, pressure recovery, and the general behavior of the velocity and Reynolds stress fields, while the comparison with PIV measurements indicates promising agreement, especially for the streamwise velocity and downstream Reynolds stresses. At the same time, the report emphasizes that the VKI results remain preliminary due to limited averaging time and identifies the rigid-body treatment of the rod and the omission of outlet pipes as the main modelling limitations. It concludes by proposing future work aimed at improving structural fidelity and extending the coupling strategy toward a more realistic flexible-body fluid-structure interaction model.

Since the outlet pipes are excluded from the present model, their influence on the flow field near the rod tip warrants further investigation. A computationally efficient approach would be to perform a fixed-rod simulation and compare the flow field near the free end with and without the outlet pipes. If the flow field in this region remains unaffected, it can be concluded that the outlet pipes have a negligible influence on the rod motion.

The primary limitation of the present model is the treatment of the rod as a rigid body. To improve the fidelity of the simulations, the following approaches of increasing complexity are proposed. As an intermediate step, the pressure fluctuations on the fixed rod could be extracted and mapped onto a finite element model to solve the structural dynamic problem in a coupled one-way manner. This would capture the flexible response of the rod without the computational overhead of a fully coupled FSI simulation. A further improvement would be to replace the rigid body model with a numerical solver of the partial differential equation governing the transverse vibration of a slender beam, derived from Euler-Bernoulli beam theory, and couple it with preCICE to achieve a two-way fluid-structure coupling. This approach is expected to be more computationally efficient than a full finite element solver, while providing a more faithful representation of the rod dynamics.

Funded by
the European Union

6. Overall Conclusions

Deliverable D6.3 successfully concludes the comprehensive numerical benchmarking campaign for the single-phase cantilever rod, definitively marking the achievement of Task 6.2 within the GO-VIKING project. This report not only evaluated the simulation capabilities of the CFD/FSI methodologies, but also stands as a testament to the effective collaborative efforts of the contributing partners: PSU, EDF, VKI, NRG PALLAS, EDF-Energy, and IPP.

The core objective—comparing the solutions obtained with different computational methods against the experimental data from D2.1—was achieved with the following takeaways from all the simulations performed by the participants including the benchmark case:

- Experimental Data: A large quantity of first and second order flow field statistics as well as vibration data are available for validation. While the experimental data provided valuable insight, they cannot be used directly for quantitative validation due to slight deviations in the installation of the long and slender rod – the rod appears to be misaligned relative to the confining pipe axis. NRG PALLAS investigated the effect of the rod offset, assuming the maximum offset of 0.3 mm reported by the experimentalists. At this offset, the effect on the flow field and vibrational characteristic of the rod was found to be negligible (Hussain, et al., 2025). This would suggest the actual misalignment to likely be larger than reported by the experimentalists. If this is indeed the case, how large might its impact on the numerical results be is unclear. Therefore, further investigations are necessary.

- High Resolution Data:

    - Rich DNS data is made available by PSU through CFD investigations of flow around the rod with hemispherical end and blunt end. The Q-criterion and TKE budget was carefully examined. The evolution of statistics is remarkably different near the rod tip and for a considerable distance along the rod wall,

Funded by the European Union

for each case, before returning to expected annular flow statistic behaviors. These statistics provide high fidelity DNS data for benchmarking and validating future, lower costing, turbulence modeling tools.

- EDF performed simulations using WR-LES on the case with the rod having a hemispherical tip, investigating the effect of the rod vibrations by simulating the fixed rod scenario and the FSI scenario. The costs were made manageable by utilizing the beam model for the rod. FSI and fixed rod simulations yielded very close velocity and Reynolds stress profiles, which means that the rod vibration does not have a strong impact on the flow. Results also showed good predictions of vibration frequencies but underpredictions in the vibration amplitude compared to the experiment.

- VKI performed a coupled LES simulation where the incoming flow was simulated as an auxiliary fully-developed channel flow and directly linked in to the domain describing the cantilever rod in a pipe. The cantilever rod was treated as a rigid body with a junction. Unfortunately, the simulated time is short, only allowing a qualitative comparison with the other partners and the experiments. The simulations will be continued in the near future to evaluate if the approach is a viable way to simulate FIV without modelling the bending of the solid.

- Medium Resolution Data:

  - EDF-Energy performed FSI simulations of the blunt end and rounded end configurations using the SSG RSM model and a wall modelled mesh. The key vibrations results showed that the approach worked well in predicting vibrations for the blunt end configuration, however with differences in the prediction of the amplitude (underpredicting for Re=16k by a factor of ~2, overpredicting for Re=46k by a factor of ~3). On the other hand, it completely failed to predict any significant vibration for the rounded end configuration at Re=21.2k.

  - NRG PALLAS performed similar FSI simulations on both configurations using the K-Epsilon (Cubic) model and a wall resolved mesh. The findings of the work showed good predictions of the flow field and vibration frequencies. For the vibration amplitude, a very good match was observed for the blunt end at Re=23.33k with a slight underprediction by a factor of ~1.05 while it was more severe for the curved end at Re=21.2k, 40k by an order of magnitude.

  - IPP also performed FSI simulations solely for the rounded end configuration at Re=21.2k using the K-Omega SST model and a wall resolved mesh, and modelled the rod with a beam model. The flow field data showed good agreement with experimental data. However, the obtained dynamics of the rod tip displacements in both the front and side directions were peculiar. The vibration amplitude was found to be of the same order as the prediction of EDF that used LES, which is quite promising. On the other hand, the frequency of vibration was found to be very dissimilar in the two directions of measurement – more than a factor of 2 between them.

Finally, within the benchmark study, a stronger focus was made on the modelling choices, simulation strategies and computational costs along with the comparison of obtained flow field and vibration results. A few key takeaways of the benchmark are mentioned below.

- The choice of turbulence model has the largest impact on the accuracy of the solution. The impact of this choice overshadowed any potential gain in accuracy of using CSM over beam model, and respecting the 2 outlet configuration of the test section over a simpler single outlet configuration.
    - As expected, the high resolution approaches offer the highest accuracy in results in the ranked order of DNS followed by LES.
    - However, URANS demonstrated to be able to make good predictions for first order flow field statistics and decent FSI predictions. The latter appears to be connected to having a wall resolved mesh as results showed a combination of eddy viscosity models with a wall resolved mesh to predict significant vibrations, as opposed to the better SSG RSM turbulence model in combination with a wall modelled mesh.
- The higher accuracy comes with a higher computational cost. This is precisely the reason why URANS-based models remain the working horse of the industry today. The gap in accuracy in the URANS solution can be envisioned to be closed with better scale resolving approaches as was established in the current study. Hybrid models, which use RANS near the wall, may not be suitable for TIV, but could be investigated before being considered as an alternative of LES. Another approach could be using synthetic turbulence such as the Anisotropic Fluctuation Model, which was investigated in WP5 of the GO-VIKING project.

7. Bibliography

Chourdakis, G., 2022. preCICE v2: A sustainable and user-friendly coupling library. *Open Research Europe*, 2(51).

Chourdakis, G., Schneider, D. & Uekermann, B., 2023. OpenFOAM-preCICEL coupling OpenFOAM with external solver for multi-physics simulations. *OpenFOAM journal*, Volume 3.

Cioncolini, A. et al., 2018. Axial-flow-induced vibration experiments on cantilevered rods for nuclear reactor applications. *Nuclear Engineering and Design*, Volume 238, pp. 102-118.

Cioncolini, A. et al., 2022. *Deliverable 2.1 of the GO-VIKIING project (101060826) Single-phase cantilever rod experiement and benchmark setup*, Manchester, UK: s.n.

Geuzaine, C. & Remacle, J.-F., 2009. Gmsh: a three-dimensional finite element mesh generator with built-in pre- and post-processing facilities.. *International Journal for Numerical Methods in Engineering*, 79(11), pp. 1309-1331.

Hussain, M. M. M. D. et al., 2025. *Deliverable 2.2 of the GO-VIKING project (101060826) Simulation of the single-phase Cantilever Rod benchmark,* Petten, The Netherlands: s.n.

Lavoie, P. et al., 2007. Spatial resolution of PIV for the measurement of turbulence. *Experiments in Fluids,* Volume 43, pp. 39-51.

Li, H. et al., 2024. ip shape effects on the axial-flow-induced vibration of a cantilever rod. *Journal of Fluids and Structures,* Volume 127, p. 104132.

Sarno, L. et al., 2019. Challenges and improvements in applying a particle image velocimetry (PIV) approach to granular flows. *Journal of Physics: Conference Series,* Volume 1249, p. 012011.

Yoshizawa, A., 1986. Statistical theory for compressible turbulent shear flows, with the application to subgrid modeling. *The Physics of Fluids,* 29(7), pp. 2152-2164.

Zagarola, M. V., 1996. *Mean flow scalingof turbulent pipe flow,* s.l.: Princeton University.

Funded by
the European Union